LONG PERIOD AMPLIFICATION OF SEISMIC WAVES IN ISTANBUL METROPOLITAN AREA

by

Esra KALKAN ERTAN

B.S. Geophysical Engineering, İstanbul University, 2007

M.S. Geophysics, Boğaziçi University, 2013

Submitted to the Kandilli Observatory and Earthquake Research Institute in partial fulfillment of the requirements for the degree of Doctor of Philosophy

Graduate Program in Geophysics

Boğaziçi University

2025

LONG PERIOD AMPLIFICATION OF SEISMIC WAVES IN ISTANBUL METROPOLITAN AREA

APPROVED BY :

Assoc. Prof. Ali Özgün KONCA ……………..

(Thesis Supervisor)

Prof. Hayrullah KARABULUT ………………

Prof. Semih ERGİNTAV ……………….

Boğaziçi University, Dep. of Geodesy

Prof. Argun KOCAOĞLU ……………….

Istanbul Technical University

Assoc. Prof. Onur TAN ………………..

İstanbul University-Cerrahpasa

DATE OF APPROVAL: 14.02.2025

ACKNOWLEDGEMENT

Kandilli was never just an institution for me, it was my home. It was the place where I found not only knowledge but also friendship, laughter, and some of the most precious memories of my life. The walls of Kandilli witnessed my struggles, my breakthroughs, my moments of doubt, and my moments of joy. No matter where life takes me, I will always carry those memories in my heart. Kandilli is not just a place, it is a part of who I am, and I will never forget that.

This has been such a long, winding, and often lonely road. Along the way, I gained so many people, and I lost just as many. But some… some were always there. Unwavering. Standing beside me, even when I felt like falling apart.

First and foremost, Professor Dr. Nurcan Meral Özel…How can I ever express my gratitude enough? Even from a distance, she never let go of me. She was always there, her presence a quiet yet powerful force, lifting me when I stumbled. I will forever be grateful to her.

And Professor Dr. Semih Ergintav… He left an imprint on my life that no words can truly capture. He shaped my path, laid the foundation for my future, and believed in me when I couldn't even believe in myself. Who I am today, what I have accomplished—so much of it is thanks to him.

Assoc. Prof. Dr. Ali Özgün Konca…Where do I even begin? If there is one person who has been the definition of perseverance, patience, and unwavering support in my life, it is him. He is not just a mentor, but a guide, a problem-solver, a friend who always knows when to push and when to pull back. He is like a Swiss Army knife, sharp, versatile, always prepared for anything. There were moments when I was ready to give up, but he held on for me. And when he felt like giving up, I was the one holding on. We carried each other through the darkest, most difficult days of this journey, and now, standing here at the end, I know I could not have made it without him. His wisdom, his encouragement, and his ability to find a solution to every challenge have been nothing short of extraordinary. If I have reached this moment, if I have endured and succeeded, it is because he never stopped believing in me. There are no words that can truly capture how much I owe him.

Professor Dr. Hayrullah Karabulut, quiet, yet full of warmth. A heart so kind, a presence so steady. His perspective on life, his humor, and his wisdom will always stay with me.

To Professor Dr. Onur Tan and Professor Dr. Argun Kocaoglu, I owe my deepest gratitude. Their invaluable feedback, insightful words have shaped the way I see the thesis. I am grateful for the doors they have opened in my mind, ones I never knew existed.

Dr. Başak Bayraktar… Words fail me when I try to describe what she means to me. She was there. Always. Through every storm, every moment of doubt, every tear. Even when miles stretched between us, our hearts were never far apart. I love her more than words can say.

Dr. Zeynep Coşkun and Fatih Turhan…My angels, my safe space, my unshakable support. They understood me when no one else did, they stood by me when I didn't even know how to stand on my own. They are irreplaceable, and I hope they will always be a part of my life. Love you millions.

Dr. Yasin Sait Toksoy, we walked similar roads, stumbled through the same storms, and in the end, we made it. My dear friend, may his kindness, his laughter, and his light never dim.

One of the greatest blessings of my time at Istanbul Metropolitan Municipality was meeting Dr. Evrim Yavuz, Dr. Özlem Yıldız Yüksekol, Nilüfer Yılmaz, and Esra Fitoz, the ones who filled my days with laughter, who reminded me that no matter how dark it seemed, there were always better days ahead.

Kübra Kiransan, she entered my life exactly when I needed her. At the right time, in the right place. And I know this is only the beginning of all we will accomplish together.

I sincerely thank Dr. Figen Eskiköy, who made even the hardest times better with her almond and sour cherry cake. I will never forget this taste.

And then, my family, my heart, my soul, my reason for everything.

To my mother, Sırriye Kalkan, the woman who taught me what resilience means. The woman who held me when I cried, who prayed for me in my weakest moments, and who never, not even for a second, doubted that I would make it here. Her love, her strength, and her unwavering belief in me have been the foundation of everything I have achieved.

To my father, Kenan Kalkan, my silent protector, my unwavering support. No matter how tough things got, I always knew that he was there, watching over me, believing in me, and carrying my burdens in his own quiet way. His sacrifices, his wisdom, and his endless patience are the reason I stand here today.

To my sister, Kısmet Kübra Kalkan Balcı, my first best friend, my confidant, my forever ally. She has been my mirror, my anchor, and my greatest cheerleader. Through every challenge, she reminded me of who I am and what I am capable of. Life is brighter, softer, and infinitely better because she is in it.

My beloved husband, Deniz Ertan, the man who held my hand through every storm, even when I was too tired to hold his. He carried my worries, my exhaustion, my fears, and he never once let go. There were moments when I felt like I had nothing left to give, but he gave me strength, reminded me of why I started, and stood by me even when I was too lost in my work to see how much he was holding everything together. There are no words that can do justice to what he has done for me. This thesis, this success, this moment, it belongs to him just as much as it belongs to me.

And finally, my precious daughter, Ayşe Benan Ertan, the light of my life, my purest love, my reason for never giving up. Every sacrifice, every sleepless night, every tear was for her. She is the reason I kept going when I had no energy left, the reason I fought through every hardship, the reason I never lost hope. Her laughter, her tiny hands reaching for me, her innocent love—they gave me the strength to finish this journey. My greatest dream is that she will grow up knowing that no challenge is too great, no mountain too high, and that she is capable of anything. This is for her.

Love you to the moon and back… and then some.

The end is not near. The end is here.

ABSTRACT

LONG PERIOD AMPLIFICATION OF SEISMIC WAVES in ISTANBUL METROPOLITAN AREA

Istanbul is a megacity located very close to the North Anatolian Fault and thus is highly vulnerable to seismic hazards. During the 2019 Mw5.7 Silivri earthquake the recorded displacements show site amplification at long-periods and prolonged duration corresponding to the frequency range of 0.1-1.0 Hz. The excitations in these frequency range cannot be explained with variations in very shallow structure only and requires an analysis that considers deeper sedimentary basins. Amplifications in this frequency range cause resonance effects and serious damage tall and high-rise buildings and infrastructure. The Mw 5.9 Silivri earthquake of September 26, 2019, provided a good dataset for investigating site-specific amplification effects. This thesis analyzes acceleration records from nine AFAD strong-motion stations distributed over different geological units to evaluate the characteristics of long-period amplification.

As an initial test, we compare synthetic waveforms using two velocity: (i) a crustal model from Karabulut et al. (2020), and (ii) an AFAD-based station specific shallow velocity model which includes near-surface velocity layers from AFAD station reports. We show that neither of the models work well for amplified waveforms especially on the motion recorded in stations on the European part of Istanbul.

Instead we generate synthetic seismograms for each station. We try two approaches. First, we generate synthetic waveforms at the surface of the crustal model which is assumed to represent a hard-rock reference waveform. Then we randomly generate 2 layer structures on top of this structure and optimize the fit to the data in the frequency domain. As a second approach we calculate the synthetic waveforms at a depth of 2 km. We then again optimize for each station the layered structure that represent first two km beneath the station. For each trial we calculate the amplified waveforms using the transfer function of these two layers for SH waves. For each station we generate 5000 velocity models and optimize the fit between the acceleration spectrum of data and

synthetics. The best-fitting velocity structure was obtained by spectral fitting of synthetic and recorded waveforms.

Results show that the site amplification largely varies with local geological conditions: stations located on stiff geological units (e.g., 3405, 3413, 3417) have minimal amplification, while soft sediment sites (e.g., 3411, 3412, 3416) undergo strong amplification and long shaking. Station 3412 displays anomalous amplification and longer oscillations probably due to very thick unconsolidated sediments or local site complexities. While the AFAD-based velocity model underestimated the observed amplification, the crustal model fits better for hard rock sites but failed to capture the amplification at soft sediment stations.

Based on our modeling results, we estimate that stations 3407, 3411, 3413, and 3416, which are situated on soft sediment, have sediment thicknesses ranging between 120 and 200 meters with underlying layers exhibiting shear wave velocities of 248 m/s, 87 m/s, 420 m/s, 188 m/s for first layer, respectively. For the second layer values for each station 254 m/s, 294 m/s, 789 m/s, 220 m/s for station 3407, 3411, 3413, 3416 respectively and the layer thickness for second layer ranging between 200 m to 1000 m. The better fit at a depth of 2 km for these stations suggests that deeper sedimentary layers significantly influence wave amplification. In comparison, AFAD's velocity models provide shear wave velocities of 597 m/s for 3407, 323 m/s for 3411, 452 m/s for 3413, and 420 m/s for 3416 for first layer and 2000m/s for 3407, 523 m/s for 3411, 772 m/s for 3413 and 849 m/s for 3416 for the second layer, indicating some discrepancies between our estimated values and the reference models. These differences highlight the need for further refinement, considering potential lateral variations and deeper structural influences.

When compared to AFAD's reference models, our synthetic seismograms show good agreement for stations 3407, 3411, 3413, 3416 where both amplitude and spectral content are well captured. However, discrepancies at other stations suggest that additional factors, such as lateral heterogeneities or path effects, may be influencing the results. In general, for significantly amplified stations on the Anatolian side, it is to refine these models further, it is necessary to incorporate additional earthquake records from different directions to assess whether the observed variations persist across different source locations and azimuths.

ÖZET

İSTANBUL METROPOL ALANINDA SISMIK DALGALARIN UZUN PERIYOTLU AMPLIFIKASYONU

İstanbul, Kuzey Anadolu Fayı'na çok yakın bir megakent olup, bu nedenle sismik tehlikelere karşı oldukça savunmasızdır. 2019 Mw 5.7 Sivrice depremi sırasında kaydedilen yer değiştirmeler, uzun periyotlarda zemin büyütmesini ve uzun süreli sarsıntıları göstermektedir ve bu büyütmeler 0.1-1.0 Hz frekans aralığında gözlemlenmiştir. Bu frekans aralığındaki dalgalanmalar çok sığ yapılarla açıklanamaz ve daha derin sedimanter havzaları dikkate alan bir analizi gerektirir. Bu frekans aralığındaki büyütmeler, rezonans etkilerine yol açarak yüksek binalar ve altyapı için ciddi hasarlara neden olmaktadır. 26 Eylül 2019'da meydana gelen Mw 5.9 Silivri depremi, bölgeye özgü zemin büyütme etkilerini araştırmak için iyi bir veri seti sağlamıştır. Bu tez, farklı jeolojik birimlere dağıtılmış dokuz AFAD kuvvetli yer hareketi istasyonunun ivme kayıtlarını analiz ederek uzun periyot büyütme özelliklerini değerlendirmektedir.

İlk test olarak, iki farklı hız modeli kullanılarak sentetikler karşılaştırılmıştır: (i) Karabulut ve ark. (2020) tarafından önerilen bir kabuk modeli ve (ii) AFAD istasyon raporlarında belirtilen yüzeye yakın hız katmanlarını içeren AFAD tabanlı istasyona özgü sığ hız modeli. Analizler, bu modellerin özellikle Avrupa Yakası'nda bulunan istasyonlarda gözlemlenen büyütmeleri doğru bir şekilde yakalayamadığını göstermektedir.

Bu nedenle, her istasyon için yeni sismogramlar üretilmiştir. Daha sonra, istasyonun altındaki ilk iki kilometrelik bölgeyi temsil eden rastgele iki tabakalı yapılar oluşturulmuştur. Ardından, bu iki tabakanın SH dalgaları için transfer fonksiyonu kullanılarak büyütülmüş dalga formları hesaplanmıştır. Her bir istasyon için 5000 farklı hız modeli oluşturulmuş ve sentetik ile gözlemsel ivme spektrumları arasındaki uyum

optimize edilmiştir. En iyi uyum sağlayan hız yapısı, sentetik ve kayıtlı dalga formlarının spektral eşleşmesiyle elde edilmiştir.

Sonuçlar, zemin büyütmesinin yerel jeolojik koşullara bağlı olarak büyük ölçüde değiştiğini göstermektedir: sert jeolojik birimlere yerleştirilmiş istasyonlar (örneğin, 3405, 3413, 3417) minimum büyütme gösterirken, yumuşak sediman üzerine yerleştirilmiş istasyonlar (örneğin, 3411, 3412, 3416) güçlü büyütme ve uzun süreli sarsıntı sergilemektedir. 3412 istasyonu, muhtemelen çok kalın sıkışmamış sedimanlar veya yerel saha karmaşıklıkları nedeniyle anormal büyütme ve daha uzun salınımlar göstermektedir. AFAD tabanlı hız modeli, gözlemlenen büyütmeyi olduğundan düşük tahmin ederken, kabuk modeli sert kaya istasyonları için daha iyi uyum sağlamakla birlikte, yumuşak sediman istasyonlarında büyütmeyi yakalayamamıştır.

Modelleme sonuçlarımıza dayanarak, yumuşak sediman üzerinde bulunan 3407, 3411, 3413 ve 3416 istasyonlarının sediman kalınlıklarının 120 ile 200 metre arasında değiştiğini ve altındaki katmanların sırasıyla 3407, 3411, 3413 ve 3416 için ilk katmanda 248 m/s, 87 m/s, 420 m/s, 188 m/s kayma dalgası hızlarına sahip olduğunu tahmin ediyoruz. İkinci katmanda ise sırasıyla 3407, 3411, 3413 ve 3416 için 254 m/s, 294 m/s, 789 m/s, 220 m/s kayma dalgası hızları elde edilmiş olup, ikinci katman kalınlığı 200 m ile 1000 m arasında değişmektedir. Bu istasyonlar için 2 km derinlikte daha iyi bir uyum sağlanması, daha derin sedimanter katmanların dalga amplifikasyonunu önemli ölçüde etkilediğini göstermektedir. Karşılaştırıldığında, AFAD'ın hız modelleri ilk katmanda 3407 için 597 m/s, 3411 için 323 m/s, 3413 için 452 m/s ve 3416 için 420 m/s; ikinci katmanda ise 3407 için 2000 m/s, 3411 için 523 m/s, 3413 için 772 m/s ve 3416 için 849 m/s kayma dalgası hızları sağlamaktadır. Bu farklılıklar, olası yanal değişimler ve daha derin yapısal etkiler göz önünde bulundurularak daha fazla iyileştirme yapılması gerektiğini ortaya koymaktadır.

AFAD'ın referans modelleriyle karşılaştırıldığında, sentetik sismogramlarımız 3407, 3411, 3413, 3416 istasyonları için iyi bir uyum göstermektedir; hem genlik hem de spektral içerik iyi bir şekilde yakalanmıştır. Ancak diğer istasyonlardaki farklılıklar, yanal heterojenlikler veya yol etkileri gibi ek faktörlerin de sonuçları etkileyebileceğini göstermektedir. Bu modellerin daha iyi optimize edilmesi için farklı yönlerden gelen depremler analiz edilmeli ve gözlemlenen farklılıkların farklı kaynak konumları ve azimutlar boyunca devam edip etmediği araştırılmalıdır.

TABLE OF CONTENTS

TABLE OF FIGURES

LIST OF TABLES

LIST OF SYMBOLS

h	Thickness
Hz	Hertz
k	Wavenumber
Qp	Quality factors for attenuation for P wave
Qs	Quality factors for attenuation for S wave
Vp	Compressional wave velocity
Vs	Shear wave velocity
ω	Angular frequency

LIST OF ACRONYMS/ABBREVIATIONS

1D	One Dimensional
2D	Two Dimensional
AD	Anno Domini
AFAD	Ministry of Interior Disaster and Emergency
BC	Before Christ
EGF	Empirical Green’s Function
FK	Frequency and Wavenumber Method
GMPE	Ground Motion Prediction Equation
HVSR	Horizontal to Vertical Spectral Ratio
	Institute
Km	Kilometer
KOERI	Kandilli Observatory and Earthquake Research
	Management Presidency
NAF	North Anatolian Fault
SAC	Seismic Analyses Cod
SSR	Standard Spectral Ratio

1. INTRODUCTION

The North Anatolian Fault (NAF), one of the most active and highest seismic hazard fault zones in the world, is a transform fault that accommodates westward motion of Anatolian block with respect to Eurasian plate. During the 20^{th} century, large earthquakes migrated from east to west starting with 1939 Mw 7.8 Erzincan earthquake (Stein et al., 1997). Among these large earthquakes are the disastrous 1999 earthquakes, Mw 7.4 İzmit (Kocaeli) and the Mw 7.1 Düzce earthquakes, which led to heavy losses of lives, structural damage in many parts of eastern Marmara region, and multi-billion-dollar financial losses. Although the exact size and location is a matter of debate, a section of the NAF that did not rupture in the last 2 centuries is beneath the Sea of Marmara posing an imminent danger for the surrounding cities.

Istanbul is a megacity with a population over 17 million people, situated very close to the western termination of the North Anatolian Fault (NAF) and is generally regarded as one of the most seismically hazardous cities worldwide. The recent decades have been marked by extreme urbanization and heavy population growth, which hugely enhanced the probability of damage. Poorly regulated infrastructure development in many areas of the region contributes to the most terrible scenarios related to future seismic activity along the NAF.

Various geological and geotechnical studies for seismic hazard assessment have been conducted in the Marmara Region; most of these were based on site response approaches without including waveform simulations. Most of the research in the region since 1999 has been on engineering applications within regional-scale studies, such as those by Atakan et al. (2002), Erdik et al. (2003a), and Erdik et al. (2004). In particular several studies focused on simulations of strong ground motion for Sea of Marmara, by Pulido et al. (2004) and Birgören et al. (2004) paying especial attention to the fault rupture scenarios. Furthermore, Picozzi et al. (2009) also developed a micro zonation characterization of the western part of Istanbul by carrying out theoretical site responses using S-wave velocity profiles from micro-array data, and then applying the propagator matrix method for a 1D-layered medium.

Although several studies have investigated ground motions in the region, most of them fail to address the specific characteristics of long-period ground motion that are relevant for a densely populated and highly urbanized city like Istanbul. The investigation of long-period ground motion plays an important role in seismic hazard assessment, especially for highly populated areas such as Istanbul. Indeed, long-period ground motion acts mainly on tall and high-rise buildings and large infrastructures and tall building, which are commonly present in megacities. On the other hand, the study of wave propagation across the Marmara Sea-and more precisely, its interaction with Istanbul-represents the primary importance in the framework of hazard mitigation. Understanding these dynamics is of extreme importance for the better preparedness and mitigation of impacts of any future earthquakes that may strike this highly exposed region. Despite this, long-period ground motion has received scant attention in specific studies pertaining to Istanbul.

This calls for further research on long-period ground motion with continuous acceleration in urbanization, an increase in the number of high-rise structures, and critical infrastructure within the metropolitan area. Such studies are indispensable to gain better knowledge and understanding of the wave propagation characteristics across the Marmara Sea and in developing seismic resilience and risk mitigation in one of the most seismically vulnerable metropolitan areas in the world.

Long-period ground motion refers to seismic waves with oscillation periods longer than two seconds, hence posing a serious risk in the urban areas of Istanbul, as in all metropolitan cities with advanced infrastructure. It has been realized, in fact that such waves, on the one hand, become hazardous for a high-rise building, long-span bridges, or other critical utility systems as these may provoke resonances if a natural frequency of a structure coincides with dominant frequency of seismic waves (Kanamori, 1994; Boore, 2003), which in turn amplifies the structural vibrations to cause severe damage or collapse. For example, in the 2011 Great East Japan Earthquake, shaking in the high-rise buildings of Tokyo was very long and it created critical non-structural damage such as broken ceiling panels (Kajima Corporation, 2012).

In general, GMPE (Ground Motion Prediction Equation) models use VS30, representing the average shear-wave velocity of the top 30 meters, as one of the key parameters in site effect estimations (Joyner & Boore, 1981). However, VS30 describes site response mainly for high-frequency motions, while the amplification of long-period ground motion is controlled also by deeper geological structures to a great extent (Bard, 1999; Zhu et al., 2020). Several studies have demonstrated that deep sedimentary basins and thick soft soil layers play a crucial role in amplifying long-period ground motions (Semblat et al., 2005; Day et al., 2008). For example, resonance effects in Mexico City's basin caused extreme amplification during the 1985 Michoacán earthquake with consequent very extensive structural failures (Singh et al., 1988; Bard et al., 1997).

A number of different methods have been developed that quantify site amplification. Of the many methods available, one such method is the horizontal-vertical spectral ratio method, popularly called HVSR, which estimates the site resonance frequencies from the study of the horizontal-to-vertical ground motion spectra ratio (Nakamura, 1989). This methodology has a wide range of applications for micro zonation studies and constitutes one of the most valuable techniques of identification of the basic site resonance frequency due to soft sediment layers (Bard, 1999; Parolai et al., 2002). These include the Standard Spectral Ratio (SSR) approach, which considers spectral amplitude ratios recorded at a site of interest relative to those recorded at a nearby reference rock site (Borcherdt, 1970). The present approach separates the site effects from other factors contributing to ground motion and measures the amplification effects directly. Numerical simulations, including 1D and 2D site response analysis (Joyner & Chen, 1975; Boore, 2004) and full waveform modeling using the finite-difference or spectral element methods, have also been done in investigating the amplification of long-period ground motion (Komatitsch & Tromp, 1999; Bielak et al., 2010).

Tan et. al, (2022), analyzes the seismic activity in the Istanbul metropolitan area and the potential impact of moderate earthquakes (Mw 5), emphasizing resonance effects. Numerical ground motion simulations based on the 2021 Kartal-Istanbul earthquake reveal that spectral accelerations for Mw 5 events may exceed the design spectrum between 0.2–0.6 s and approach it between 0.4–1 s, leading to resonance phenomena.

Özel et. al, (2004) examines the strong ground motion and site effects during the largest aftershock (Mw 5.8) of the 1999 Izmit earthquake, showing that while peak ground acceleration near the epicenter matched empirical predictions, significant amplification of S-waves (~1 Hz) due to thick low-velocity sediments in the Avcılar district contributed to localized damage, highlighting the role of site effects.

Local site effects in the Ataköy area (SW Istanbul) using synthetic and empirical data, revealing strong spectral amplifications (~1 Hz) with SA factors of 1.5–2 in alluvial sites, which have implications for similarly structured areas in southwestern Istanbul (Soronsen et. al, 2006).

The site effects in Avcılar, the most damaged suburb during the 1999 Izmit earthquake, using seismic and microtremor measurements, revealing that seismic energy trapping in a 100–150 m thick low-velocity layer caused amplification (0.3–1.6 Hz), while microtremor methods underestimated amplification below 1 Hz (Ergin et. al, 2004).

More recently, EGF (empirical Green's function) methods have also been applied to estimate site amplification by comparing smaller recorded earthquakes with larger target events (Irikura, 1986; Satoh et al., 1995). This helped in constraining the amplification factors in complex geological settings. Further, 3D numerical modeling of seismic wave propagation has also been a prime basis in providing understanding of long-period ground-motion behavior of the biggest urban cities lying within the sedimentary basin area of both Los Angeles and Istanbul (Graves et al., 2011; Pulido et al., 2004). All such models simulate the appropriate amplification effects in terms of comprehensive subsurface velocity structure.

The amplification in broad frequency band indicates that an approach that considers deeper structures, in the order of kilometers, is necessary. In that regard, for the region of Istanbul, deep sedimentary layers are known to strongly amplify seismic waves with long periods; hence, in order to provide a good modeling of amplification for seismic hazard mitigation, both empirical and numerical methods are necessary, as discussed in Picozzi et al. (2009) and Karabulut et al. (2020).

Local geological conditions, like deep sedimentary basins in addition to soft soils, also increase the amplitude and period of seismic waves, thus enhancing the long-period ground motion (Bard, 1999; Joyner & Boore, 1981). Indeed, this happened in Mexico City during the 1985 earthquake, where the loose soils the city was resting on amplified the ground motion significantly and caused immense destruction (Singh et al., 1988). As geological structure in Marmara Region of Istanbul is the same, that city is also subject to long-period ground motion.

The thesis addresses the key knowledge gap, pertaining to site-specific amplification effects manifested during the Mw 5.9 September 26, 2019 Silivri earthquake in the frequency range that cannot be explained by the shear wave velocity structure of the top 30 meters. My goal is to study the long-period ground motion in the Istanbul metropolitan area by using acceleration records obtained from nine AFAD strong-motion stations: 3405, 3406, 3407, 3408, 3411, 3412, 3413, 3416, and 3417. The distribution of these recording stations across the city on various geological units renders the dataset particularly suitable for the investigation of site-specific amplification effects.

The strong-motion recordings at these stations indicate that the amplification varies significantly with respect to the local site conditions. Stations 3405, 3413, and 3417 are located on relatively stiff and ductile geological units. Thus, their ground-motion amplifications are essentially minimal, as predicted by their stiffer subsurface conditions. On the contrary, the stations on soft soils, which tend to be on the European side of the city, such as stations 3411, 3412, and 3416, show pronounced ground-motion amplification and also longer shaking duration in comparison to other stations. This indeed reveals that path effects can significantly influence ground-motion behavior, especially for those urban cities where the subsurface compositions vary substantially.

In this study we focus on 0.05 to 1 Hz frequency band and find the velocity structure of the top few kilometers to explain the amplified and long duration S waves recorded in Istanbul during the 2019, September 24, Mw5.7 Silivri Earthquake. The frequency range is selected due to the fact that the long-period ground motions give the maximum response within the natural frequencies of tall buildings and other critical infrastructures and also the amplification is more expressed in this range. In order to focus on S wave amplification and obtain S wave models we utilize transverse component of the seismic records to avoid converted phases.

These long-period ground motions may lead to resonance of some basins and also structures and pose a serious hazard, especially in cities like Istanbul with an ever-increasing number of high-rise buildings. High-frequency components, which are less relevant for large structures, were excluded to avoid interference and keep the analysis focused on the most critical frequency bands.

The procedure for obtaining station-specific 1D velocity structures is carried out using strong-motion data recorded at AFAD stations during the 2019 Mw 5.7 Silivri earthquake. Initially, synthetic displacement waveforms are generated at the AFAD station locations by applying a frequency-wavenumber algorithm (Zhu and Rivera, 2002) in combination with the crustal model proposed by Karabulut et al. (2020). While some stations are successfully modeled with the 1D crustal velocity model, significant amplification of the observed data, compared to the estimated ground motion, is identified at certain stations. To assess whether these estimations can be improved, the velocity structures reported by AFAD are incorporated into the analysis. It is demonstrated that deeper and alternative velocity models are required to explain the observed amplification at some sites. Subsequently, synthetic tangential component acceleration waveforms are generated at a depth of 2 km. Two soft layers are randomly introduced, while the remaining portion of the 2 km depth is filled using the crustal model from Karabulut (2020). Through spectral fitting of the recorded seismograms, the best-fitting two-layer structure is determined to represent the upper ~1 to 2 km of the site.

Synthetic seismograms computed from the velocity profiles formed a strong basis for the understanding of the contrasts between hard rock and soft soil sites. The hard rock stations, like 3405, 3406, 3413, and 3417, have limited amplification because of the restrictive subsurface conditions. On the contrary, stations with soft soil like 3411, 3412, and 3416 have shown longer shaking duration and higher amplification factors in good agreement with their softer geological settings. These results strengthen the critical influence of local geology on seismic hazard.

Besides, this study points out that the need for site-specific amplification studies shall be brought within the context of urban development and seismic hazard assessment. Evidence from the 2019 Silivri earthquake indicated that effective targeting of updated legislative measures and building codes is necessary regarding local geology and long-period ground motion. All these factors would play a very important role in reducing seismic vulnerability and improving resilience in the rapidly growing urban landscape of Istanbul.

Chapter 2 gives a general overview of geology of Istanbul and tectonic activity around the Marmara Region. Furthermore, it deals in great detail with the local geological setting, indicating that structural complexity constitutes part of a setting developed within a close proximity to the North Anatolian Fault or NAF-the major strike-slip system that has repeatedly generated disastrous earthquakes over history. This chapter describes how local geological features interact with the tectonic forces and thereby sets the scene for understanding seismic risks in Istanbul.

Chapter 3 contains the data and methodology of this study. This section describes seismic data collection and processing, records from nine AFAD-controlled strong-motion stations. It further gives a detailed analysis of the different methods used during analysis, PySeismoSoil application on the calculation of amplification factor, filtering of seismic records aimed at long-period ground motion and utilization of synthetic seismogram for comparative study.

Chapter 4 presents the results of the analysis, giving insight into the amplification effects observed during the Mw 5.9 September 26, 2019 Silivri earthquake. The findings are discussed in a systematic manner, underlining the striking contrasts in ground motion behavior between hard rock and soft soil sites.

Chapter 5 includes the findings into the wide context of seismic hazard assessment and urban resilience. This chapter sets out to discuss what the implications of such findings would be for Istanbul's burgeoning urban landscape and strongly indicates that any seismic risk mitigation strategy should include long-period ground motion analysis. This points out in the discussion that not only does it feed into real-life application, but it also serves to reinforce seismic resilience in Istanbul and other vulnerable regions. It emphasizes that these findings will be the basis for more resistant infrastructure design, urban planning development, and legislative efforts on reducing the effects of future earthquakes.

2. GEOLOGY AND SEISMICITY OF MARMARA REGION AND ISTANBUL METROPOLITAN AREA

Geologically, the Marmara Region is divided into three main tectonic zones: the Strandja Massif, the Istanbul Zone, and the Sakarya Zone, as identified by Ketin (1973) and Okay (1986). The Strandja Massif is made up of a variety of rocks, including sandstone, quartzite, limestone, shale, and Late Permian granitoids, all of which underwent deformation and metamorphism during the Late Jurassic period. This metamorphic series comprises rocks such as metagranite, micaschist, marble, calcschist, and quartzite (Ketin, 1973). The southern part of the Strandja Massif is covered by the Cenozoic sedimentary cover of the Thrace Basin. The Intra-Pontide Suture, running east-west beneath the Sea of Marmara, separates the Strandja-Rhodope Massif to the north from the Sakarya Zone to the south. It connects ophiolitic mélange outcrops in the Geyve-Armutlu area in the east with those around the Gulf of Saros and Şarköy in the west (Şengör and Yılmaz, 1981).

In contrast, the Istanbul Zone consists of a thick succession of unmetamorphosed sedimentary sequence ranging in age from Ordovician to Carboniferous. Due to its stratigraphy and lack of metamorphism, it is geologically distinct from its neighbor tectonic units (Ketin, 1973). The Sakarya Zone, on its part, does not have a basement of Paleozoic age hence distinguishing it from the Istanbul Zone (Hoşgören, 1995).

The Sakarya Zone is limited by the Izmir-Ankara Suture, which marks its boundary with the Anatolide-Tauride tectonic units. It has a Triassic basement represented by the Karakaya Complex, which underwent various degrees of metamorphism and deformation. This basement is unconformably overlain by Liassic conglomerates and sandstones, followed by a stratigraphic sequence of Middle Jurassic-Lower Cretaceous limestone and Upper Cretaceous flysch deposits (Ketin, 1973; Hoşgören, 1995).

The Istanbul metropolitan area is located in a region including lithostratigraphic units that represent an important part of a broad geologic time span from the Early Paleozoic, Ordovician to the Quaternary. This region also bears the deep marks of the important tectonic events which took place during this period (Özgül,2012).

In this respect, two major groups of lithostratigraphic units exist within the boundaries of Istanbul Province: one metamorphic and the other non-metamorphic. The metamorphic sequence is associated with an important tectonic event whose nature has not yet been clarified and is called the " Strandja Unit," while the non-metamorphic sequence is referred to as the "Istanbul Unit" (Özgül,2012).

A small portion of the Strandja Unit metamorphics, which include extensive areas between Tekirdağ and Edirne in the northern part of the Thrace Peninsula, also covering schists, quartzites, and magmatites, extends to the western and northern parts of Çatalca district within the provincial boundaries of Istanbul. In the Çatalca area, units of the aforementioned metamorphic sequence are exposed, known as the "Tekedere Group," "Kızılağaç Metagranite," "Sermat Quartzite," and "Mahya Schist." (Özgül,2012).

The Istanbul Unit comprises non-metamorphic rock units of Paleozoic and Mesozoic age, covering extensive areas on both sides of the Bosphorus and the Kocaeli Peninsula. The oldest rock units of the Istanbul Unit exposed in the metropolitan area and its vicinity are terrestrial sediments of Early Ordovician age, including the Kocatöngel Formation and the Kurtköy Formation, representing fluvial and lagoonal environments. In the Early Ordovician, the landmass area started to be covered by a tectonically stable sea, represented by a transgression of the quartzites of the Aydos Formation, aged Ordovician. It was followed by a deepening during the Silurian and Devonian. During this process, the Yayalar Formation (Early Ordovician), represented by siltstone-sandstone, was successively deposited, followed by the Pelitli Formation (Early Ordovician-Silurian), reflecting shelf-type carbonate deposition; then, the Kartal Formation (Early-Middle Devonian) followed, representing a low-energy open shelf environment with abundant macrofossils and occasional limestone intercalations; and finally, the Denizli Köyü Formation (Upper Devonian-Lower Carboniferous), representing an open shelf-slope environment with abundant nodular limestones. Siliceous deposits of Early Carboniferous age, like chert, which exists as middle levels in the Denizli Köyü Formation, suggest intense silica input caused by volcanic activity close to the marine basin. In the Early Carboniferous, the dominantly unstable conditions represented by turbiditic flows were incarnated by flysch-type sandstone-shale sequences of the Trakya Formation. The magmatic intrusions, represented by the Sancaktepe Granite (Permian), developed as a result of tectonic movements active during the Carboniferous-Permian interval, and the region emerged again as land, leading to deposition of terrestrial sequences of Permian (?) - Early Triassic age. In the Middle-Late Triassic, a new transgressive sea flooded the area, represented by the Demirciler Formation (tidal), the Ballıkaya Formation (shelf carbonates), and the Tepeköy and Bakırlıkıran formations (slope deposits). No representative Jurassic-Early Cretaceous age rock units exist in this region. Volcanic-sedimentary sequences with andesitic volcanics and flysch-type clastics include the Late Cretaceous: the Sarıyer and Yemisliçay formations. The "Çavuşbaşı Granodiorite" of Upper Cretaceous age is a deep-seated rock considered to be associated with island arc volcanism active during the closure of the Tethys Ocean (Özgül,2012).

During the Eocene, intense compressive movements affecting most parts of Anatolia caused serious folding and faulting in the Marmara Basin, including the Istanbul area. These movements could have led to the evolution of the Sarıyer-Şile Fault, which runs from north to south in an approximately east-west direction, cutting the region. This has caused the thrusting of Paleozoic and Mesozoic rock units onto the Upper Cretaceous-Early Eocene sequences. The olistostromes of the Ağlayankaya Member observed in the shales of the Lower-Middle Eocene Şile Formation in the Şile region are understood to have developed as a result of these movements, which caused unstable conditions. During the course of another transgression in the Middle Eocene, from Middle Eocene to Early Oligocene, the area of Çatalca and Şile was covered by a sea with beaches and reefs along its shores, where the following were deposited: Hatipler Formation, Koyunbaba Formation, Yunuslubayır Formation, Soğucak

Limestone, and clayey muds (Ceylan Formation) in inner parts. During the Middle-Late Oligocene, tectonic movements affecting the entire Thrace Basin resulted in the rise of the region and the beginning of the land-forming processes, which continue to the present, with the development of fluvial deposits (Kıraç Formation, Çukurçesme Formation) and lagoon-lake sediments (Danismen Formation and Çekmece Formation) representing the Late Oligocene-Late Miocene interval. These movements, causing compression roughly north-south, led to the development of NW-SE and NE-SW trending shear faults and joint systems. It was these shear faults that formed as zones of weakness, controlling the morphological development of the Bosphorus and Dardanelles straits, major river valleys in the region, and the Golden Horn, which results in their zigzag geometry aligned with NW-SE and NE-SW trends. However, there is no field evidence that these shear faults are active at present, but rather they are covered by terrestrial deposits of at least Upper Miocene-Pliocene age (Figure 2.1)(Özgül,2012).

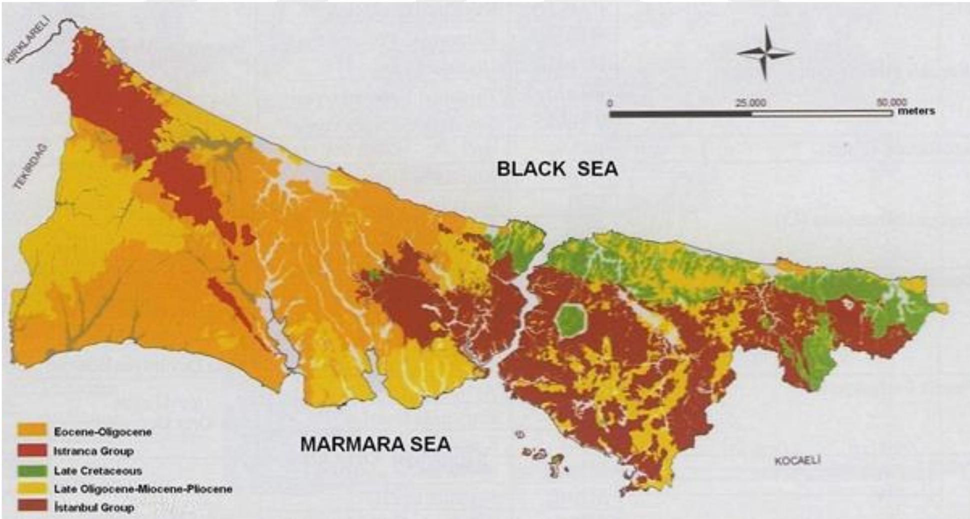

Figure 2.1. Map showing gross-scale geological outline of the İstanbul city area (from Özgül, 2011).

Figure 2.2, prepared according to the Modified Mercalli Intensity Scale, between 2100 BC—1900 AD, shows the historical earthquakes intensity distribution in the Marmara Region and points out the seismic hazards of the area (Soysal et. al. 1981). High-intensity events, such as IX and X, situated along the North Anatolian Fault, especially around the Marmara Sea, show areas that have suffered severe damage in the past. The lower intensities, such as VI and VII, are less concentrated and show that seismic activity can have effects quite far from the fault zone.

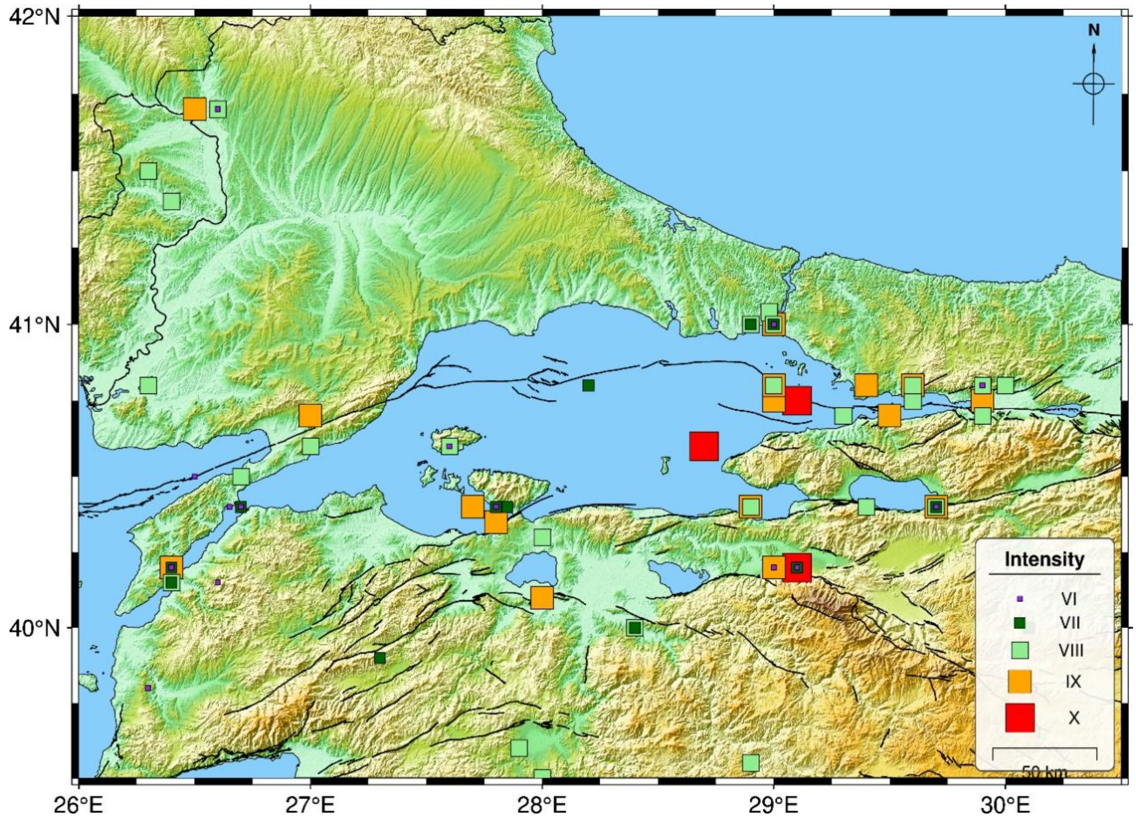

Figure 2.2. Historical earthquakes of Marmara Region and Istanbul Metropolitan Area (Soysal et. al. 1981).

Figure 2.3. presents seismicity for the Marmara Region in northwestern Turkey and demonstrates a rather thick clustering of earthquakes over the area. The red circles display epicenters of earthquakes, with the size of circles scaled for magnitude (larger circle corresponds to larger magnitude) and most of these large circles located along the NAF (e.g., M6, M7). This fault system, crossing the southern Marmara Sea, constitutes a seismic source with a number of high-magnitude events aligned close to its trend. Seismicity is diffuse from the eastern to the western limits of this map-from Istanbul and the Marmara Sea through the surrounding areas. The highest number of seismic events is concentrated in the Marmara Sea and its northern and southern shores, underlining tectonic complexity and seismic hazard of this area. Faults shown on this map further indicate the relation of earthquake epicenters with active tectonic structures

and demonstrate the crucial need for continuing seismic monitoring and risk assessment in this very active area. The earthquake data used in this study were obtained from the KOERI Earthquake Catalog (Boğaziçi University Kandilli Observatory and Earthquake Research Institute), accessible at www.koeri.boun.edu.tr/sismo/zeqdb/.

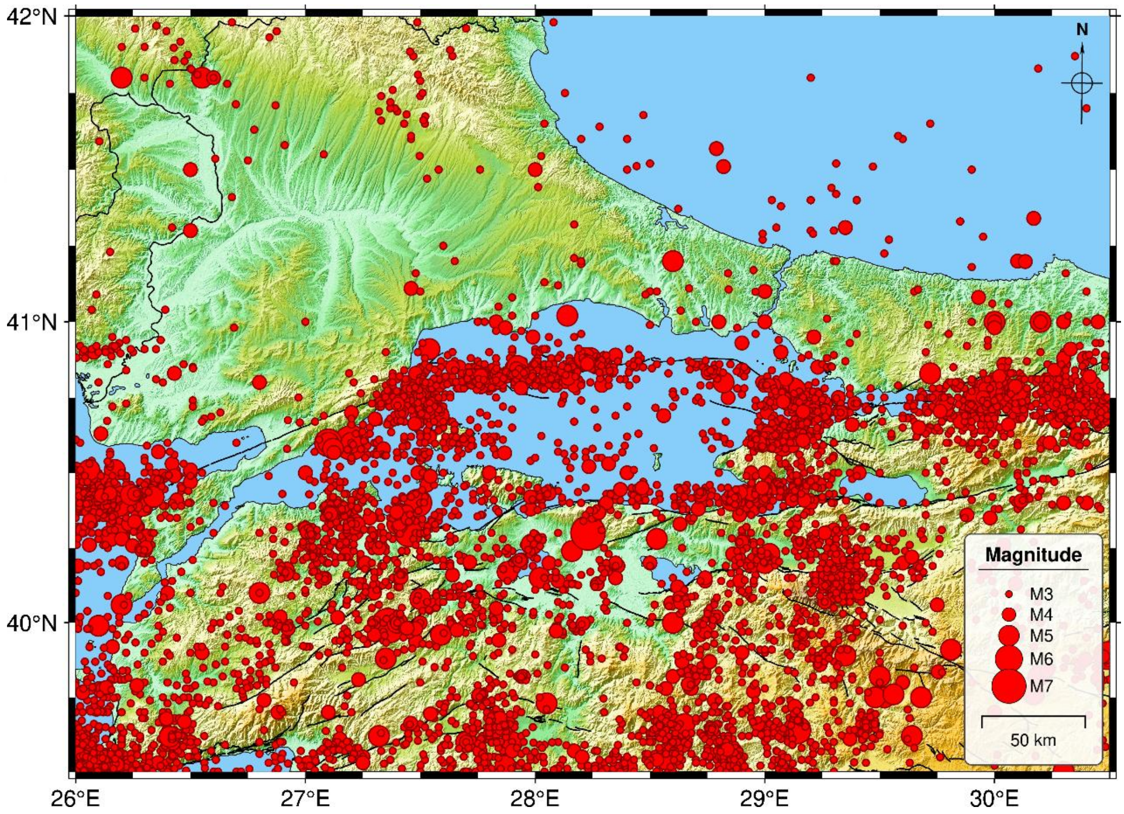

Figure 2.3. The seismicity of the Marmara Region (NW Turkey) and İstanbul Metropolitan area is marked by a dense distribution of seismic events. (1950-2025 February, KOERI)

3. DATA AND METHODOLOGY

3.1. Data

In this study, strong-motion accelerometer data recorded from AFAD (Disaster and Emergency Management Authority) stations in Istanbul were used to analyze the Mw 5.7 earthquake on September 26, 2019. This offshore event took place along the Kumburgaz segment of the North Anatolian Fault Line in the Marmara Sea, with a magnitude of Mw 5.7 and a depth of 6.99 kilometers. It had a strong impact, on the nearby cities such as for example, in places like Tekirdağ and Istanbul but were also felt in cities around the Sea of Marmara including Yalova, Kocaeli, Bursa, and Kırklareli. Considering the distance of the stations to the earthquake source (~40 to 90 km) the 2019 Silivri earthquake is a suitable source as it generates sufficient long period energy and is also close enough to focus on SH waves rather than surface waves which would dominate for earthquakes that are further away.

The stations were included in this study to the analysis are 3405, 3406, 3407, 3408, 3411, 3412, 3413, 3416, and 3417. Geological structure beneath these stations (Figure 3.2) differs, resulting in large differences of velocity profile in each site. The geological conditions of these stations, along with amplification factors and Vs values, were received from the reports prepared by AFAD. These values reflect the average site conditions of each station and for understanding site-specific effects on ground motion.

A summary of the station-specific data such as location, geological feature, amplification factor, and average Vs are given in the Table 3.1. below.

Correspondingly, based on the site classifications provided by TBEC, class ZA represents hard rock with VS30 > 1500 m/s, class ZB is rock with VS30 between 760–1500 m/s, class ZC is dense soil or soft rock with VS30 between 360–760 m/s, and class ZD represents stiff soil with VS30 between 180–360 m/s. Following the MTA Geology map, sedimentary rocks are grouped accordingly: Al refers to alluvium; CCl to continental clastic rocks; CaCl to carbonate and clastic rocks; and ClCa to clastic and carbonate rocks. Besides, the ages of rocks are shown by Q for Quaternary, M for

Miocene, Ol for Oligocene, C for Carboniferous, D for Devonian, and S for Silurian, and O stands for Ordovician.

Table 3.1. Station Information

Station Code	Lat	Lon	District	Geology	VS30 (m/s)	AFAD Site Class	Amplification Factor
3405	40.9111	29.1567	Kartal	CCl (O)	1862	ZA	1.77
3406	41.0226	29.1588	Umraniye	ClCa (S)	436	ZC	No Info
3407	41.0582	29.0095	Beşiktaş	No Info	596	ZC	No Info
3408	41.0734	28.2557	Silivri	No Info	740	ZB	No Info
3411	41.0119	28.9761	Fatih	CCl (M)	323	ZD	1.5
3412	41.0206	28.5782	Buyukcekmece	Al (Q)	247	ZD	4.17
3413	41.0943	28.9482	Eyup	CaCl (C)	452	ZC	1.61
3416	40.9747	28.8364	Yesilkoy	CCl (M)	420	ZC	0.9
3417	40.9547	29.2563	Sultanbeyli	CCl (O)	1747	ZA	1.8

A map showing the location of the stations and the epicenter of the earthquake has also been provided to give a fair idea of their spatial distribution (Figure 3.1.).

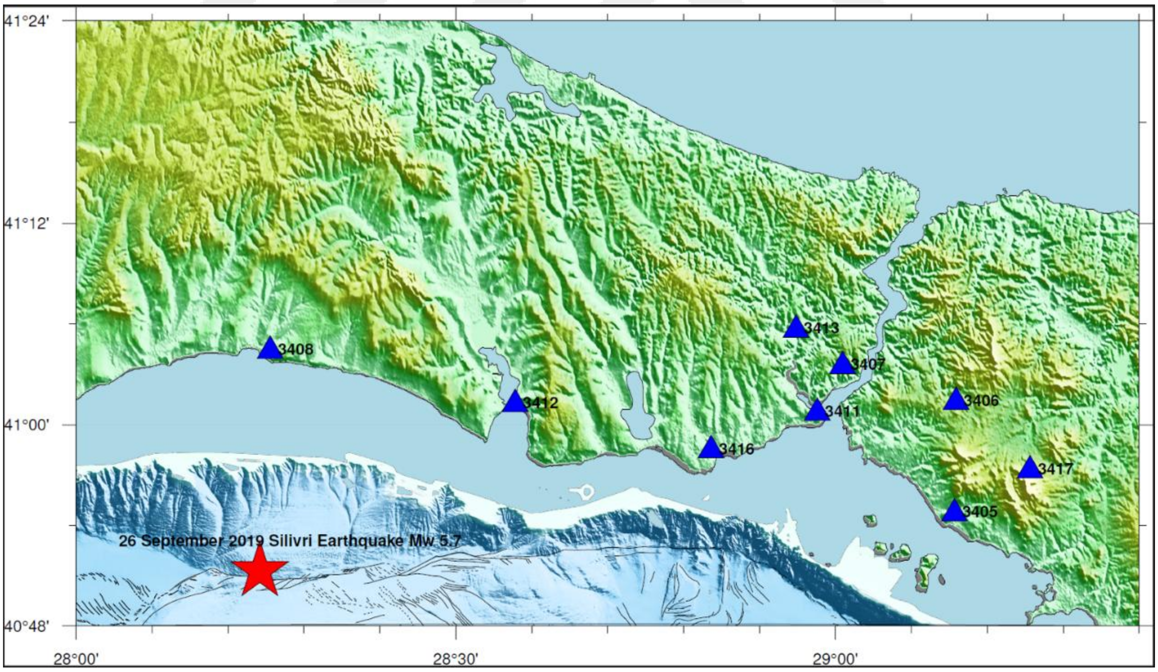

Figure 3.1. AFAD Stations (blue triangles) and Silivri Earthquake Location (red star). The names of the stations are indicated to the right of the triangle that represents the station location.

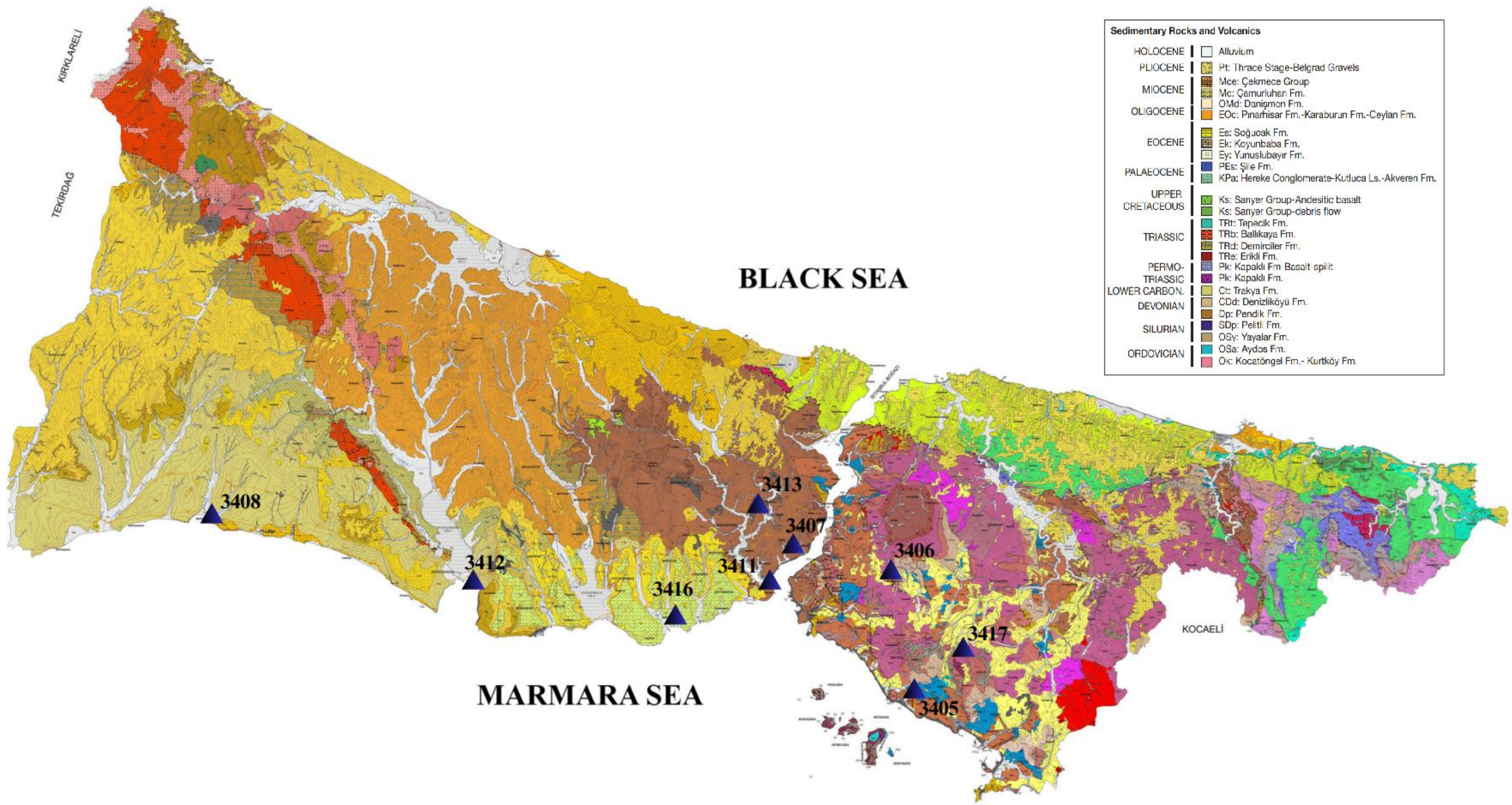

Figure 3.2. Geology of İstanbul and AFAD Station Distribution (Modified from IMM Geology Report Map, 2011)

The distribution of the VS30 velocities prepared by AFAD in Istanbul is also shown in Figure 3.3.

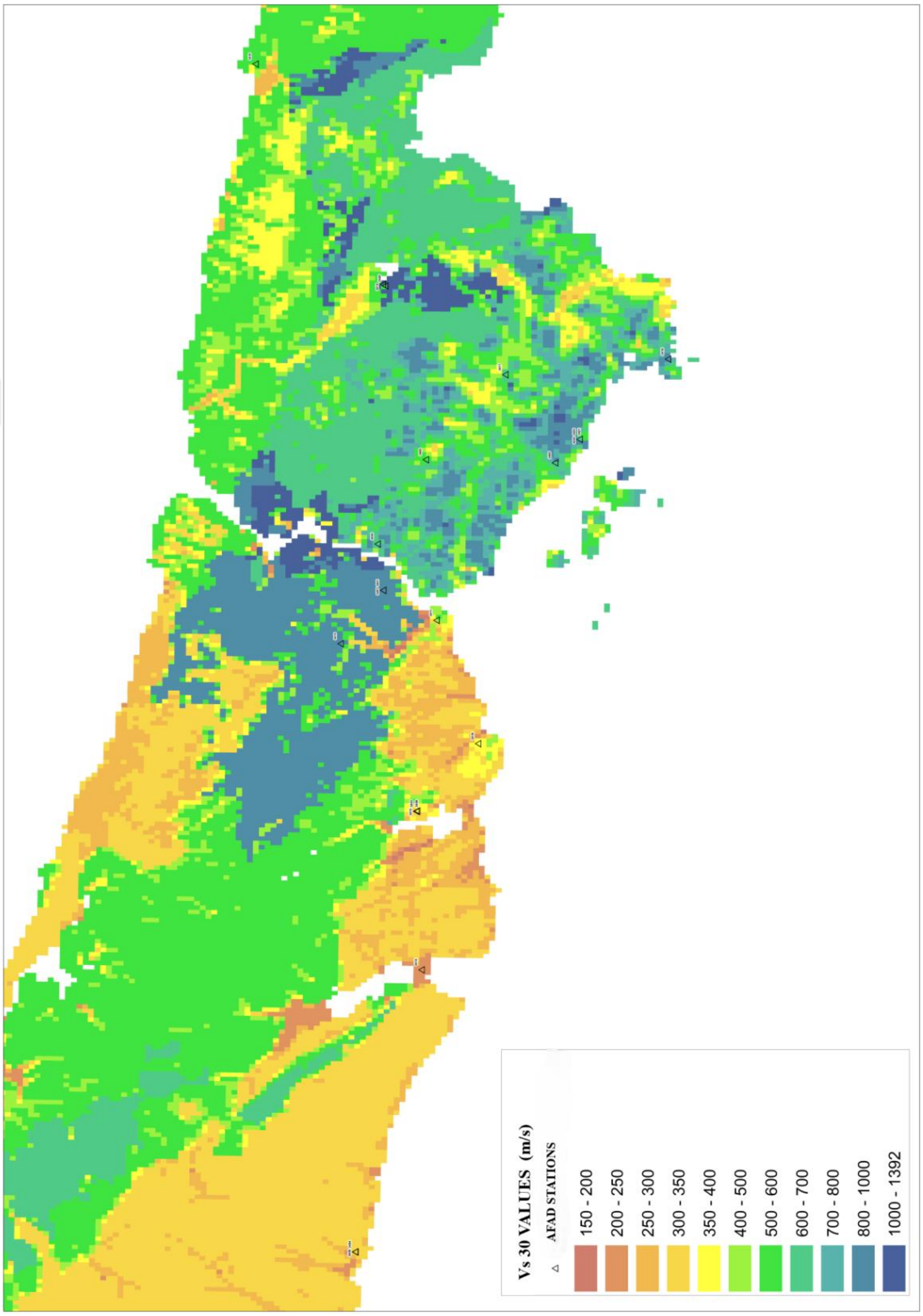

Figure 3.3. AFAD Vs 30 Values for İstanbul

Data and their stationxml response files were downloaded from AFAD website (https://tdvms.afad.gov.tr). Following the removal of the instrument response, event metadata was added to facilitate spatial and temporal analyses. The data were then converted into radial and transverse components, allowing for a more detailed examination of seismic wave propagation. The transverse component of the seismograms was utilized, with a specific focus on SH waves to avoid complex P-to-S and S-to-P conversions, ensuring that only the transfer function of the S wave was used.

For waveform comparison with the synthetic models, acceleration data was converted to displacement data. Displacement data was chosen for comparison with synthetic datasets generated using the crustal velocity models and other site-specific velocity models, ensuring a compatibility test between real and synthetic data.

3.2 Method

3.2.1. Generation of Synthetic Seismograms

Synthetic seismograms for a given earthquake scenario are generated by creating multiple perturbed velocity models, calculating Green's functions, and producing synthetic waveforms. Synthetic seismograms were Generated by the Frequency-Wavenumber method (Bouchon, 1982) using the code FK developed by Zhu and Rivera (2002). Since this method works exclusively with 1D Earth models, it can be used in a very useful and efficient way to simulate seismic wave propagation in a layered medium.

The F-K technique models seismic reactions with high computational efficiency and precision by solving the wave equation in frequency and wavenumber domains through mathematical transformations. The F-K approach, in fact, has gained more recognition for its accuracy and adaptability while generating seismic waveforms to model a wide range of geological situations.

In this technique, the Earth's subsurface is represented as a series of horizontal layers, each characterized by its thickness (h), shear wave velocity (Vs), compressional wave velocity (Vp), density (ρ), and quality factors for attenuation (Qs and Qp). The displacement field within each layer is computed using boundary conditions for stress and displacement continuity at layer interfaces. These conditions ensure accurate modeling of wave reflections and transmissions.

The program calculates Green's functions, which describe the Earth's response to a unit source. These functions are derived in the frequency-wavenumber domain by summing contributions from all layers.

In this analysis, the reference velocity model used will be refered to as "Crustal Model" from Karabulut et al, (2020) and defines the initial subsurface velocity structure. (Table 3.2 and Figure 3.3). This velocity structure was obtained from the 2019 Silivri cluster and was successfully used for earthquake relocation and waveform modeling of both the finite-fault model of the mainshock, and focal mechanisms of foreshocks and aftershocks.

Table 3.2. Crustal Velocity Model (Karabulut et. al, 2020)

Depth (km)	**Vs (km/s)**	**Vp (km/s)**	**Density (g/cm^3)**	**Qs**	**Qp**
2.0	1.79	3.22	2.3	100	200
2.0	2.83	5.09	2.6	200	400
2.0	3.10	5.39	2.6	200	400
4.0	3.20	5.56	2.6	200	400
4.0	3.29	5.73	2.7	400	800
8.0	3.72	6.48	2.9	500	1000
10.0	3.82	6.64	2.9	500	1000
8.0	4.41	7.93	3.2	500	1000
10.0	4.44	7.99	3.2	500	1000
10.0	4.56	8.16	3.2	500	1000

The SAC file, which represents the transverse component, provides the necessary station information, including the station name, azimuth, and distance. The earthquake parameters used for this simulation include a magnitude of 5.7, a depth of 11 km, and a focal mechanism defined by a strike of 282°, a dip of 62°, and a rake of 170° (Karabulut et al., 2020). The source-time function is assumed to be a 4 second triangular function with a 1.6 second rise and 2.4 second fall duration.

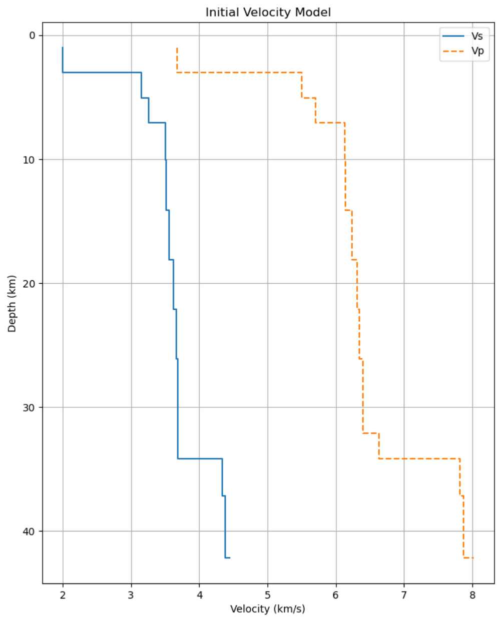

Figure 3.4. Initial Crustal Model from Karabulut et al., (2020)

3.2.2. Calculation of Site-Specific Ground Motions

Synthetic waveforms were first Generated for the 2019 Silivri mainshock using two different approaches to generate input seismograms.

In the first approach, synthetic seismograms were generated directly with input from synthetic waveforms generated at the surface, representing the seismic waves as they arrive at the surface, incorporating the effects of near-surface layers. To account for site effects, two additional layers were introduced on top of the existing crustal model. These layers were placed above a hard rock layer, which was assumed to represent the deeper subsurface structure. This approach allows for assessing how near-surface layers influence seismic wave amplification.

In the second approach, synthetic waveforms were generated at a depth of 2 km, directly beneath the station. This depth corresponds to the base of the first layer in the crustal model, where the seismic waves have not yet been affected by near-surface modifications. These deep synthetic waveforms were then used as input to analyze how seismic waves propagate through the overlying layers. By applying the transfer function of a vertically incident wave, the response of the surface motion was estimated, allowing for a more accurate representation of how the upper layers influence the seismic signal.

To identify the best-fitting station-specific structure, the following procedure was applied:

1. A random shear wave velocity was generated for two layers, ensuring that the velocity of the uppermost layer remained lower than that of the layer beneath it. A random thickness and damping value were assigned to both layers. The remaining portion of the 2 km depth was completed using the velocity of layer 1 from the crustal model (for the second approach) or by assuming a hard rock layer beneath the two newly introduced layers (for the first approach).

2. The transfer function of these two layers was then computed and convolved with the input to generate synthetic waveforms both at the surface and at a depth of 2 km, ensuring that the wave propagation effects were accurately captured for both modeling approaches.

3. The acceleration spectrum of the amplified motion was compared with the data spectrum within the frequency range will be given in the result section correspondingly.

4. The best-fitting models were obtained by optimizing the objective function at each frequency point, which is defined as:

$$E = \sum_{i=1}^{N} \left| \log(\frac{A_d(f_i)}{A_s(f_i)}) - 1 \right|$$

$A_d(f_i)$ *and* $A_s(f_i)$ *are the amplitudes of the data and synthetic waveforms at the discrete frequency* f_i.

5. Finally, the process was reverted back to the time domain, where the best-fitting site-specific model was used to compute synthetic displacement waveforms and compare them with the observed data. For the time-domain synthetic waveforms, P-wave velocities were also required, which were estimated using the empirical relationship by Kitsunezaki et al. (1990):

$$Vp = 1.29 \times Vs + 1.11$$

where Vs and Vp are expressed in meters per second (m/s).

The best-fit models are selected from a total of 5000 models. The ranges for layer thickness and Vs are determined based on the subsurface structure of the selected station, as provided in the AFAD station reports and are tabulated in Table 3.3 For this analysis, the subsurface is modeled with two layers, where the thickness and Vs values of both layers are assigned according to site-specific characteristics. These ranges are informed by geological and geophysical studies of the station's location. The damping parameter is also assigned as site-specific, reflecting the attenuation characteristics of each site. The specific damping values will be presented in the results section.

Table 3.3 Vs, Thickness and Damping Range for Every Station

Station	Vs Range for Layer 1 (m/s)	Vs Range for Layer 2 (m/s)	Thickness Range for Layer 1 (m)	Thickness Range for Layer 2 (m)	Damping Range for Layer 1	Damping Range for Layer 2
3405	100-400	200-600	300-500	600-1000	1-5	0.1-1
3406	300-800	400-1000	100-500	100-1000	1-5	1-5
3407	100-300	200-1500	30-300	100-1500	1-3	0.1-1
3408	100-300	100-1500	100-300	100-1500	1-5	0.1-1
3411	30-200	100-500	30-100	100-1000	1-5	01-0.5
3412	50-300	100-600	30-400	200-1000	0.5-1	0.1-0.3
3413	400-600	200-800	100-300	300-1500	1-3	0.1-1
3416	100-300	100-500	30-200	100-600	1-5	0.1-0.5
3417	600-1000	800-2000	400-600	800-1500	1-3	1-3

4. RESULTS

4.1 Comparison of 2019 Silivri Earthquake Records with Synthetic Waveforms Using the Crustal Model and AFAD's Station Models

In this study, synthetic seismograms generated using two different velocity models the crustal model of Karabulut (2020) and the same model overlayed with station specific velocity values obtained from the reports of AFAD stations are compared. This comparison is conducted to evaluate the precision of these models in relation to real seismic data. In particular, the aim is to assess whether AFAD's station-specific velocity models provide any improvement in predicting SH waveform records at these stations.

The velocity values provided for the first two layers in the AFAD reports were incorporated into the crustal model as additional layers to ensure consistency within the structural framework of the AFAD-based model. The tangential displacement data recorded during the 2019 Mw 5.7 Silivri earthquake were then compared with both the AFAD-based model and the crustal model. Significant differences were observed in their performance, highlighting discrepancies in the predicted ground motion.

Figure 4.1.- 4.9. show this comparisons. Results indicate that the crustal model used in this study fits well to the stations on hard rock sites 3405, 3406, 3407, 3408 and 3417. While the direct SH phase is well-fit in most stations, the reverberations observed in the recordings cannot be generated by the crustal model. In the case of soft soil sites (3411, 3412,3413 and 3416), the crustal model does not yield similar good agreement. This is due to the fact that the crustal model was originally developed for hard rock sites, and therefore is less suitable to represent softer surface conditions. The amplification factor for each station will be provided in the corresponding results section.

The addition of station-specific layers provided by AFAD does not result in any improvement in these fits. It is highly likely that the velocity values given in the reports are not representative of the subsurface structure and therefore fail to accurately capture dynamic site responses.

These results generally indicate that the AFAD-based model is unable to accurately reproduce seismic wave propagation, highlighting the necessity of using well-calibrated crustal models for soft-rock sites. Future studies should focus on refining the models for soft soil sites to achieve better agreement with observed seismic records.

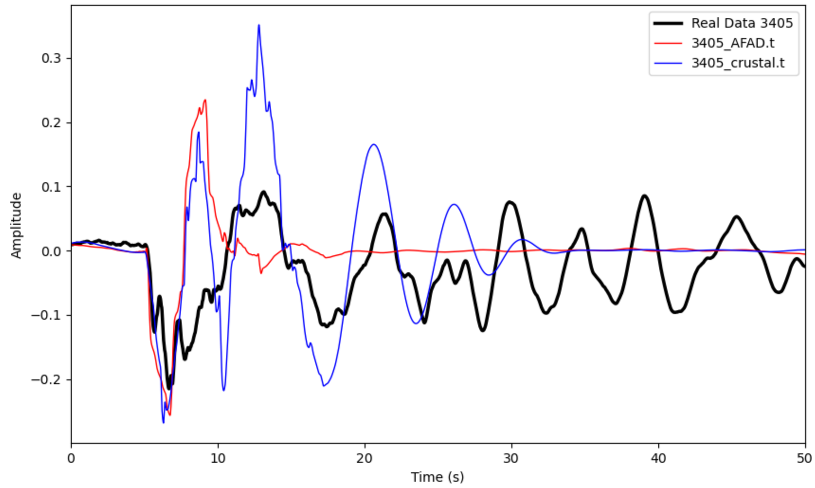

Figure 4.1. Comparison of Tangential Velocity Models for Displacement Recording of Station 3405

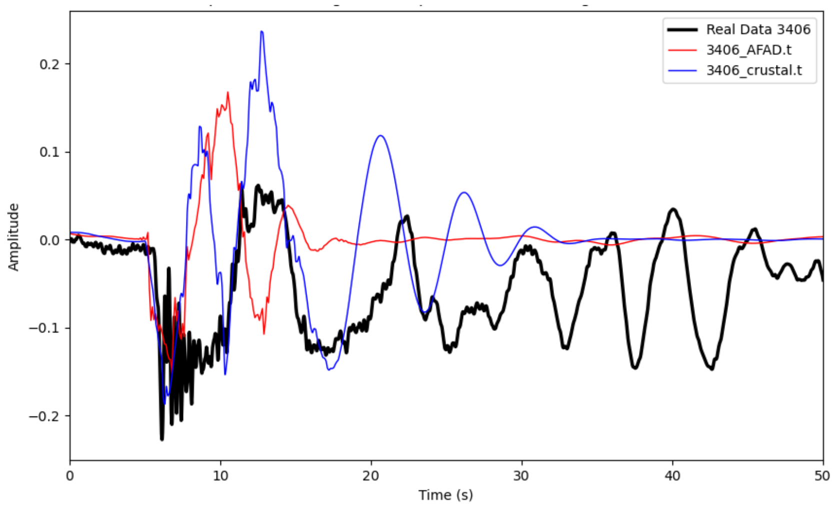

Figure 4.2. Comparison of Tangential Velocity Models for Displacement Recording of Station 3406

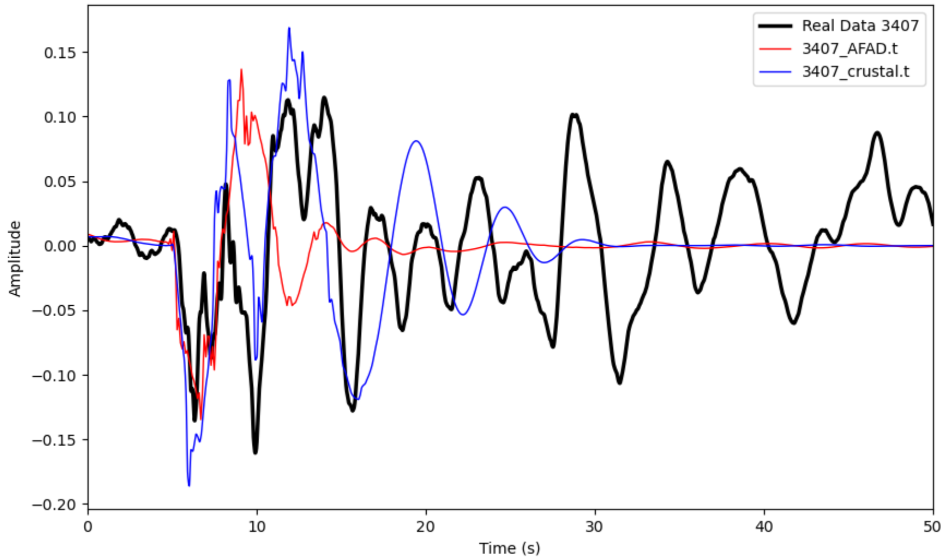

Figure 4.3. Comparison of Tangential Velocity Models for Displacement Recording of Station 3407

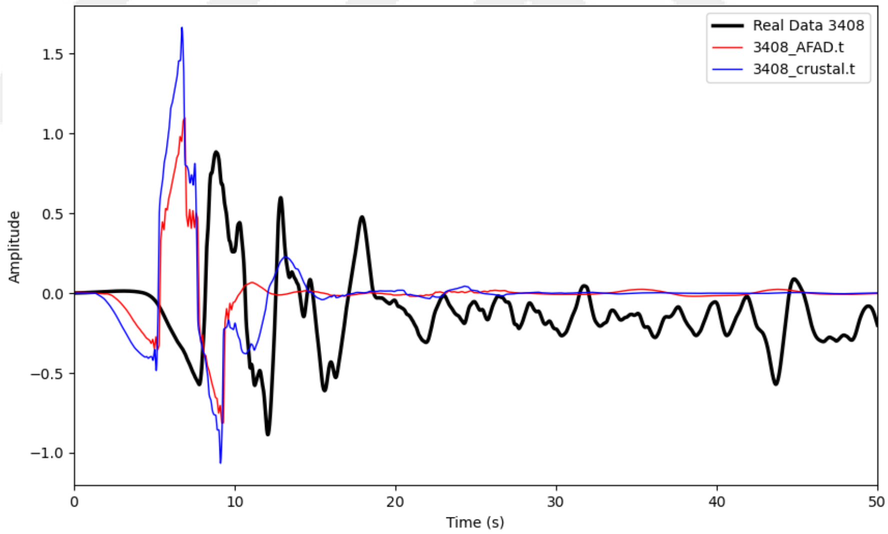

Figure 4.4. Comparison of Tangential Velocity Models for Displacement Recording of Station 3408

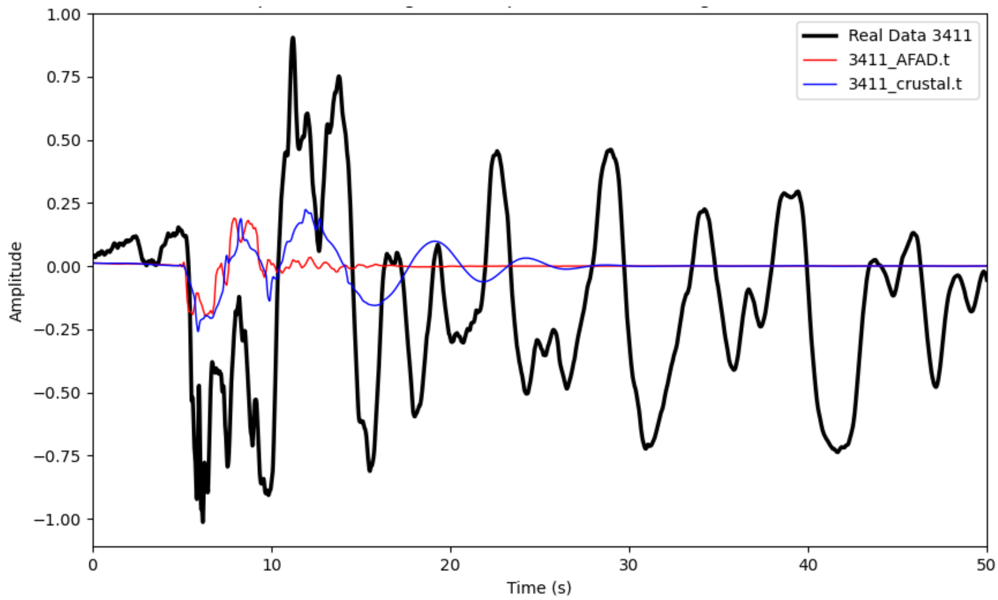

Figure 4.5. Comparison of Tangential Velocity Models for Displacement Recording of Station 3411

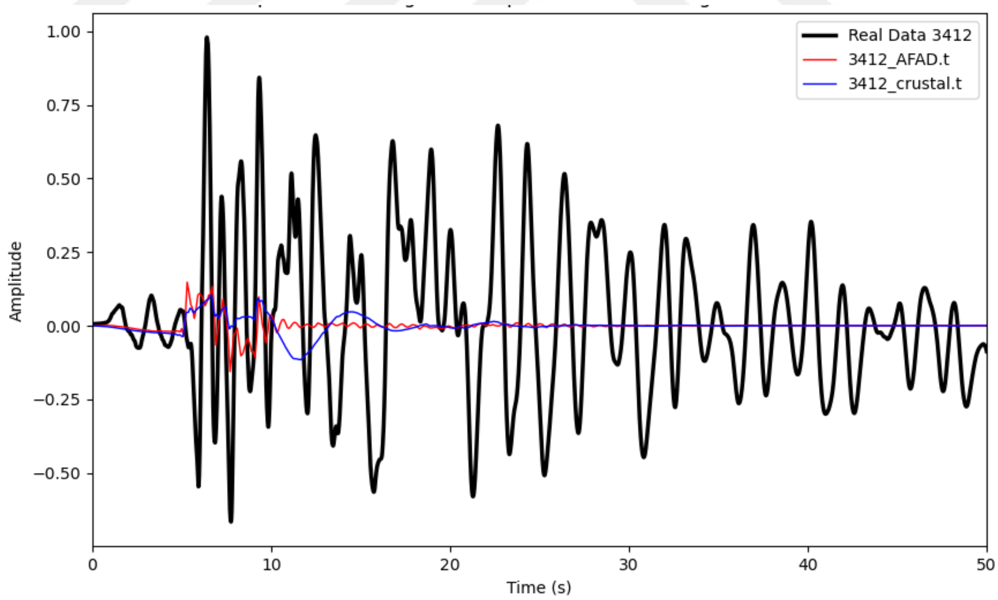

Figure 4.6. Comparison of Tangential Velocity Models for Displacement Recording of Station 3412

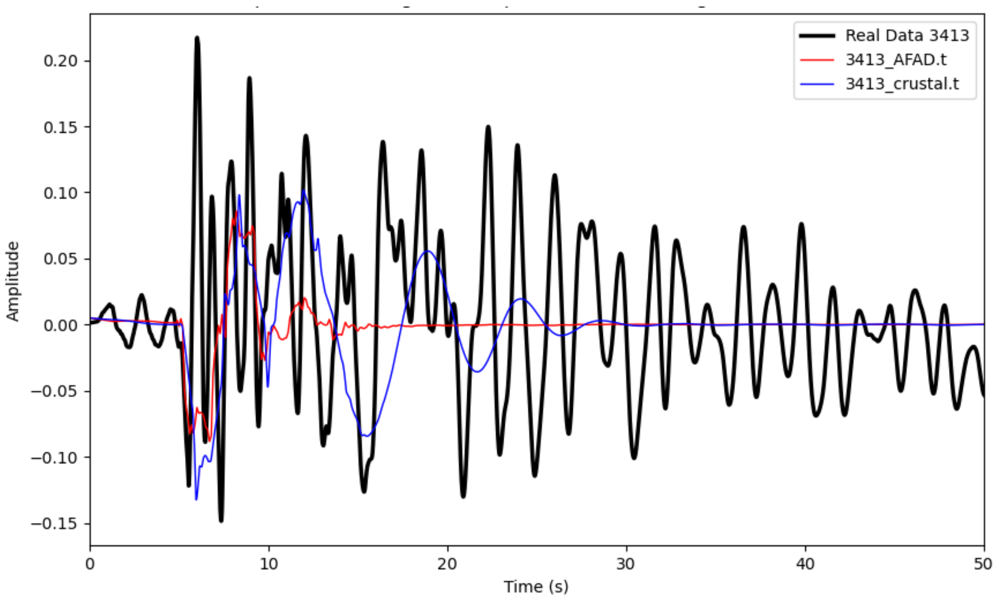

Figure 4.7. Comparison of Tangential Velocity Models for Displacement Recording of Station 3413

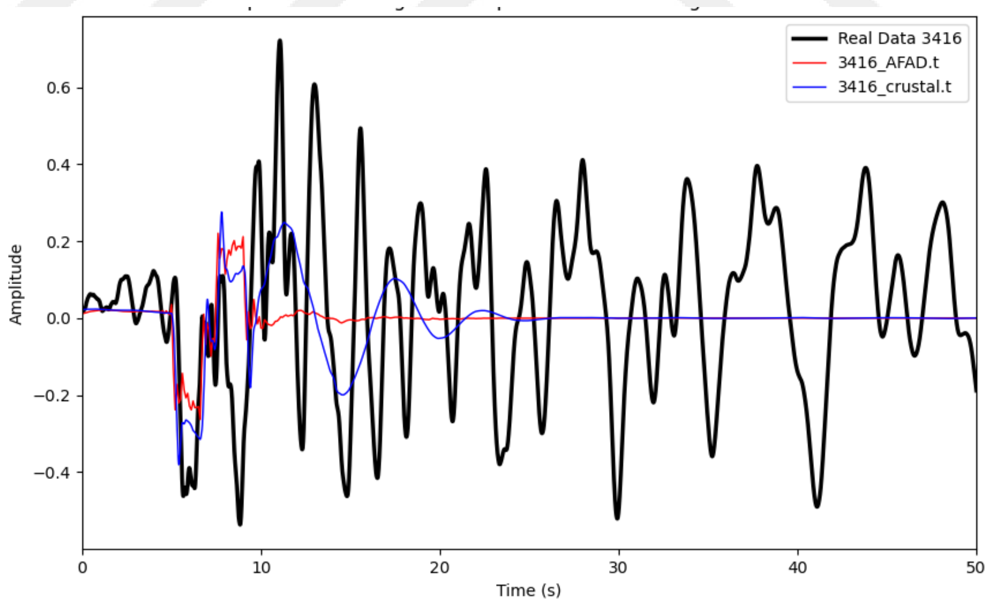

Figure 4.8. Comparison of Tangential Velocity Models for Displacement Recording of Station 3416

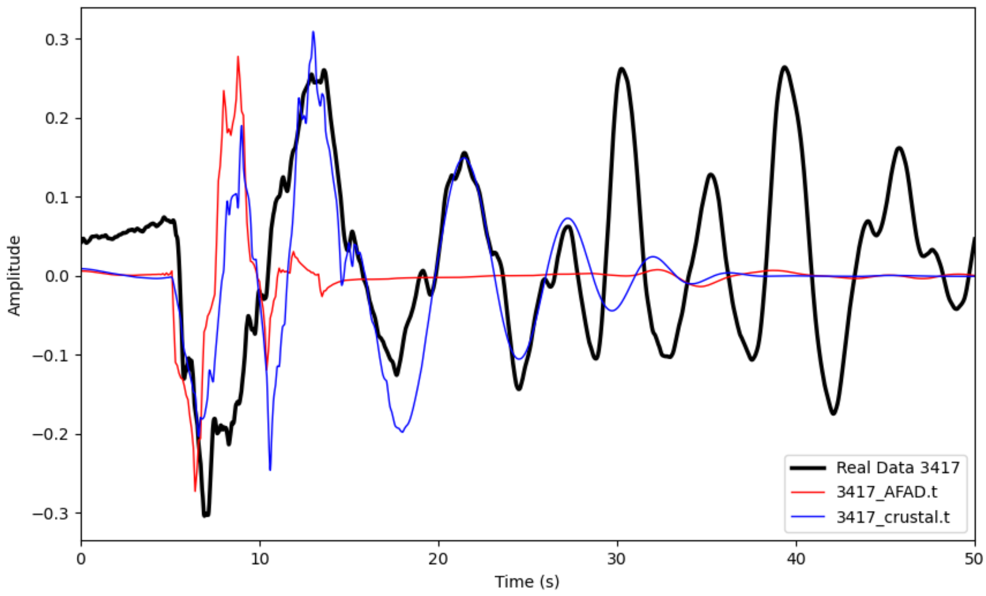

Figure 4.9. Comparison of Tangential Velocity Models for Displacement Recording of Station 3417

4.2 Site Amplification Optimization and Site Specific Shallow Model Optimization

First, the amplification observed with input from synthetic waveforms generated at the surface for the stations exhibiting amplification will be presented. In this part, synthetic waveforms will be compared with time-domain waveforms obtained by convolving them with the transfer function of the optimal two-layer model. After that, the results for the same stations at a depth of 2 km will be shown. In this case, seismograms generated at a depth of 2 km were used as input for site amplification. Additionally, synthetic waveforms obtained using the crustal model will be compared to analyze the differences.

4.2.1 Result of Station 3411

For station 3411, the first layer's thickness was chosen between 10 meters and 100 meters, with Vs values ranging from 30 m/s to 200 m/s, while the second layer's thickness was set between 100 meters and 1000 meters, with Vs values ranging from 100 m/s to 500 m/s. The damping factor was considered within the range of 1-5 for the first layer and between 0.1 and 0.5 for the second layer. These values were selected based on the relatively soft sediments in the area, and the Vs range was derived from reports from AFAD stations.

Figure 4.10. presents the amplification factor calculation at the surface, where the synthetic seismogram from the crustal model was used as input. The time history plot compares the input (red) and output (blue) signals, revealing a significantly high-amplitude output, particularly within the 10-25 second period of the wave, indicating strong site response effects. The bottom-left panel displays the amplification spectrum versus frequency, showing that amplitudes between 0.1 Hz and approximately 5 Hz exceed 20 times the size of the input motion, likely due to impedance contrast within the crust. The bottom-middle panel illustrates the phase shift plot, where an increase in negative phase shift with frequency suggests wave dispersion and frequency-dependent arrival times, typical of varying velocity structures. The Fourier spectra in the bottom-right panel further confirm that the output motion exhibits consistently higher amplitudes than the input, especially between 0.1 Hz and 10 Hz, reinforcing the observed amplification effects.

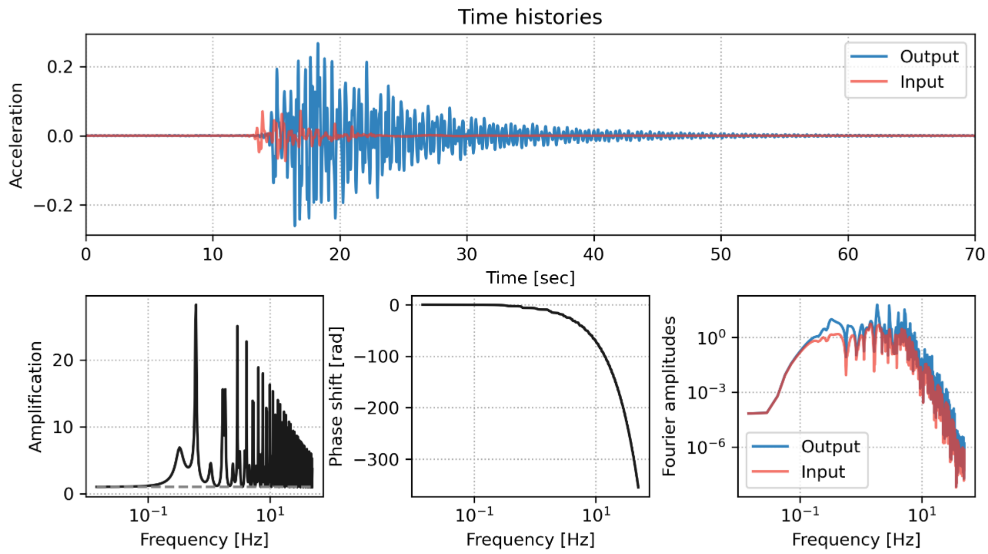

Figure 4.10. Amplification Factor and Fourier Amplitude Comparison of Station 3411 with Input from Synthetic Waveforms Generated at the Surface

Figure 4.11. shows the calculation of the amplification factor at a depth of 2 km, using as input the synthetic seismogram computed from the crustal model. The time history plot in the top panel compares the input (red) and output (blue) signals, where the output motion exhibits significantly larger amplitudes than the input, particularly in the time interval between 10 to 25 seconds, highlighting strong amplification effects. The bottom-left panel presents the amplification spectrum, showing that the principal amplification lies within the range of 0.1 to 5 Hz. Maximum values exceed more than 15 times the input motion, suggesting that in this frequency band, seismic energy is enhanced due to impedance contrasts and resonance effects. The phase shift plot in the bottom-middle panel shows a large negative phase shift that increases further with frequency, implying wave dispersion and travel time variations due to velocity changes in the model. As in previous observations, the amplitudes of the output motion are consistently higher across most frequencies, particularly in the 0.1-10 Hz range, where maximum amplification can be identified. This is further confirmed by the Fourier amplitude spectra in the bottom-right panel. Such observations suggest that significant amplification arises from the crustal model, as lower frequencies lead to wave propagation with greater interaction with the shallow structure and resonant effects.

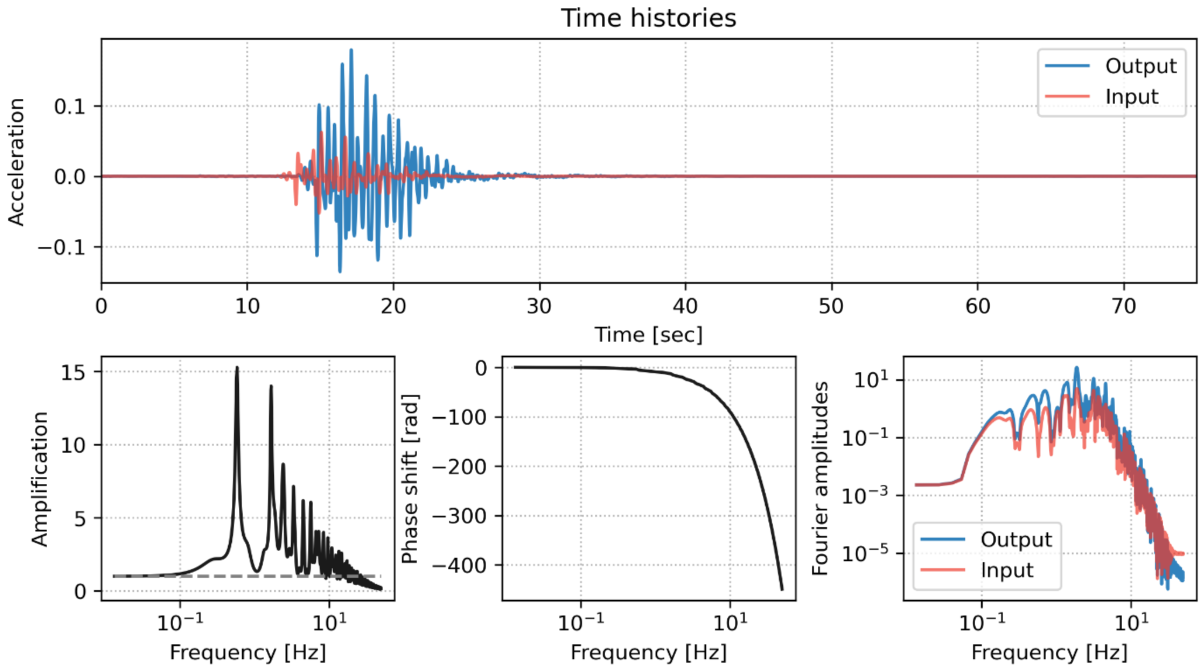

Figure 4.11. Amplification Factor and Fourier Amplitude Comparison of Station 3411 with Input from Synthetic Waveforms Generated at the Depth of 2 km

Figure 4.12. and Figure 4.13. illustrate the depth and Vs velocity of the five generated velocity models at the levels of the surface and -2 km, respectively. Similarly, Figure 4.14. and Figure 4.15. present the comparison between the synthetic waveforms generated using these velocity models and the real data, in the same order.

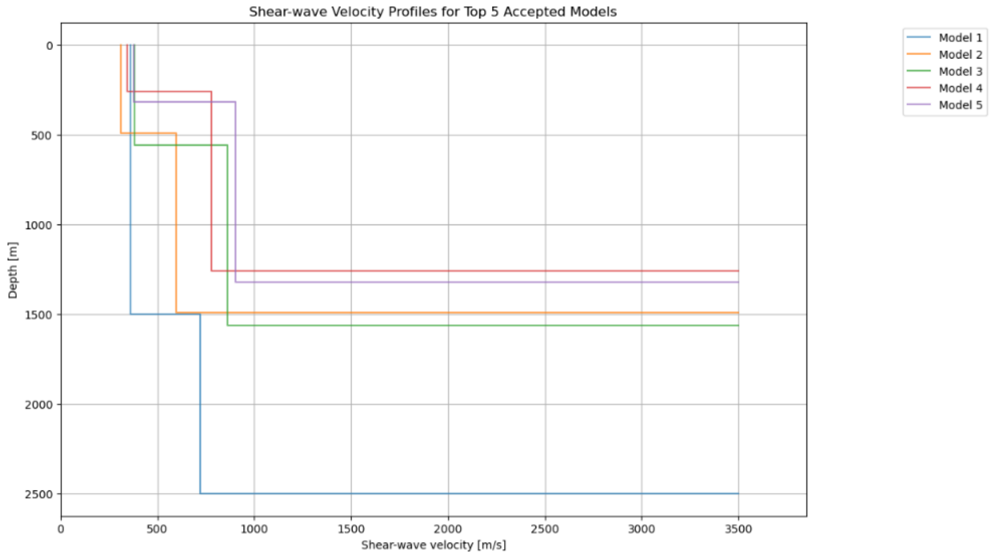

Figure 4.12. Top 5 Accepted Models for Station 3411 with Input from Synthetic Waveforms Generated at the Surface

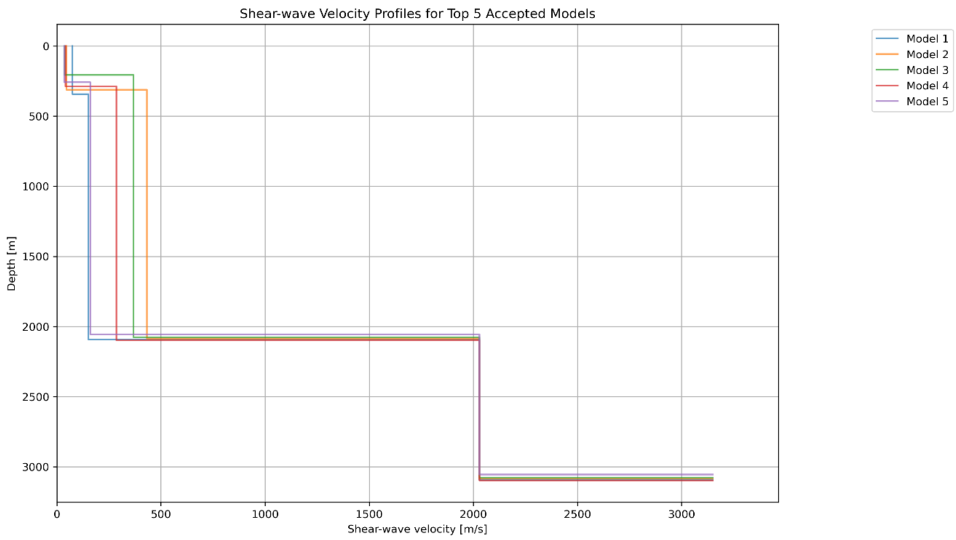

Figure 4.13. Top 5 Accepted Model for Station 3411 with Input from Synthetic Waveforms Generated at the Depth of 2 km

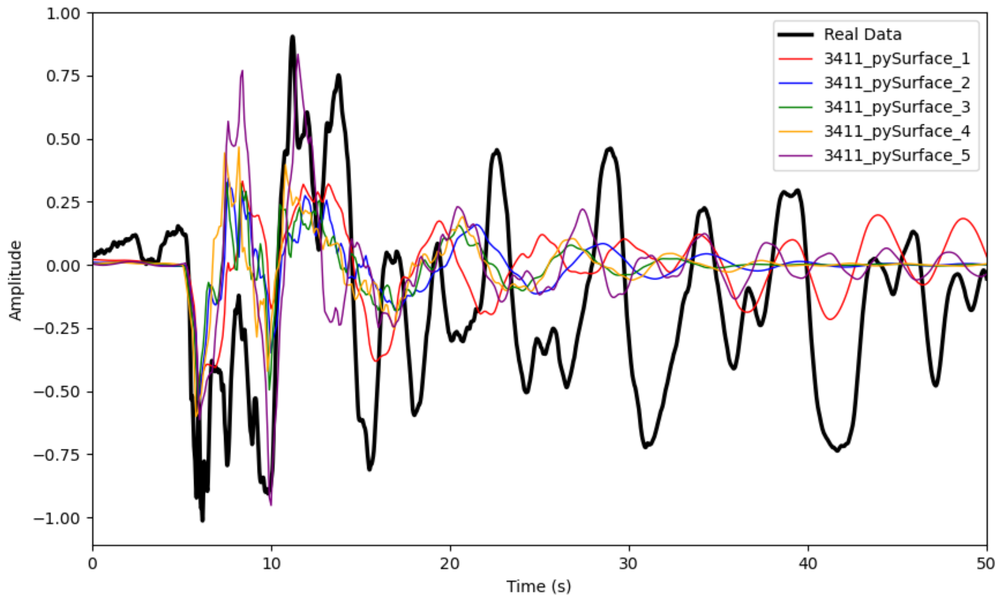

Figure 4.14. Top 5 Accepted Velocity Models Synthetic Waveforms Generated at the Surface vs Real Tangential Displacement Data for Station 3411

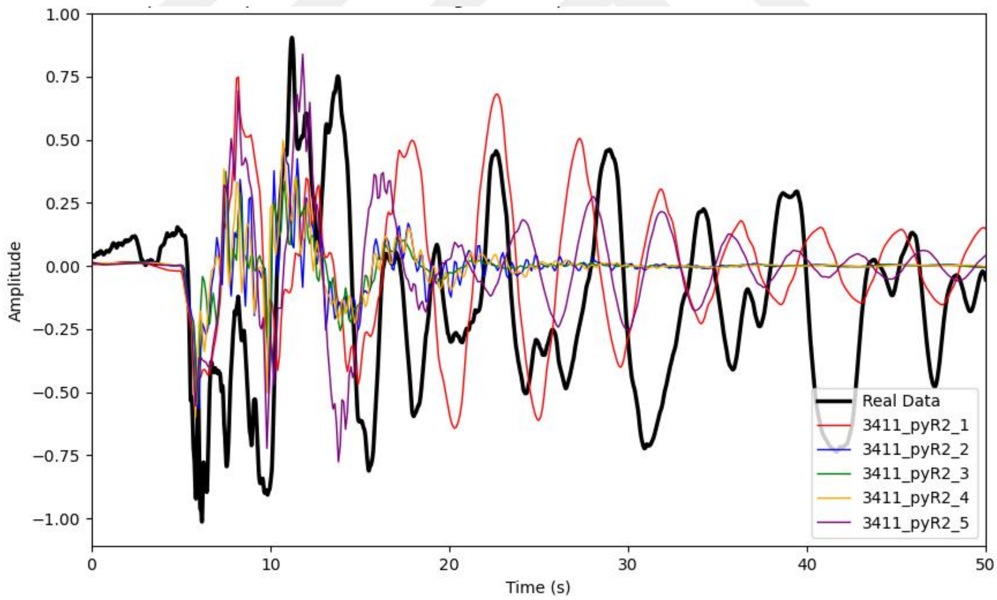

Figure 4.15. Top 5 Accepted Velocity Models Synthetic Waveforms Generated at the Depth of -2km vs Real Tangential Displacement Data for Station 3411

Figure 4.16. shows amplification range at the frequency domain, the amplified synthetic data over real data and the synthetic data which was generated with crustal

structure model over real data, at the with input from synthetic waveforms generated at the surface (left) and the at the depth of -2 km (right) correspondingly.

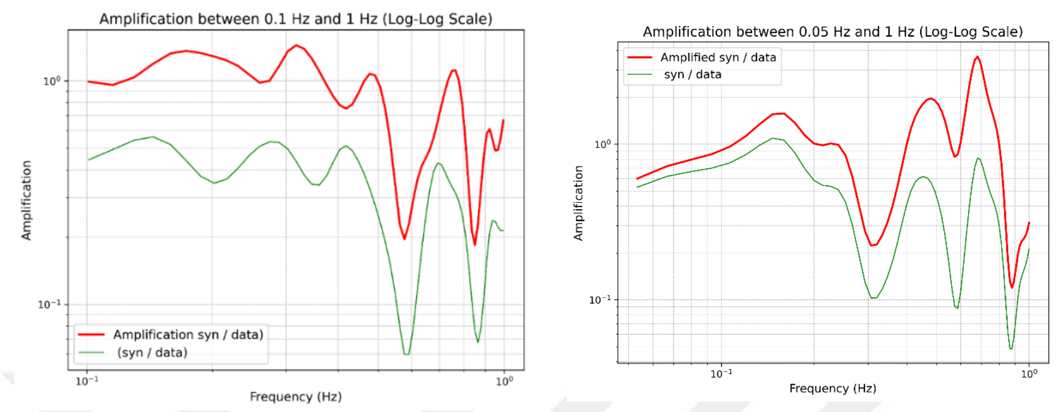

Figure 4.16. Amplification Range at the Frequency Domain for station 3411

4.2.2 Result of Station 3416

For station 3416, the first layer's thickness was chosen between 30 meters and 200 meters, with Vs values ranging from 100 m/s to 300 m/s, while the second layer's thickness was set between 100 meters and 600 meters, with Vs values ranging from 100 m/s to 500 m/s. The damping factor was considered within the range of 1-5 for the first layer and between 0.1 and 0.5 for the second layer. These values were selected based on the relatively soft sediments in the area, and the Vs range was derived from reports from AFAD stations.

Figure 4.17. presents the calculation of the amplification factor at the surface, where the synthetic seismogram from the crustal model was used as input. The time series plot at the top compares the input motion (red) and output motion (blue), showing considerable amplification of surface waves. The bottom-left panel displays the amplification plot, clearly indicating that the amplification exceeds 30 at low frequencies (~0.1-1 Hz) and that this crustal model produces strong amplification within specific frequency bands. The bottom-middle panel shows significant phase delays at low frequencies, suggesting that dispersive effects are introduced by this model. The bottom-right panel presents the Fourier spectra, where larger amplitudes of the output signal at certain frequencies compared to the input signal indicate that the crustal model amplifies these wavelengths.

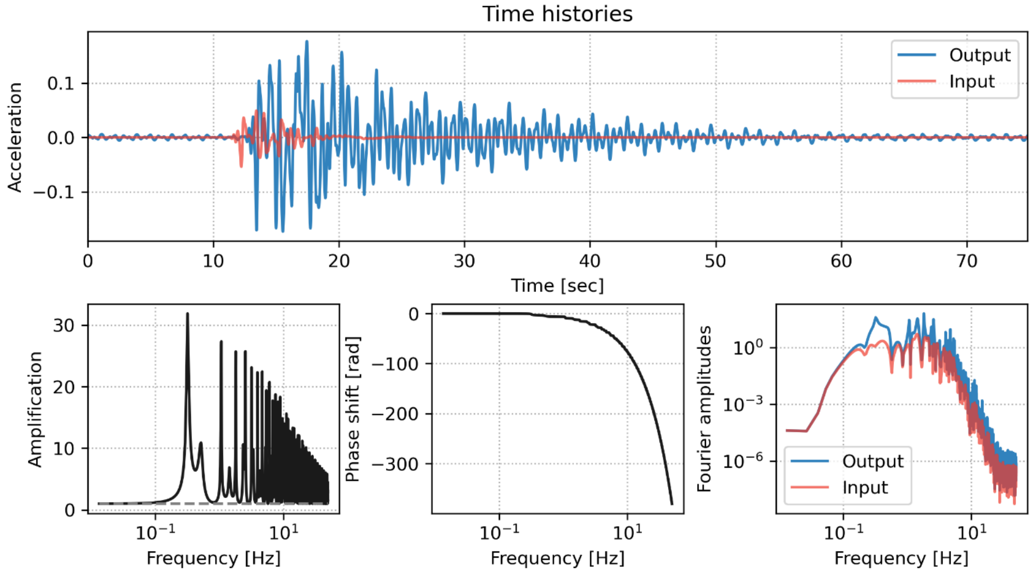

Figure 4.17. Amplification Factor and Fourier Amplitude Comparison of Station 3416 with Input from Synthetic Waveforms Generated at the Surface

Figure 4.18. shows the calculation of the amplification factor at a depth of 2 km, using as input the synthetic seismogram computed from the crustal model. It is quite evident from this plot that there is a significant increase in amplitude within the output signal with respect to the input signal, particularly around 15-20 seconds, suggesting site amplification of seismic waves due to subsurface characteristics. This frequency range also displays in the plot of amplification factor, a strong peak between 0.1-1 Hz—meaning the apparent site resonating within that frequency range. The plot for the phase shift in the case with dependence on the expected frequency shows delays in the wave propagation along with site responses. Besides, the comparison of the Fourier amplitude spectra of input and output signals signifies that this amplification is strong in the 0.1-3 Hz frequency range and decays slowly for higher frequencies. This sort of implication about site velocity structure becomes important regarding the transmission and modification of seismic waves passing through it. It means that there are more peaks in the plot of the amplification factor that could be indicative of impedance contrasts.

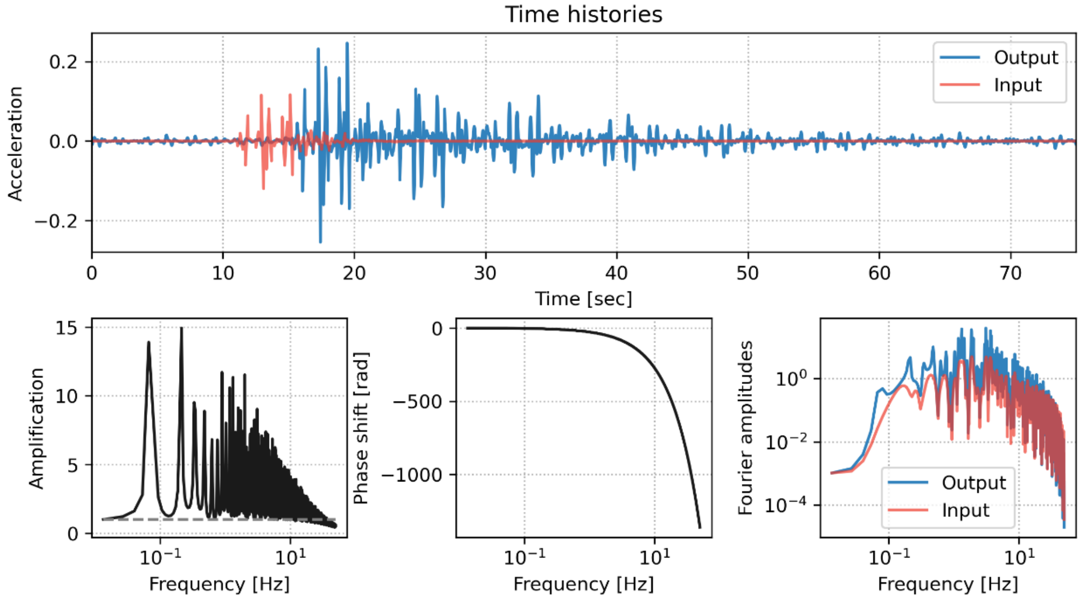

Figure 4.18. Amplification Factor and Fourier Amplitude Comparison of Station 3416 with Input from Synthetic Waveforms Generated at the Depth of 2 km

Figure 4.19. and Figure 4.20. illustrate the depth and Vs velocity of the five generated velocity models at the levels of the surface and -2 km, respectively. Similarly, Figure 4.21. and Figure 4.22. present the comparison between the synthetic waveforms generated using these velocity models and the real data, in the same order.

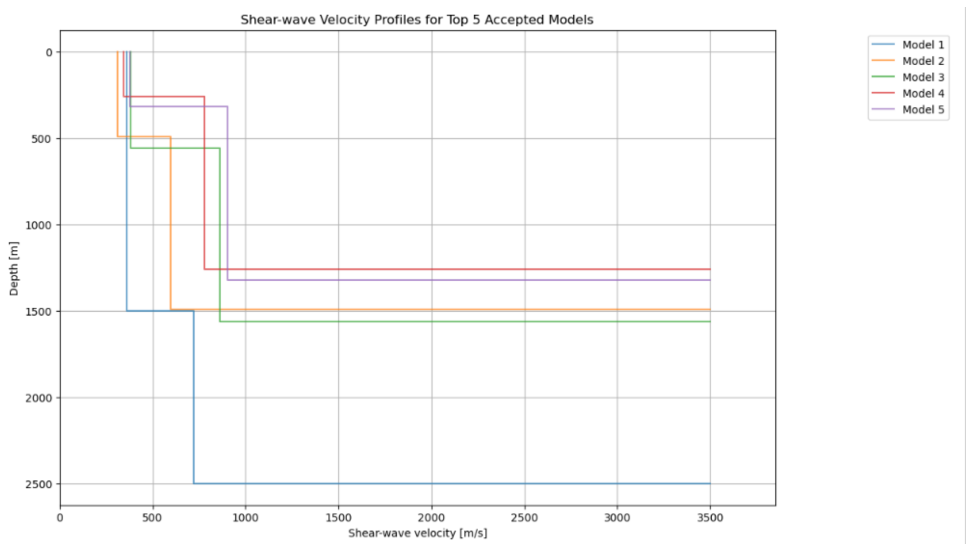

Figure 4.19. Top 5 Accepted Model for Station 3416 with Input from Synthetic Waveforms Generated at the Surface

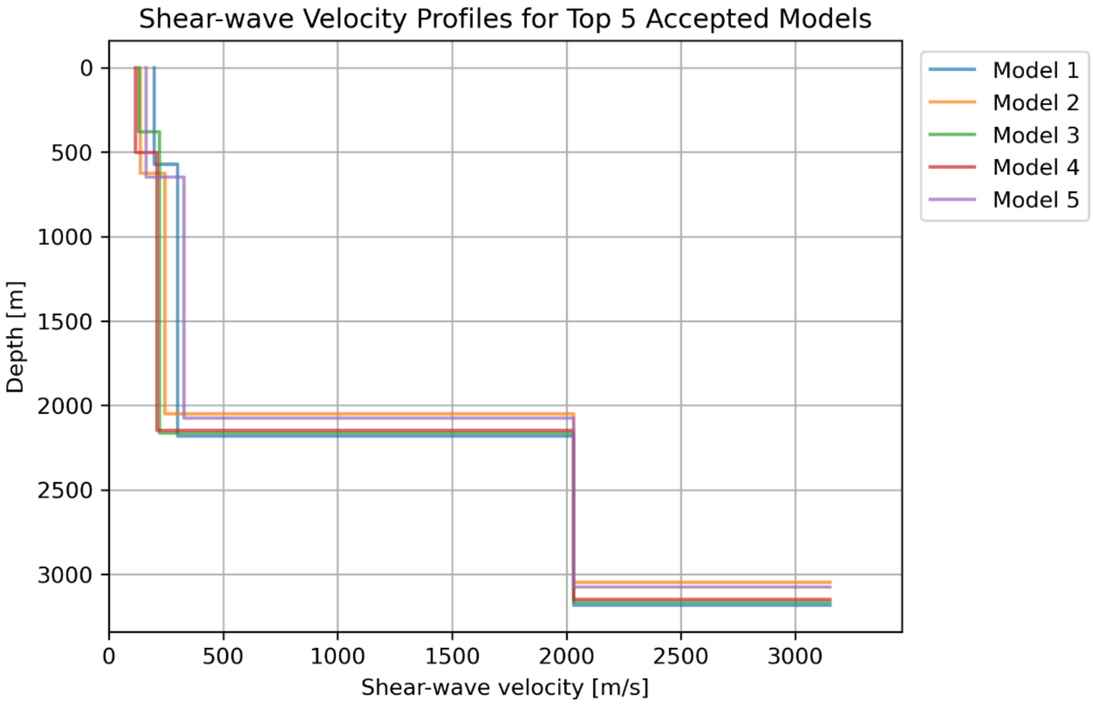

Figure 4.20. Top 5 Accepted Model for Station 3416 with Input from Synthetic Waveforms Generated at the Depth of 2 km

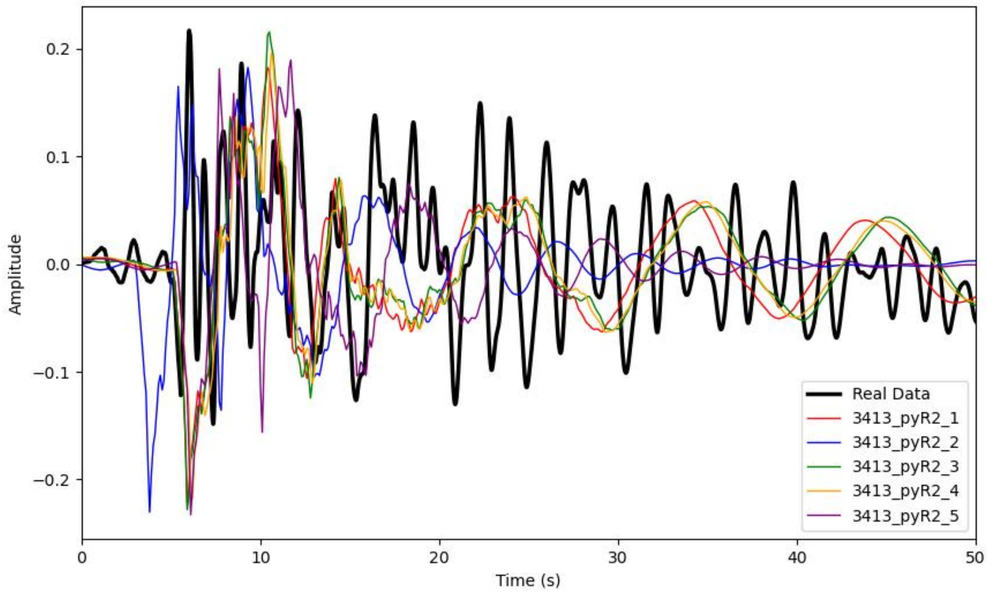

Figure 4.21. Top 5 Accepted Velocity Models Synthetic Waveforms Generated at the Surface vs Real Tangential Displacement Data for Station 3416

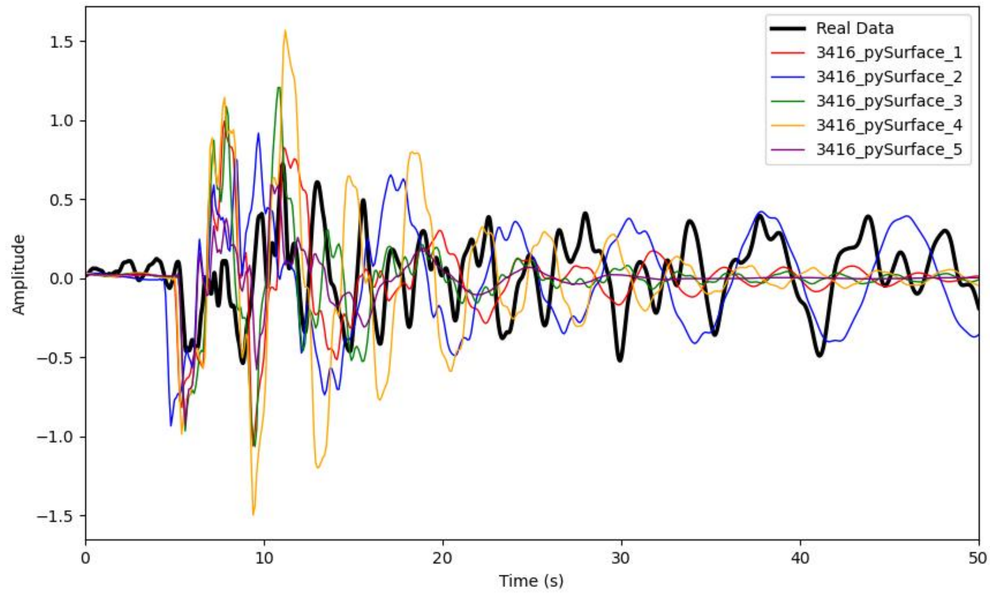

Figure 4.22. Top 5 Accepted Velocity Models Synthetic Waveforms Generated at the Depth of -2km vs Real Tangential Displacement Data for Station 3416

Figure 4.23. shows amplification range at the frequency domain, the amplified synthetic data over real data and the synthetic data which was generated with crustal structure model over real data, with Input from Synthetic Waveforms Generated at the Surface (left) and at the bottom -2 km (right) correspondingly.

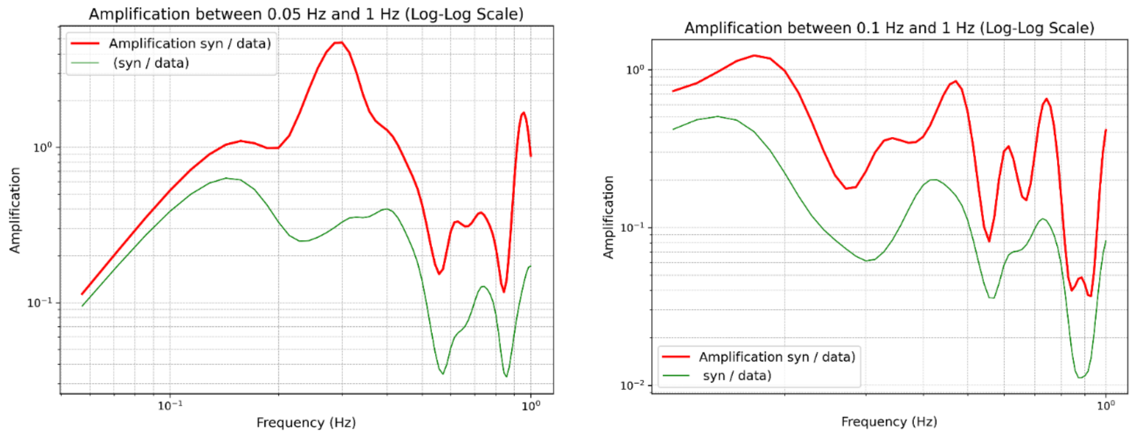

Figure 4.23. Amplification Range at the Frequency Domain for station 3416

4.2.3. Result of Station 3413

In the case of station 3413, the first layer's thickness was chosen between 100 meters and 300 meters with Vs values from 400 m/s to 600 m/s, while the second layer thickness was chosen between 300 meters and 1500 meters with Vs ranging from 200 m/s to 800 m/s. The damping factor has been considered within the range 1-3 for the first layer and between 0.1 and 1 for the second layer. These values have been selected for this area in view of their relatively soft sediments, the range of Vs values was derived based on reports from AFAD stations. Figure 4.24. shows the calculation of the amplification factor at the surface, where the synthetic seismogram from the crustal model has been taken as an input. In the time history plot, the top panel compares the input signal in red and the output in blue; one can notice that, around 15 seconds, the amplitude increases considerably, showing the wave amplification due to the local site effects. The bottom left panel of the amplification spectrum shows that, in the frequency range between 0.2 and 10 Hz, the amplification factor is above 2, with several resonance peaks, which would suggest a strong influence of subsurface layering and impedance contrasts. The phase shift plot shows frequency-dependent delay in wave arrivals, increasing progressively towards lower frequencies. In fact, from the Fourier amplitude spectra of the bottom right panel, it is clear that, for frequencies lower than 1 Hz, according to the amplification trend, higher spectral energy is obtained in the output signal with respect to the input one.

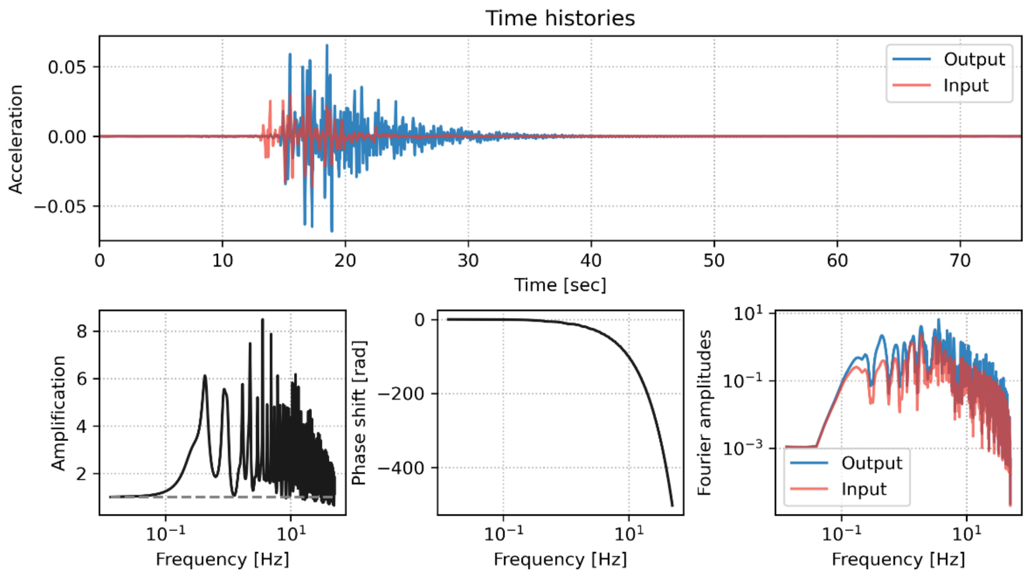

Figure 4.24. Amplification Factor and Fourier Amplitude Comparison of Station 3413 with Input from Synthetic Waveforms Generated at the Surface

Figure 4.25. shows the amplification factor computed using a synthetic seismogram generated with the crustal model. The time history plot (top panel) shows the input waveform (red) and the output waveform (blue), indicating significant amplification in the 10–30 second range, where the output exhibits increased amplitude. The amplification

spectrum (bottom left panel) highlights amplification factors exceeding 2–8 times within the 0.1–10 Hz frequency range, suggesting strong site effects. The phase shift plot (bottom middle panel) reveals a substantial phase delay at lower frequencies, indicating wave dispersion due to subsurface layering. The Fourier amplitude spectra (bottom right panel) show that the output spectrum has a stronger response at lower frequencies compared to the input, reinforcing the observed amplification. These results suggest that the crustal model predicts notable amplification, particularly at long periods, likely due to soft sedimentary layers in the structure

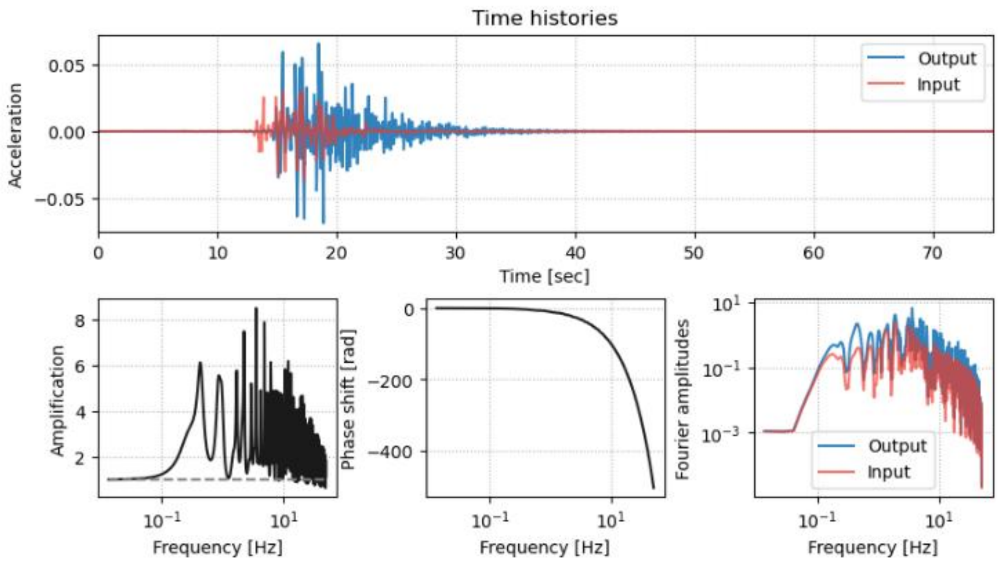

Figure 4.25. Amplification Factor and Fourier Amplitude Comparison of Station 3413 with Input from Synthetic Waveforms Generated at the Depth of 2 km

Figure 4.26. and Figure 4.27. illustrate the depth and Vs velocity of the five generated velocity models at the levels of the surface and -2 km, respectively. Similarly, Figure 4.28. and Figure 4.29. present the comparison between the synthetic waveforms generated using these velocity models and the real data, in the same order.

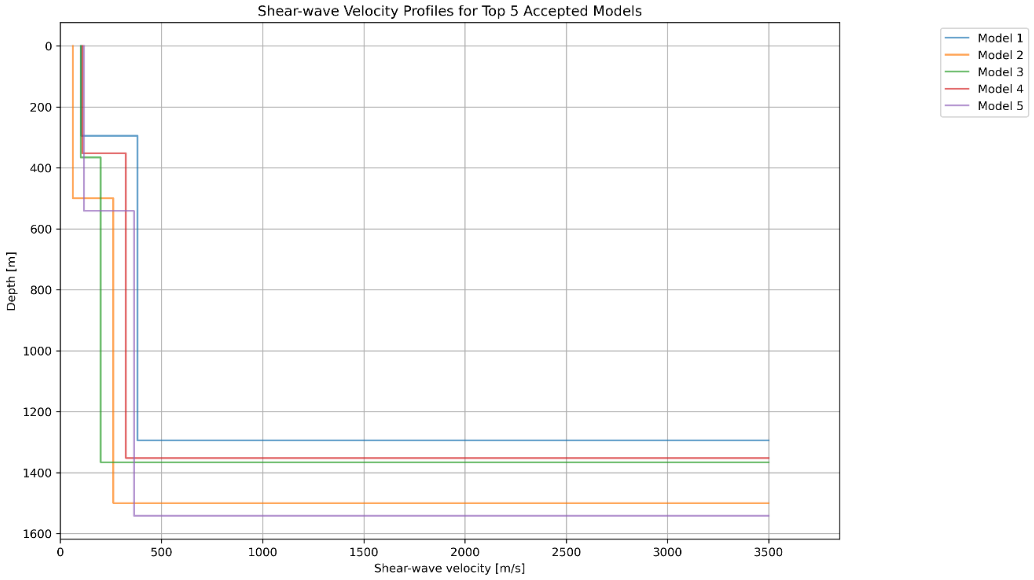

Figure 4.26. Top 5 Accepted Model for Station 3413 with Input from Synthetic Waveforms Generated at the Surface

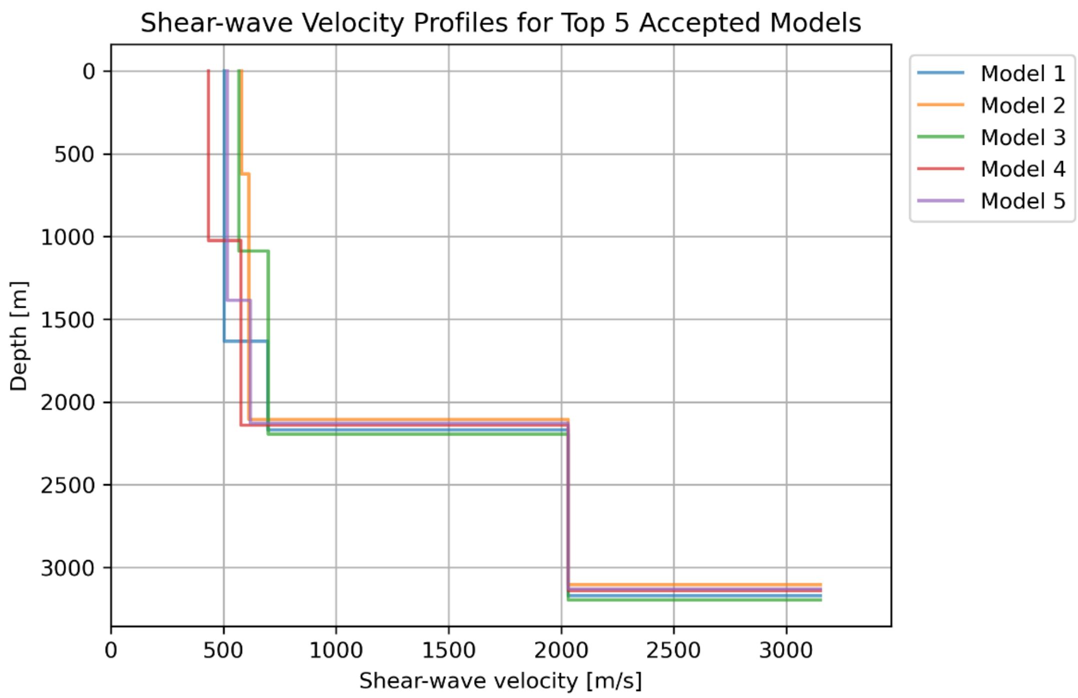

Figure 4.27. Top 5 Accepted Model for Station 3413 with Input from Synthetic Waveforms Generated at the Depth of 2 km

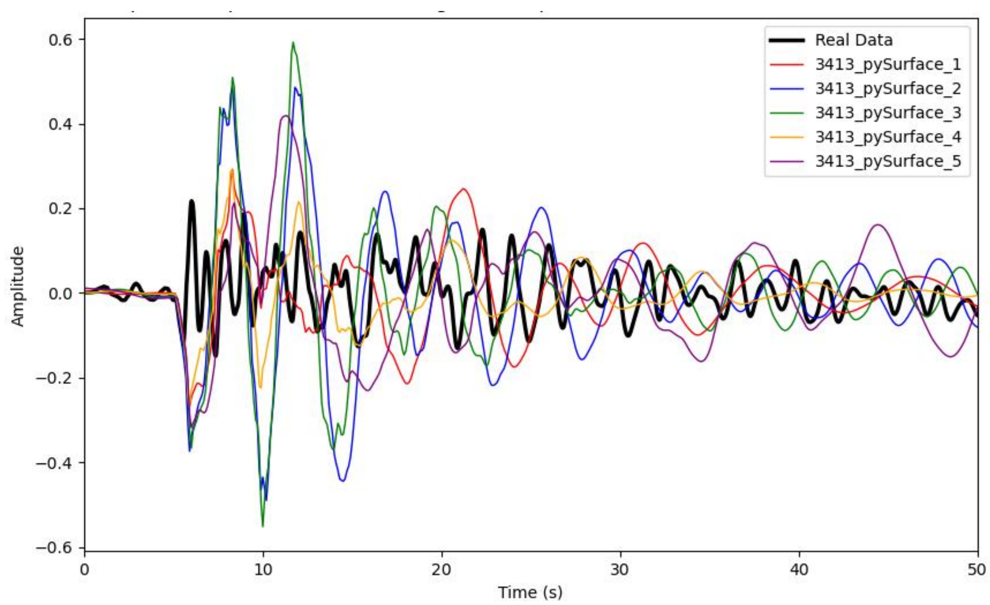

Figure 4.28. Top 5 Accepted Velocity Models Synthetic Waveforms Generated at the Surface vs Real Tangential Displacement Data for Station 3413

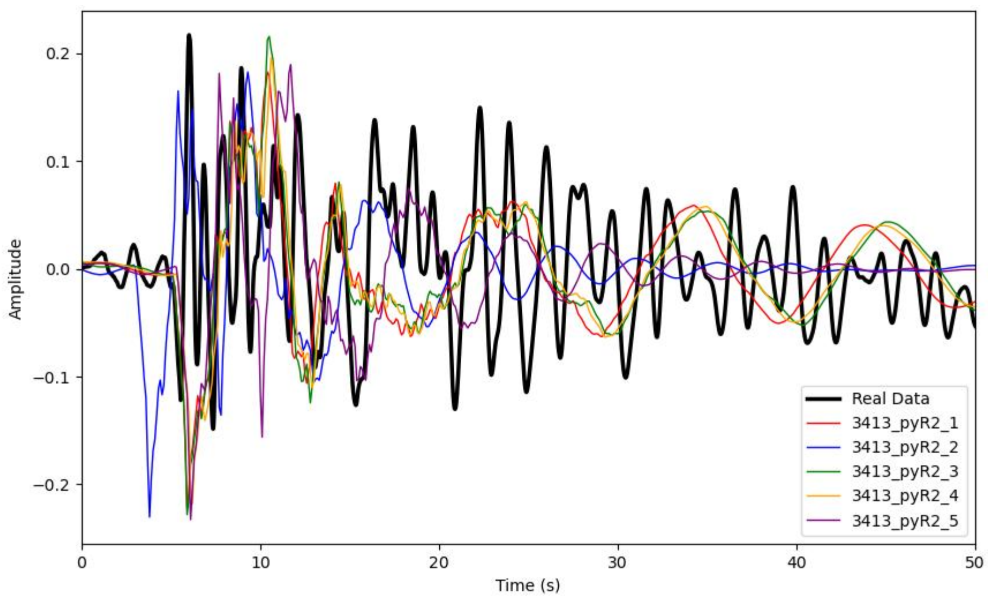

Figure 4.29. Top 5 Accepted Velocity Models Synthetic Waveforms Generated at the Depth of -2km vs Real Tangential Displacement Data for Station 3413

Figure 4.30. shows amplification range at the frequency domain, the amplified synthetic data over real data and the synthetic data which was generated with crustal structure model over real data, at the with Input from Synthetic Waveforms Generated at the Surface (left) and at the depth -2 km (right) correspondingly.

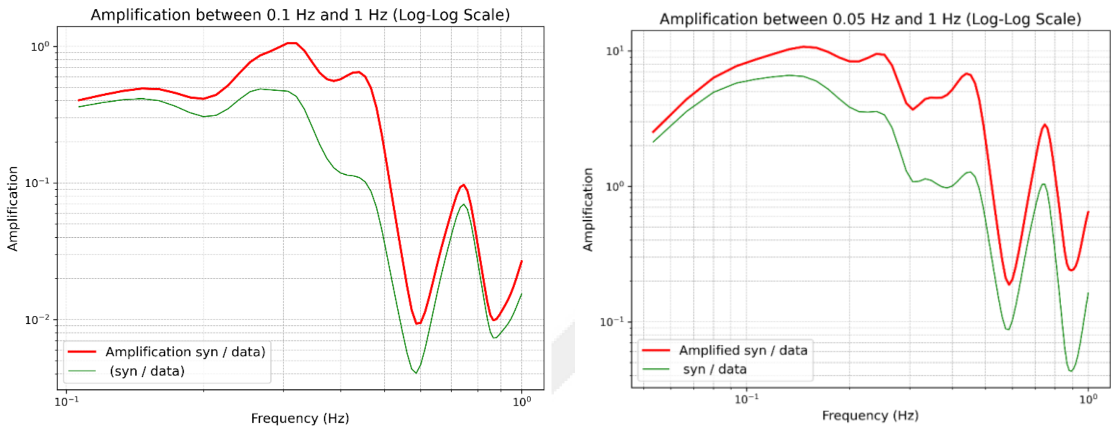

Figure 4.30. Amplification Range at the Frequency Domain for station 3413

4.2.4. Result of Station 3407

In the case of station 3413, the first layer's thickness was chosen between 30 meters and 300 meters with Vs values from 100 m/s to 300 m/s, while the second layer thickness was chosen between 100 meters and 1500 meters with Vs ranging from 200 m/s to 1500 m/s. The damping factor has been considered within the range of 1-3 for the first layer and between 0.1 and 1 for the second layer. These values have been selected for this area in view of their relatively soft sediments, and the range of Vs values was derived based on reports from AFAD stations. Figure 4.31. shows the calculation of the amplification factor at the surface, where the synthetic seismogram from the crustal model has been taken as an input. The time history plot above shows the input in red and the output in blue after amplification, with the output indicating a substantial increase in amplitude from 15 to 30 seconds, reflecting significant site response effects. The spectrum of amplification shows that the more relevant amplification falls in the range between 0.1 Hz and 5 Hz, with peak values that exceed more than 15 times the input, which could suggest resonance effects caused by impedance contrasts in crustal structure. Also, as seen from the plot of the phase shift, there is strong delay for higher frequencies that could imply strong effects of wave dispersion while seismic waves travel through different layers. The amplitude spectra in the bottom right panel of the Fourier amplitude confirm that indeed, much larger amplitude components characterize the output motion than the input, especially within the frequency window between 0.1 and 10 Hz, reinforcing the observed trend of amplification. These results would therefore imply a substantial amount of amplification, induced by the crustal model, mostly within the low-to-mid frequency range, underlining the role of subsurface layering and resonance effects on wave propagation.

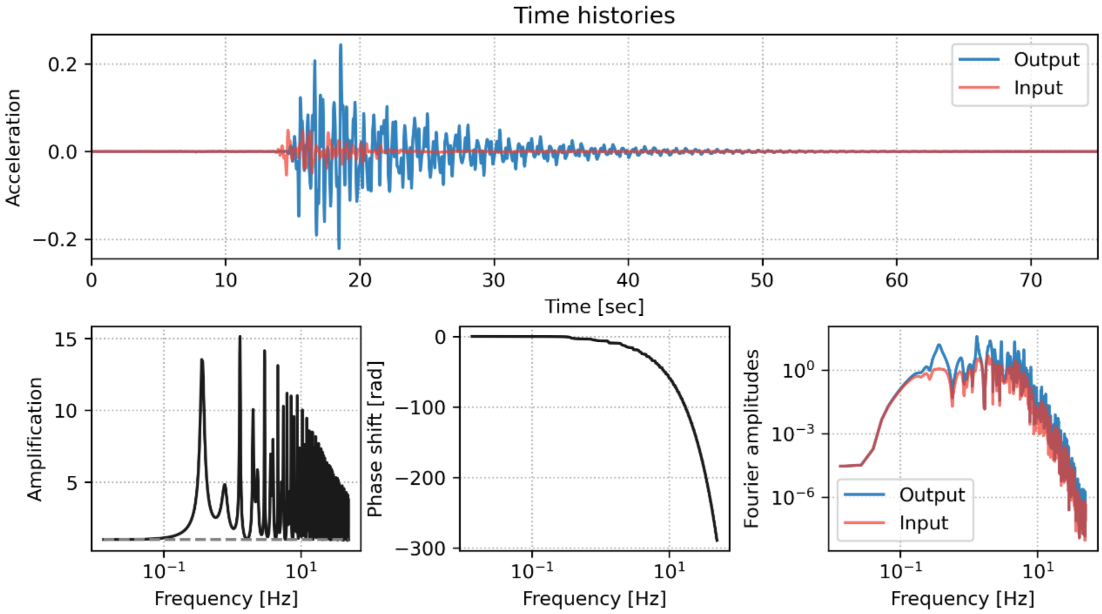

Figure 4.31. Amplification Factor and Fourier Amplitude Comparison of Station 3407 with Input from Synthetic Waveforms Generated at the Surface

Figure 4.32. shows the computation of the amplification factor using as input a synthetic seismogram obtained from the crustal model. The time history plot (top panel) compares the input (red) and output (blue) signals, where the latter is highly amplified, especially between 15 and 30 seconds, indicating a very strong site response. The bottom-left panel presents the amplification spectrum, which represents the most coherent source of amplification, occurring within the range of 0.1 Hz to 5 Hz, with peak values exceeding 10 times the input motion. This observation suggests that seismic energy is significantly enhanced by the crustal model within this frequency range due to impedance contrast and resonance effects. The phase shift represents a strong delay for the high-frequency wave dispersion. The Fourier amplitude spectra, below right, confirm indeed that at most

frequencies, the output motion provides higher amplitudes, especially within the 0.1-10 Hz frequency range, corroborating the above trends of amplification. All the above results provide general support that the crustal model introduces noticeable amplification with regard to waves at lower frequency, where characteristics of site responses are relevant to seismic waves.

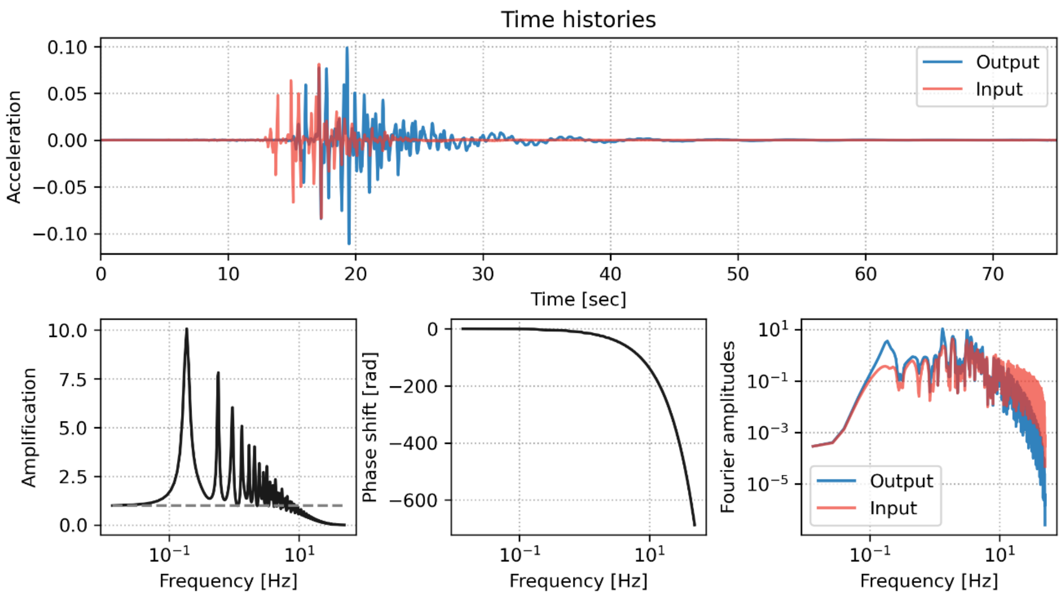

Figure 4.32. Amplification Factor and Fourier Amplitude Comparison of Station 3407 with Input from Synthetic Waveforms Generated at the Depth of 2 km

Figure 4.33 and Figure 4.34 illustrate the depth and Vs velocity of the five generated velocity models at the levels of the surface and -2 km, respectively. Similarly, Figure 4.35 and Figure 4.36 present the comparison between the synthetic waveforms generated using these velocity models and the real data, in the same order.

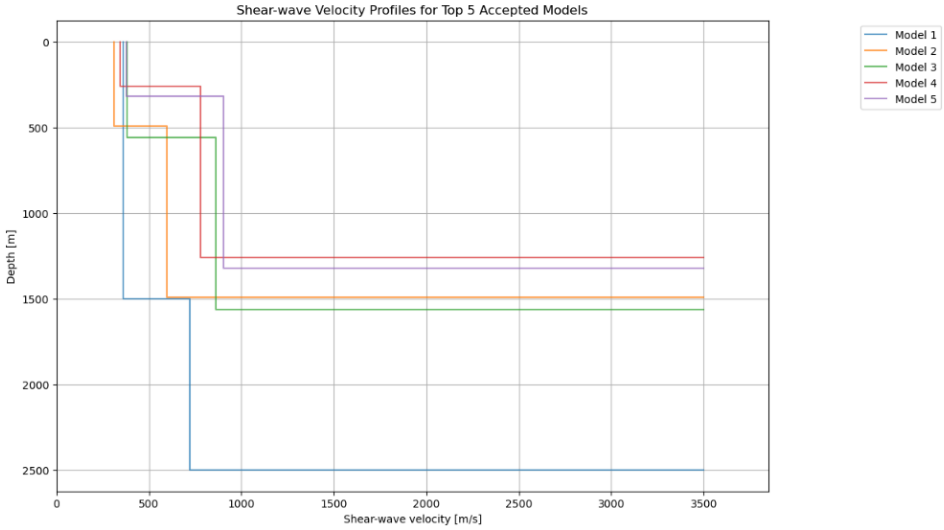

Figure 4.33. Top 5 Accepted Model for Station 3407 with Input from Synthetic Waveforms Generated at the Surface

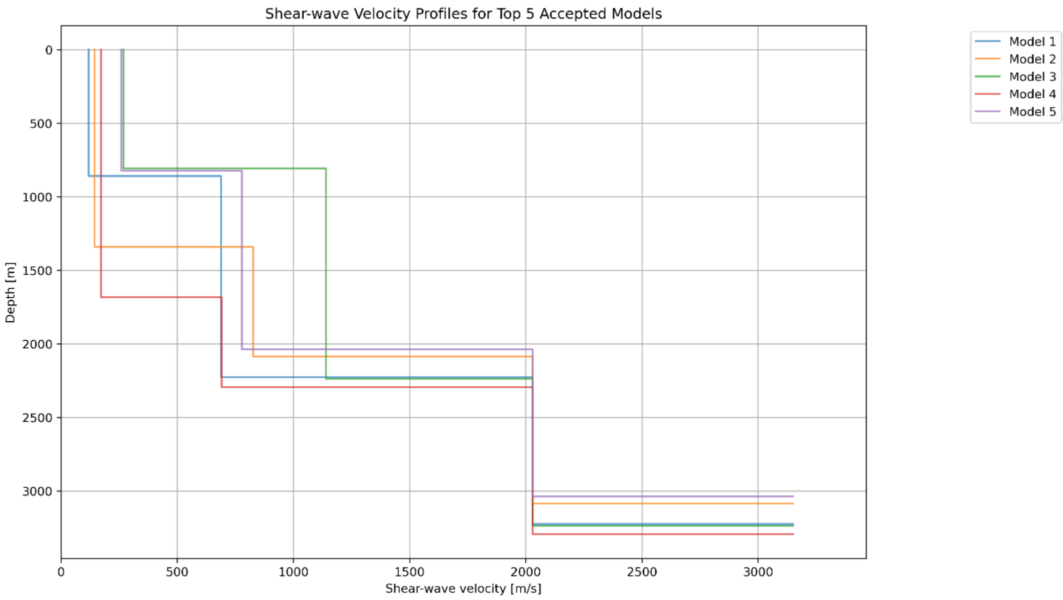

Figure 4.34. Top 5 Accepted Model for Station 3407 with Input from Synthetic Waveforms Generated at the Depth of 2 km

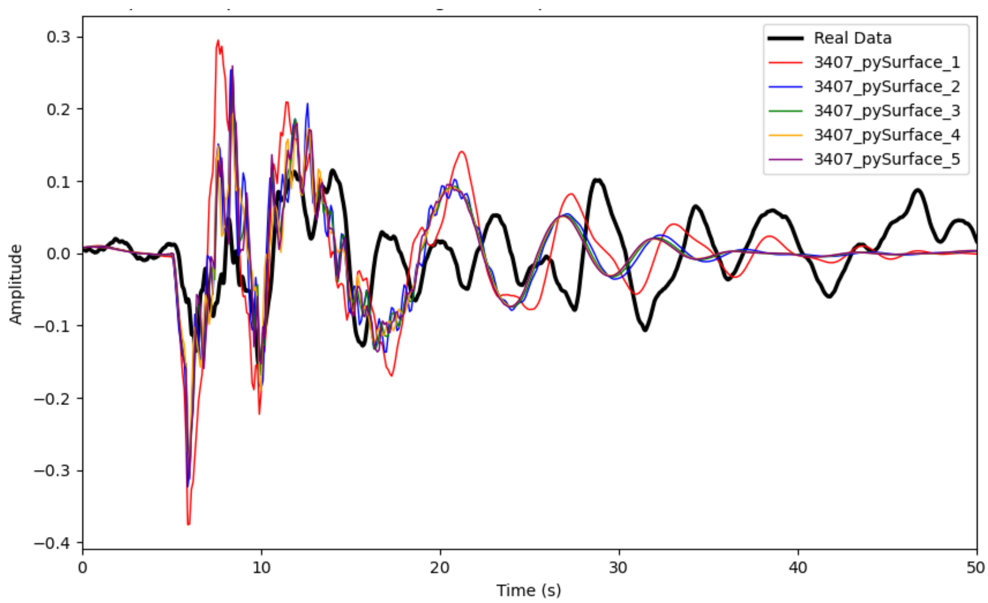

Figure 4.35. Top 5 Accepted Velocity Models Synthetic Waveforms Generated at the Surface vs Real Tangential Displacement Data for Station 3407

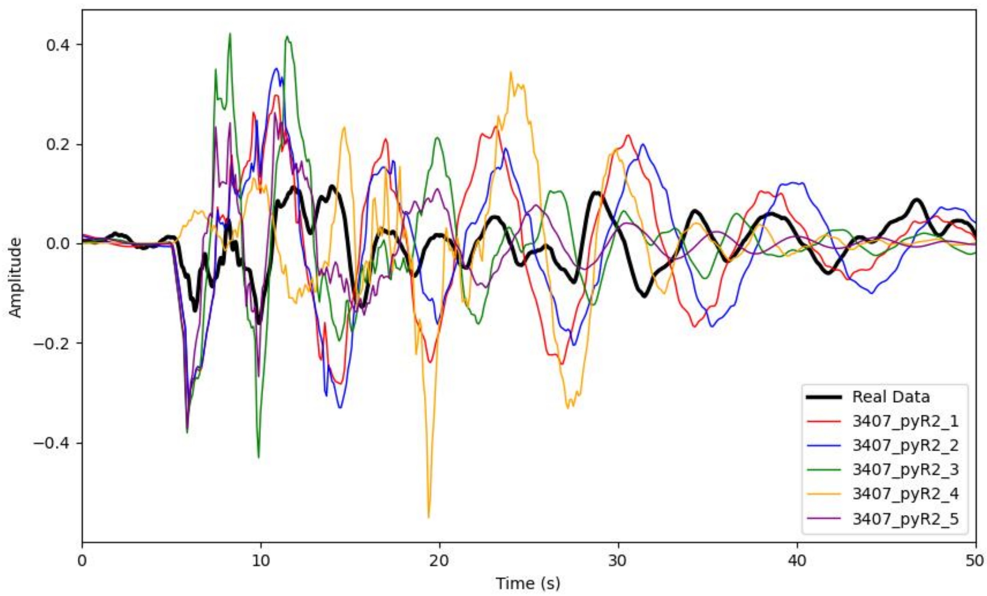

Figure 4.36. Top 5 Accepted Velocity Models Synthetic Waveforms Generated at the Depth of -2km vs Real Tangential Displacement Data for Station 3407

Figure 4.37 shows amplification range at the frequency domain, the amplified synthetic data over real data and the synthetic data which was generated with crustal structure model over real data, with Input from Synthetic Waveforms Generated at the Surface (left) and at the depth of -2 km (right) correspondingly.

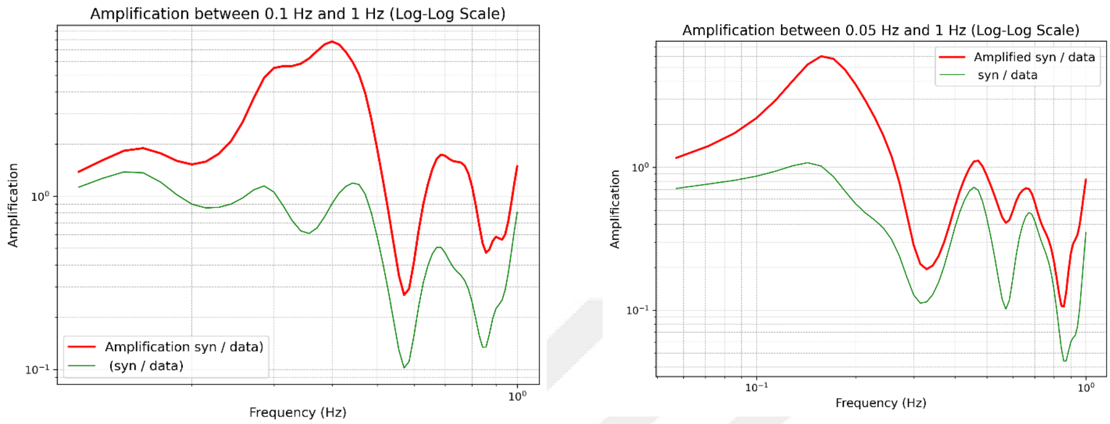

Figure 4.37. Amplification Range at the Frequency Domain for station 3407

4.3. Site Amplification Optimization and Site Specific Shallow Model Optimization for Non Amplified Stations

Although amplification is observed at these stations 3405,3406,3408,3411, a good fit could not be achieved with all the top five velocity models, since these are relatively hard rock sites. Normally, in soft sediment sites, one would expect to observe the amplification because of stronger wave energy trapping and resonance effects due to lower shear wave velocities. However, such amplification hardly ever appears in hard rock sites due to much higher values of Vs and lower impedance contrast. The inability to model such amplification thus does not point at data processing issues but underlines natural limitations of velocity models in capturing the amplification at hard rock sites where, generally, amplification is small. Results will be shown as the amplification observed with Input from Synthetic Waveforms Generated at the Surface for stations exhibiting amplification will be presented. Subsequently, the results for these stations at a depth of 2 km will be displayed. In both cases, synthetic waveforms will be sequentially compared with time-domain waveforms obtained through convolution with the transfer function of the optimal two layers.

4.3.1. Result of Station 3405

In the case of station 3405, the first layer's thickness was chosen between 300 meters and 500 meters with Vs values from 100 m/s to 400 m/s, while the second layer thickness was chosen between 600 meters and 1000 meters with Vs ranging from 200 m/s to 600 m/s. The damping factor has been considered within the range 1-5 for the first layer and between 0.1 and 1 for the second layer. These values have been selected for this area in view of their relatively soft sediments, the range of Vs values was derived based on reports from AFAD stations. Figure 4.38 shows the calculation of the amplification factor at the surface, where the synthetic seismogram from the crustal model has been taken as an input. In the time history plot, the amplitudes of the output signal are much larger with respect to the input signal, especially between approximately 10 to 25 seconds, showing very strong site response. It is further confirmed by the amplification spectrum, which shows strong amplification in the frequency range between 0.5 Hz and 10 Hz, with distinct peaks within the frequency window of 1 Hz to 5 Hz. Thus, it indicates that the site amplifies seismic waves within this frequency range. The phase shift plot is on a decreasing trend, which means that higher frequencies are experiencing greater phase delays that can be attributed to the frequency-dependent wave propagation effects. Also, Fourier amplitude spectra showing the constant higher output motion amplitudes than the input motion amplitudes within the same frequency window confirm that amplification is taking place. It can be observed that for frequencies lower than 0.5 Hz, the shapes of the input and output spectra are similar while exhibiting a very small amplification. Generally, this analysis points out that seismic energy has been most amplified in this station within a frequency range of 0.5-10 Hz, particularly between 1 Hz and 5 Hz, most probably due to the local site and subsurface effect.

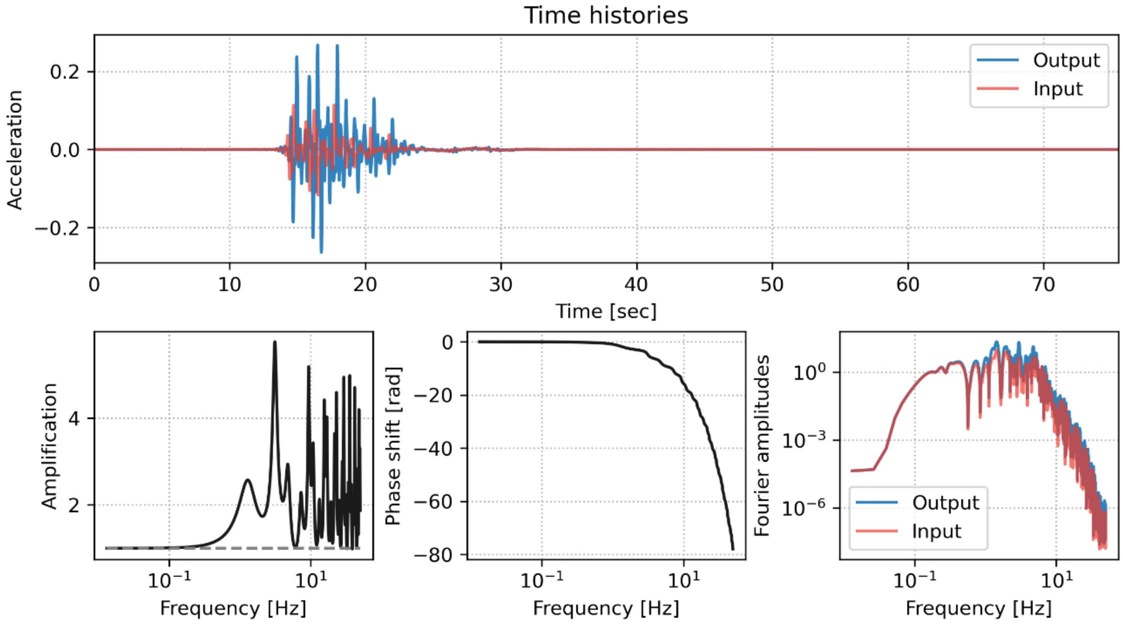

Figure 4.38. Amplification Factor and Fourier Amplitude Comparison of Station 3405 with Input from Synthetic Waveforms Generated at the Surface

Figure 4.39 presents the amplification effects that were observed at a depth of 2 km, for which the input signal in red is taken as the synthetic seismogram produced from the crustal model, and the output signal in blue is its amplified version after wave propagation. A strong increase in amplitude of the output motion within 15 to 25 seconds is visible in the time history plot, which indicates strong site effects. The result is an increase in the maximum amplification within the frequency spectrum between 0.1 Hz up to 3 Hz, with peaks over a factor of 8 that may show resonant effects caused by impedance contrast in the deeper structure. The phase shift plot shows considerable wave dispersion, particularly at higher frequencies, while the Fourier amplitude spectra show that the output contains the spectral characteristics of the input but with increased energy, especially within the 0.1 Hz to 10 Hz range. These results suggest that the deeper geological structure significantly amplifies seismic waves, especially in the lower frequencies, by changing both their amplitude and phase characteristics due to resonance and propagation of waves.

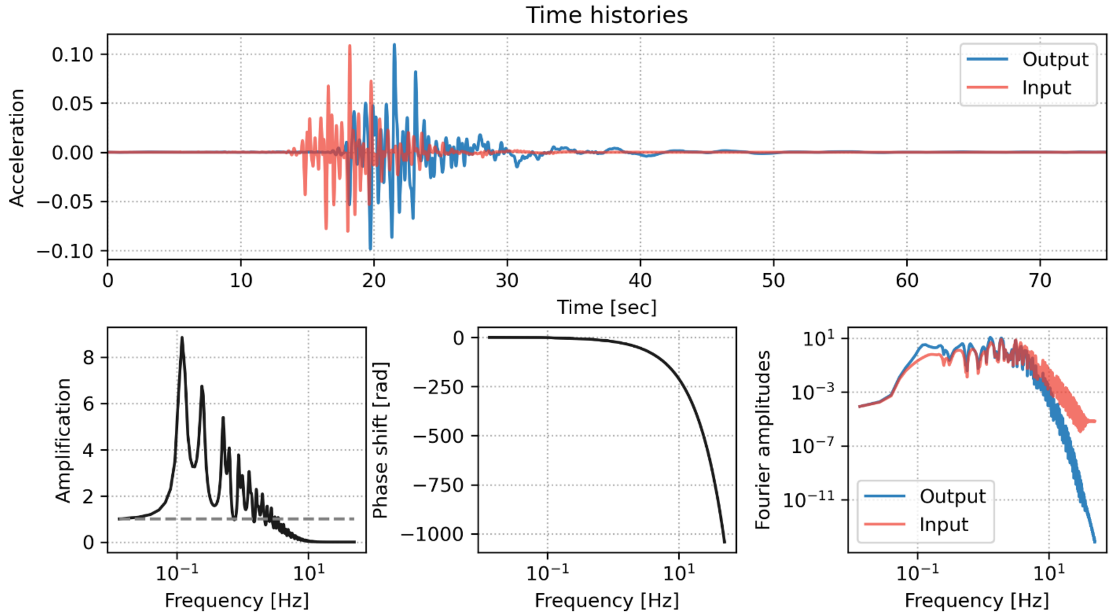

Figure 4.39. Amplification Factor and Fourier Amplitude Comparison of Station 3405 with Input from Synthetic Waveforms Generated at the Depth of 2 km

Figure 4.40 and Figure 4.41 illustrate the depth and Vs velocity of the five generated velocity models at the levels of the surface and -2 km, respectively. Similarly, Figure 4.42 and Figure 4.43 present the comparison between the synthetic waveforms generated using these velocity models and the real data, in the same order.

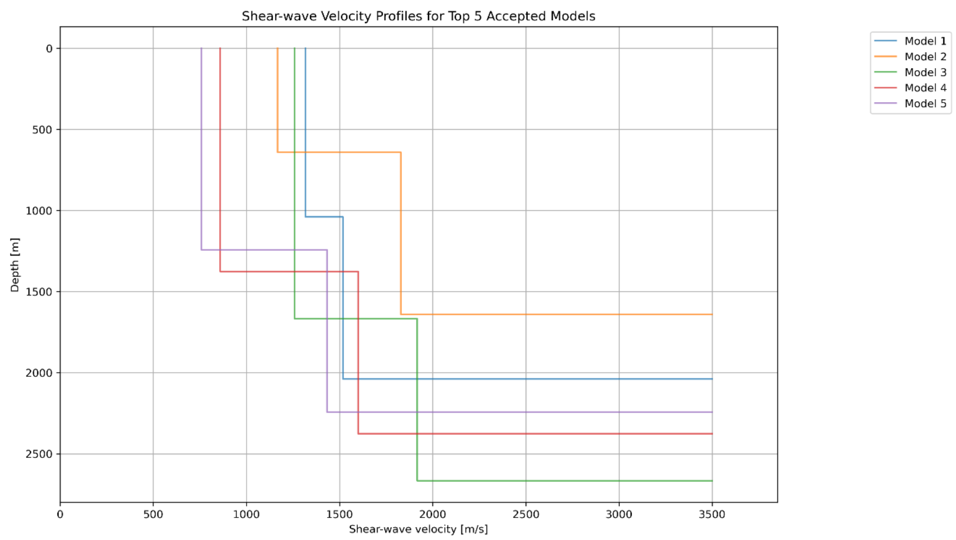

Figure 4.40. Top 5 Accepted Model for Station 3405 with Input from Synthetic Waveforms Generated at the Surface

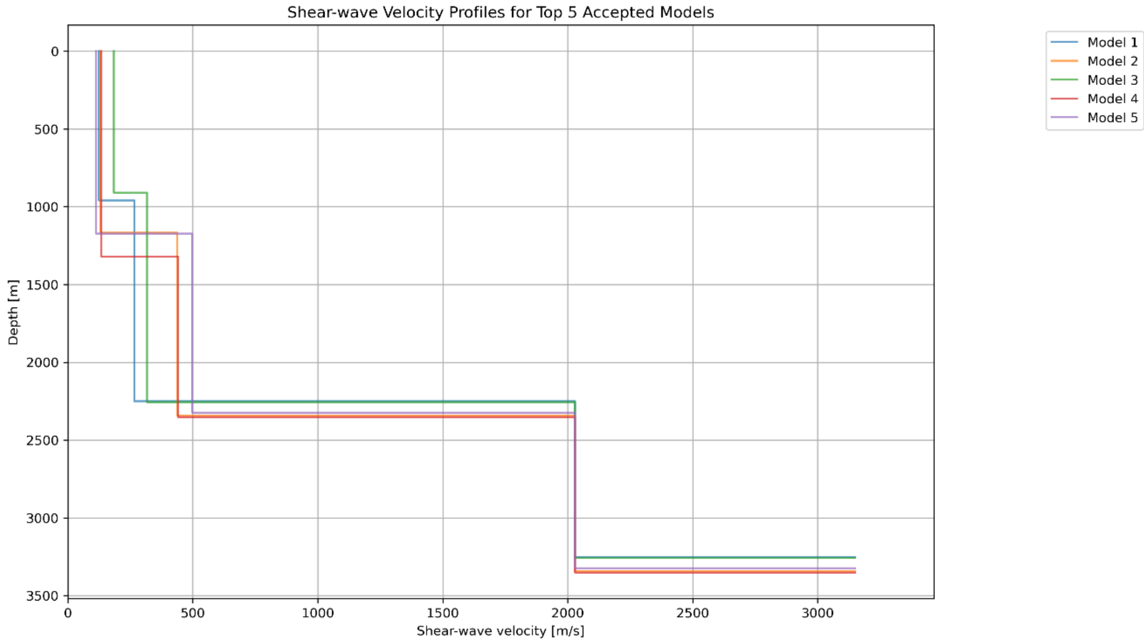

Figure 4.41. Top 5 Accepted Model for Station 3405 with Input from Synthetic Waveforms Generated at the Depth of 2 km

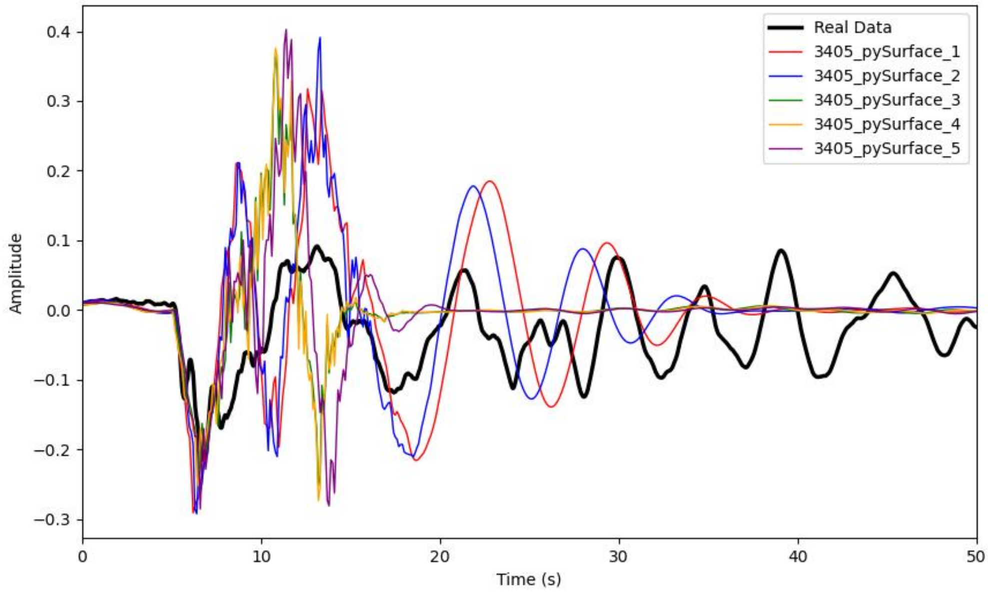

Figure 4.42. Top 5 Accepted Velocity Models Synthetic Waveforms Generated at the Surface vs Real Tangential Displacement Data for Station 3405

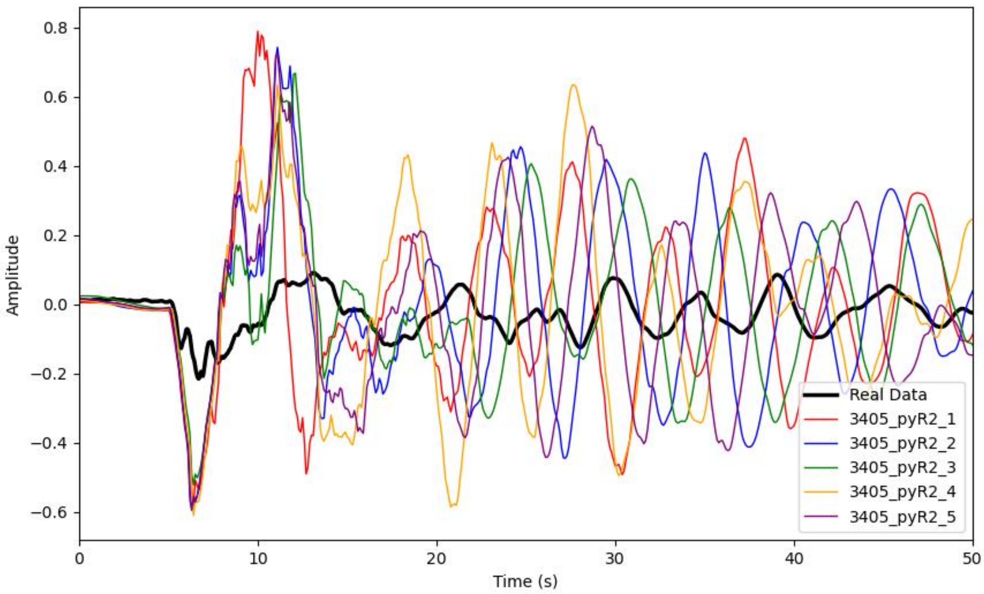

Figure 4.43. Top 5 Accepted Velocity Models Synthetic Waveforms Generated at the Depth of -2km vs Real Tangential Displacement Data for Station 3405

Figure 4.44 shows amplification range at the frequency domain, the amplified synthetic data over real data and the synthetic data which was generated with crustal structure model over real data, with Input from Synthetic Waveforms Generated at the Surface (left) and at the depth of -2 km (right) correspondingly.

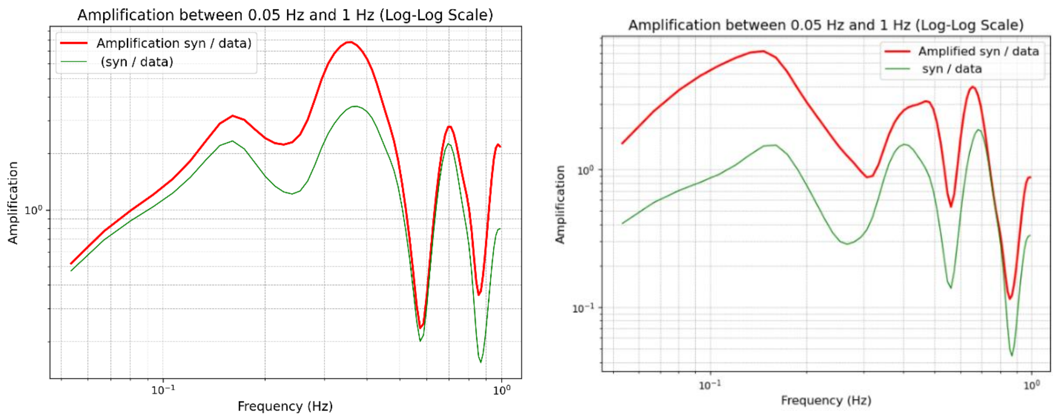

Figure 4.44. Amplification Range at the Frequency Domain for station 3405

4.3.2. Result of Station 3406

In the case of station 3406, the first layer's thickness was chosen between 100 meters and 500 meters with Vs values from 300 m/s to 800 m/s, while the second layer thickness was chosen between 100 meters and 1000 meters with Vs ranging from 400 m/s to 1000 m/s. The damping factor has been considered within the range 1-5 for the first layer and between 1 and 5 for the second layer. These values have been selected for this area in view of their relatively soft sediments, the range of Vs values was derived based on reports from AFAD stations. Figure 4.45 shows the calculation of the amplification factor at the surface, where the synthetic seismogram from the crustal model has been taken as an input. The time history plot displays input (red) and output (blue) signals: the latter is significantly amplified, with main amplifications falling in between 15 to 30 s due to the wave propagation effects through the modeled velocity structure. The bottom-left panel shows that the amplification spectrum clearly increases within the frequency range of 0.2 Hz to 3 Hz with peak values over three times the input motion, suggesting that the crustal model enhances seismic energy within this frequency band due to impedance contrasts and resonance effects. The bottom middle panel represents the phase shift plot, indicating a decreasing trend, which signifies that with increasing frequency, the output signal becomes progressively delayed with respect to the input, and thus the effects of wave dispersion are highlighted. Fourier amplitude spectra, represented by the bottom right panel, further confirm that throughout most frequencies, but especially within the low-to-mid frequency range of 0.2 Hz to 10 Hz, the output motion amplitudes are higher in agreement with the observed amplification trends. The most important implication of these results is that the crustal model induces significant amplification effects, mostly at lower frequencies, where wave resonance and site-specific characteristics prevail in seismic wave propagation.

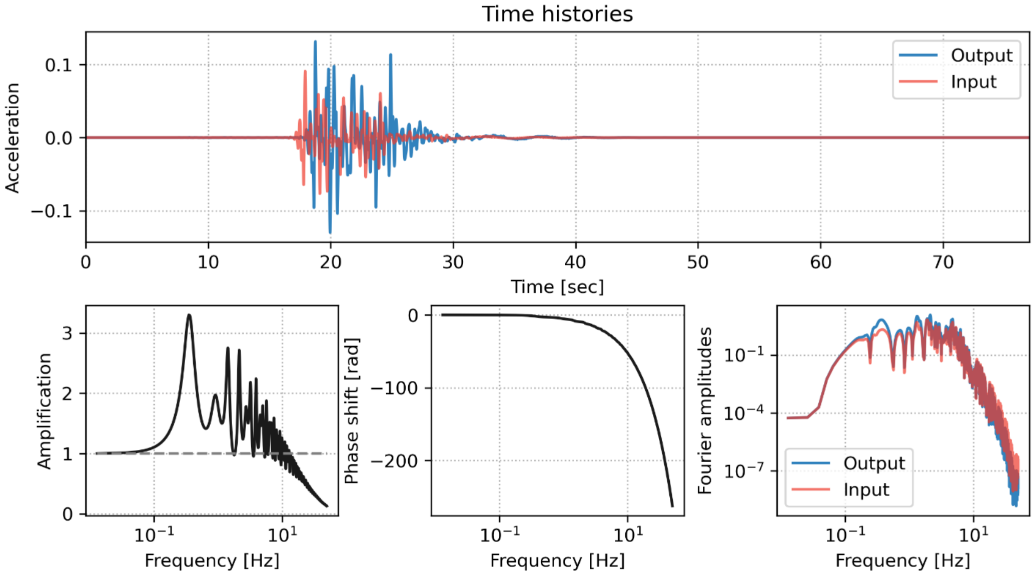

Figure 4.45. Amplification Factor and Fourier Amplitude Comparison of Station 3406 with Input from Synthetic Waveforms Generated at the Surface

Figure 4.46 shows the amplification factor Generated using, as input, the synthetic seismogram generated from the crustal model. Note that in the time history plot, in the top panel, the input signal (red) and the output (blue) present a clearly visible amplification effect. In fact, between 15 to 25 s, the amplitude of the output signal is higher than that of the input. The most amplification, since the resultant of the bottom-left panel of the amplification spectrum is for frequencies ranging between 0.1 and 1 Hz, reaching a peak factor of amplification greater than 2. This already says everything, that this crustal model enhances the ground motion mainly due to impedance contrasts and resonance effects at the low-frequency range. The phase shift plot given by the bottom middle panel reflects a progressive decrease, greater delays for higher frequencies, representative of wave dispersion effects in the model. Fourier amplitude spectra bottom right panel show that the amplitude of output motion is higher within the frequency range 0.1 to 10 Hz as compared with the input and thereby reinforces amplification trends discussed previously. These results indicate that this crustal model introduces huge amplification effects, especially in those lower frequencies where site response characteristics play a major role in modifying seismic wave propagation.

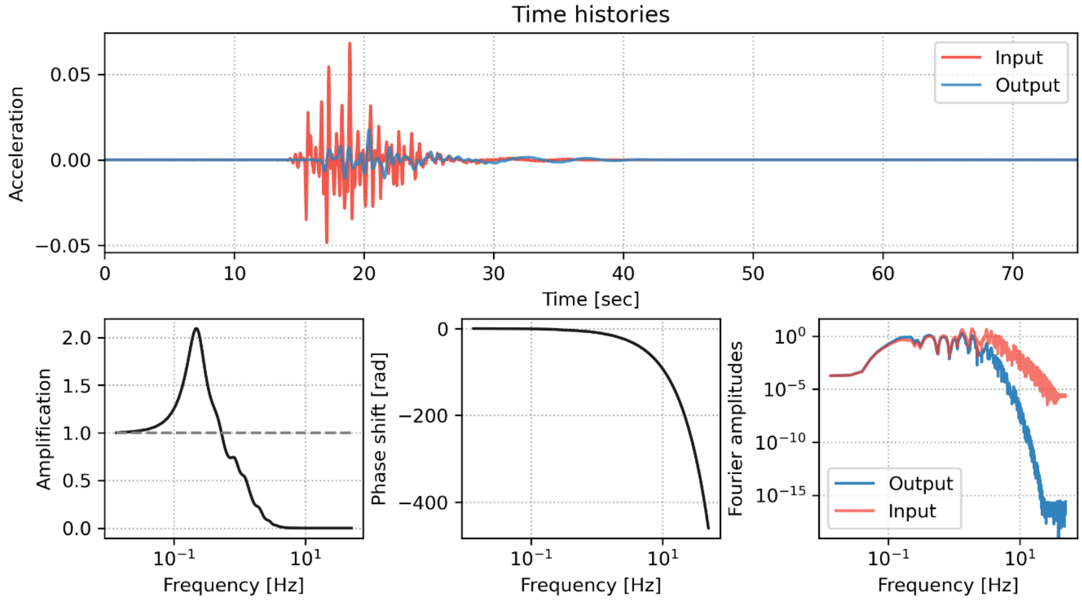

Figure 4.46. Amplification Factor and Fourier Amplitude Comparison of Station 3406 with Input from Synthetic Waveforms Generated at the Depth of 2 km

Figure 4.47 and Figure 4.48 illustrate the depth and Vs velocity of the five generated velocity models with Input from Synthetic Waveforms Generated at the Surface and depth of -2 km, respectively. Similarly, Figure 4.49 and Figure 4.50 present the comparison between the synthetic waveforms generated using these velocity models and the real data, in the same order.

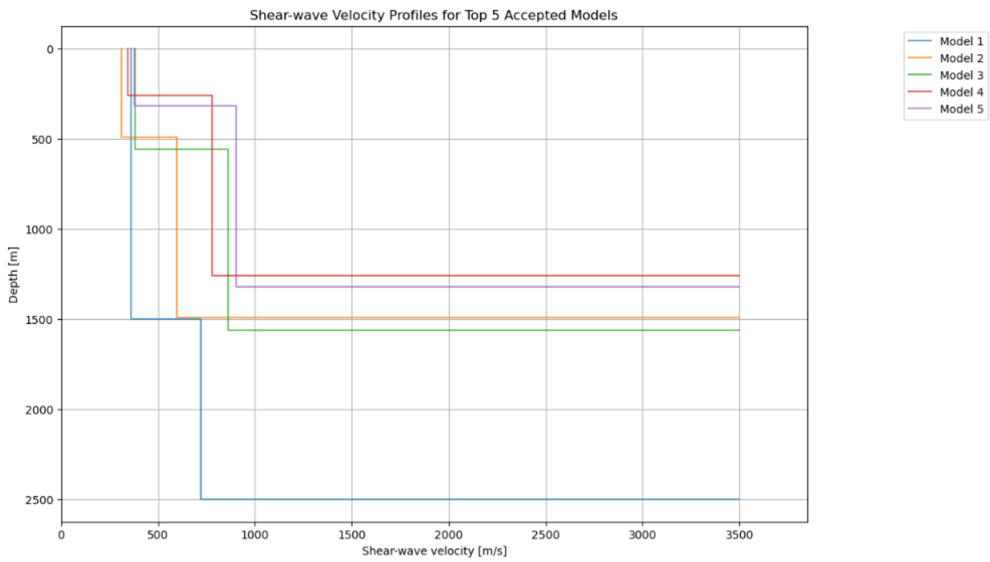

Figure 4.47. Top 5 Accepted Model for Station 3406 with Input from Synthetic Waveforms Generated at the Surface

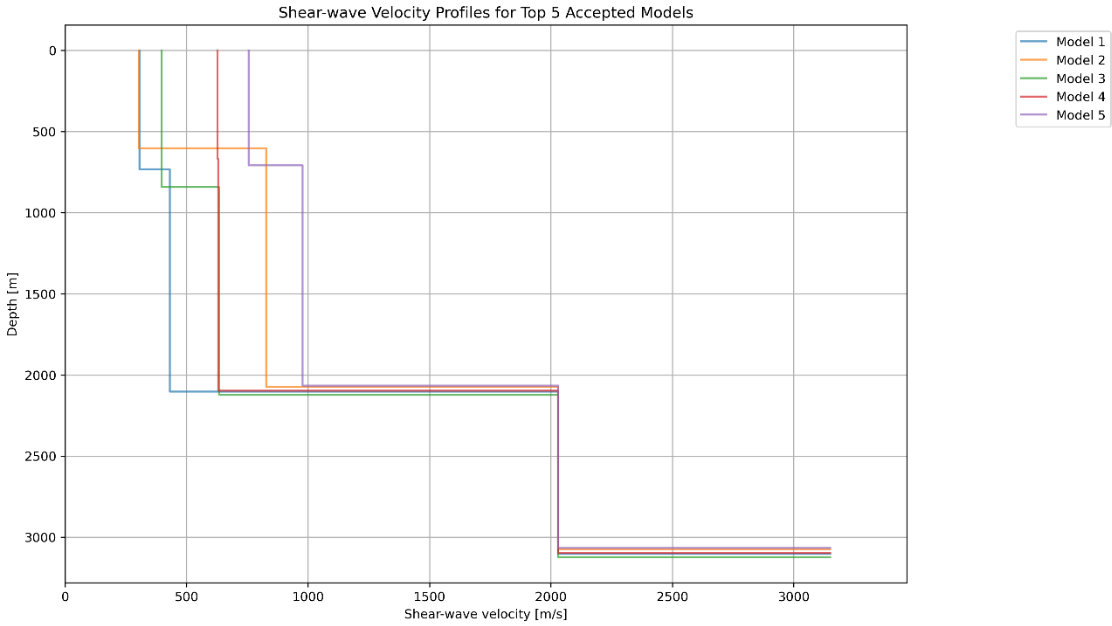

Figure 4.48. Top 5 Accepted Model for Station 3406 with Input from Synthetic Waveforms Generated at the Depth of 2 km

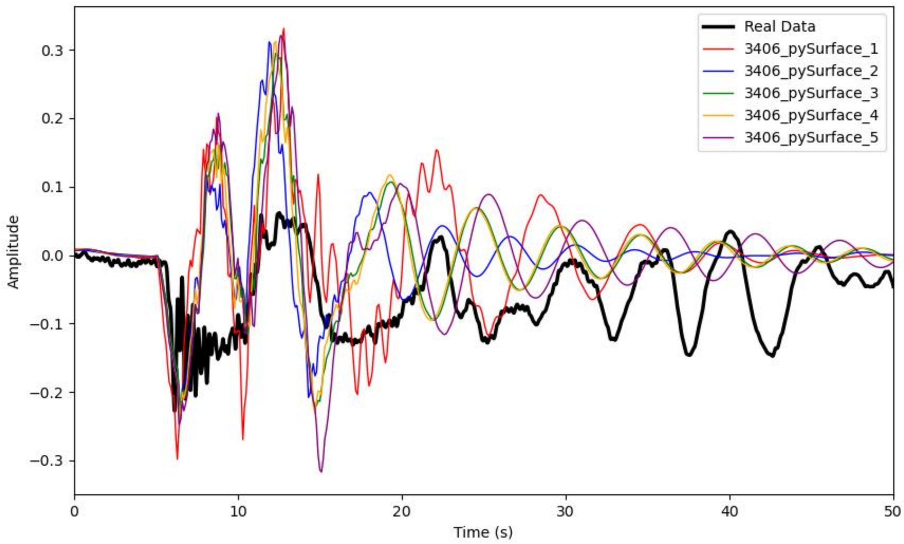

Figure 4.49. Top 5 Accepted Velocity Models Synthetic Waveforms Generated at the Surface vs Real Tangential Displacement Data for Station 3405

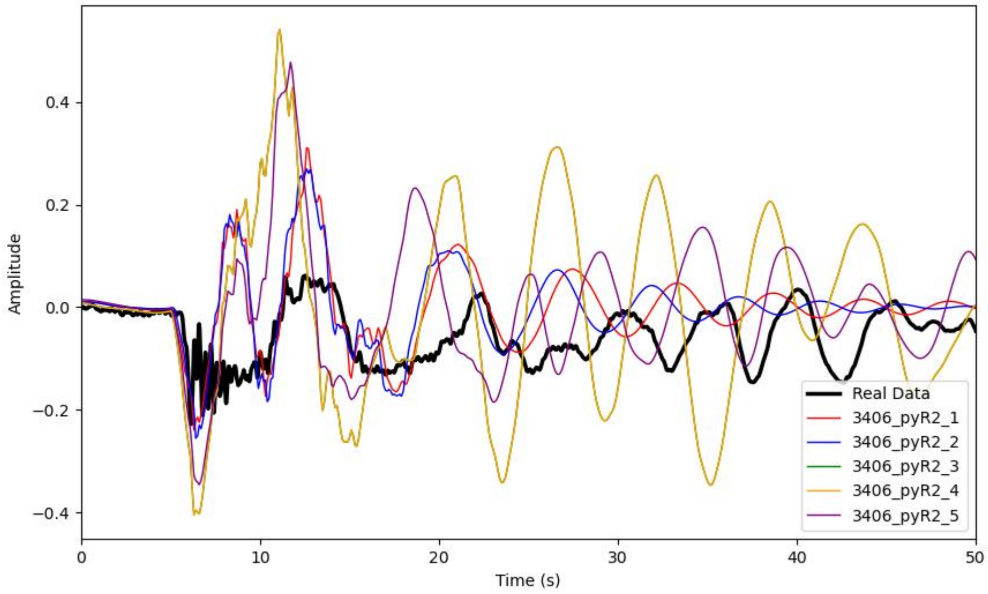

Figure 4.50. Top 5 Accepted Velocity Models Synthetic Waveforms Generated at the Depth of -2km vs Real Tangential Displacement Data for Station 3406

Figure 4.51 shows amplification range at the frequency domain, the amplified synthetic data over real data and the synthetic data which was generated with crustal structure model over real data, with Input from Synthetic Waveforms Generated at the Surface (left) and at the depth of -2 km (right) correspondingly.

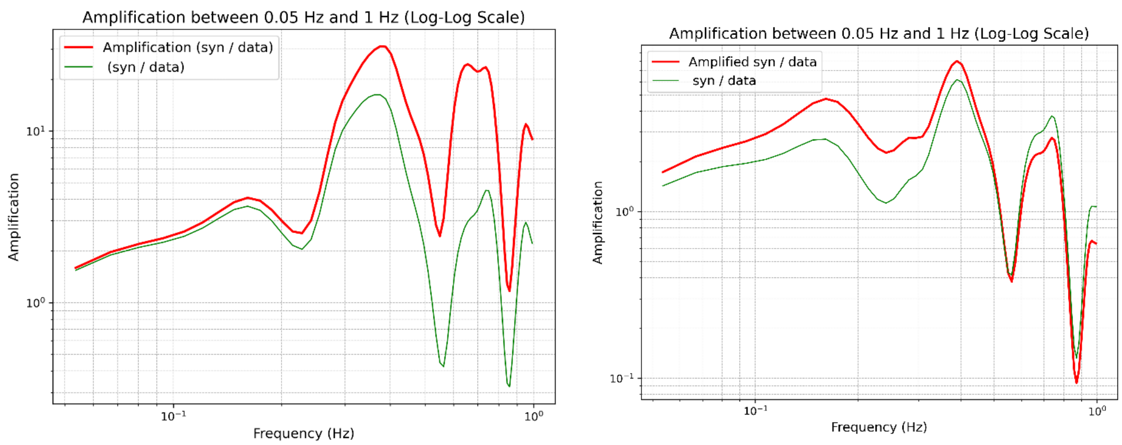

Figure 4.51. Amplification Range at the Frequency Domain for station 3406

4.3.3. Result of Station 3408

In the case, station 3405, the first layer's thickness was chosen in between 100 meters and 300 meters with Vs values from 100 m/s to 300 m/s, while the second layer thickness was chosen in between 100 meters and 1500 meters with Vs ranging from 200 m/s to 1500 m/s. The damping factor has been considered within the range 1-5 for the first layer and between 0.1 and 1 for the second layer. These values have been selected for this area in view of their relatively soft sediments, the range of Vs values was derived based on reports from AFAD stations. Figure 4.52 shows the calculation of the amplification factor with Input from Synthetic Waveforms Generated at the Surface, where the synthetic seismogram from the crustal model has been taken as an input. From this time history, the input signals are in red color and the output signals. It is clear that there is a strong effect of amplification above all between 15 to 30 seconds where the amplitudes related to the outputs are higher with respect to the inputs, demonstrating strong site responses. The most marked amplification lies within the range from 0.1 to 5 Hz, as obtained from the amplification spectrum at the bottom left panel, having peak values well over 10 times the input motion. Hence, it could be assumed from this that the seismic energy will be enhanced due to impedance contrast and resonance effect within this range by the crustal model. The phase shift plot, bottom middle panel, reflects the significant reduction on account of wave dispersion effects mainly at the higher frequencies. Fourier amplitude spectra of the same-bottom right panel-essentially substantiate that the amplitude components of output motion are well above that of the input, predominantly between 0.1 Hz and 10 Hz, further confirming the trend above. These results therefore indicate that the crustal model contributes significant amplification, particularly at lower frequencies where site response characteristics are very important in modifying seismic wave propagation. Figure 4.53 shows a synthetic seismogram computation using the crustal model for given input to give the calculation of amplification factor. Time History: The plot above compares between the input red and output blue signals of this computation. Most obvious is the fact that it has been drastically amplified, since the site responses are very strongly developed in a window of about 10 to 20 sec. The bottom left panel of the amplification spectrum indicates that the principal amplification lies in the frequency range between 0.1 and 5 Hz, including peak values larger than 10 times the input motion. This may suggest that seismic energy has been developed in the given frequency range due to impedance contrasts and resonance effects in the crustal model. The phase shift plot indeed has a steep, generally decreasing trend that describes strong wave dispersion at especially higher frequencies. These are indeed confirmed by the Fourier amplitude spectra shown in the bottom right panel; for the most part, especially within the range 0.1 Hz to 10 Hz, the output motion has larger amplitude than the input, hence reinforcing the pattern of amplification observed. Results obtained from the above studies indicate that the crustal model significantly amplifies seismic waves, especially at low frequencies where subsurface structure and resonance effects dominate to modify wave propagation.

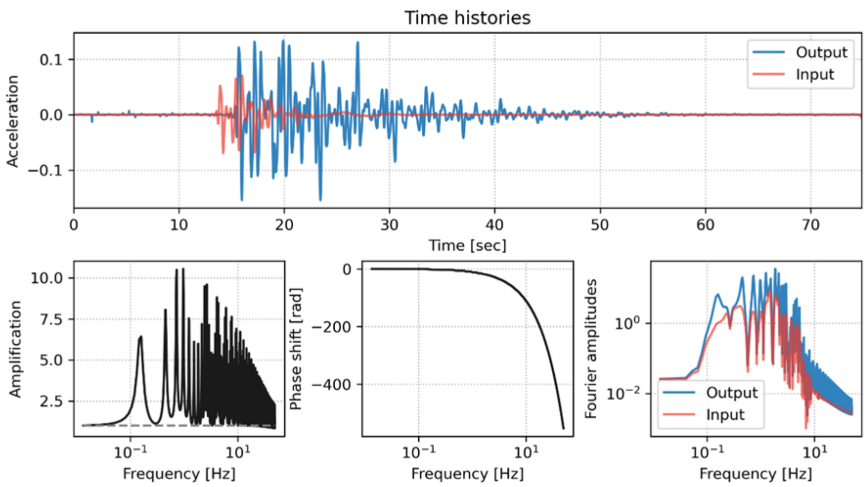

Figure 4.52. Amplification Factor and Fourier Amplitude Comparison of Station 3408 with Input from Synthetic Waveforms Generated at the Surface

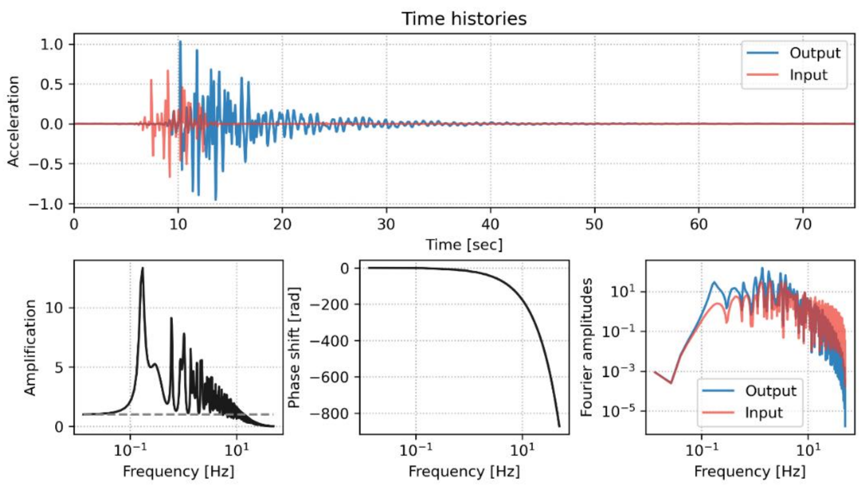

Figure 4.53. Amplification Factor and Fourier Amplitude Comparison of Station 3408 with Input from Synthetic Waveforms Generated at the Depth of 2 km

Figure 4.54 and Figure 4.55 illustrate the depth and Vs velocity of the five generated velocity models at the levels of the surface and -2 km, respectively. Similarly, Figure 4.56 and Figure 4.57 present the comparison between the synthetic waveforms generated using these velocity models and the real data, in the same order. Figure 4.58 shows amplification range at the frequency domain, the amplified synthetic data over real data and the synthetic data which was generated with crustal structure model over real data, with Input from Synthetic Waveforms Generated at the Surface (left) and at the Depth of -2 km (right) correspondingly.

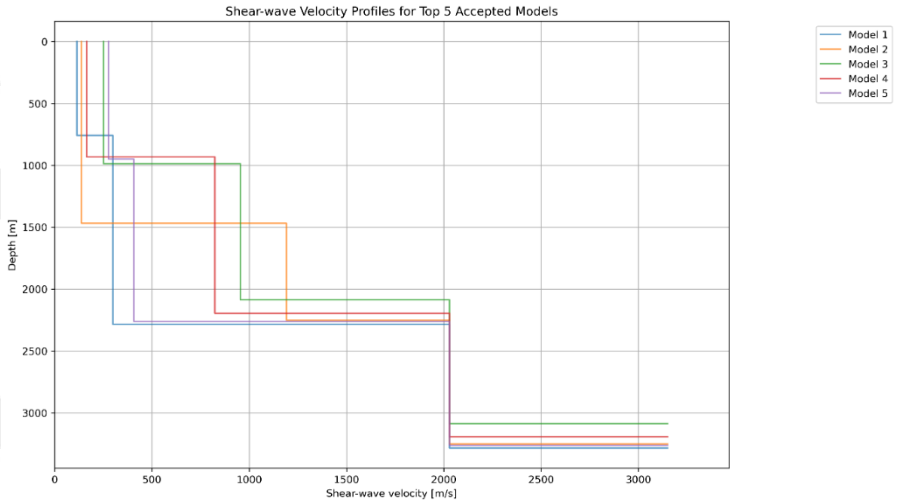

Figure 4.54. Top 5 Accepted Model for Station 3408 with Input from Synthetic Waveforms Generated at the Surface

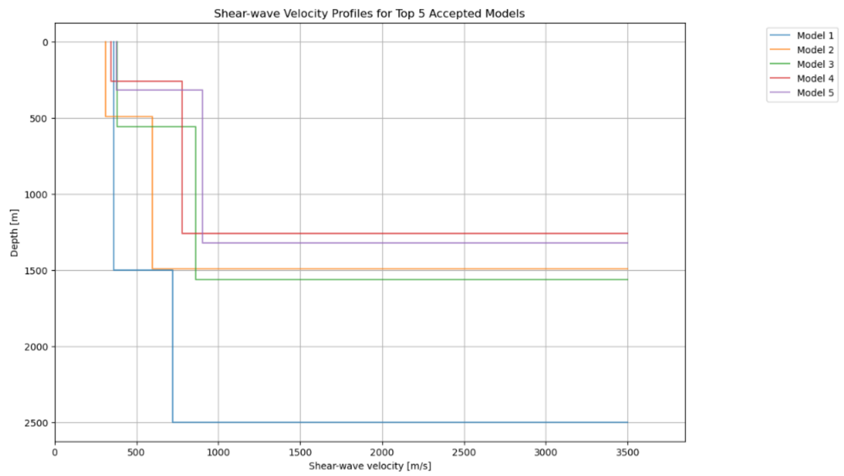

Figure 4.55. Top 5 Accepted Model for Station 3408 with Input from Synthetic Waveforms Generated at the Depth of 2 km

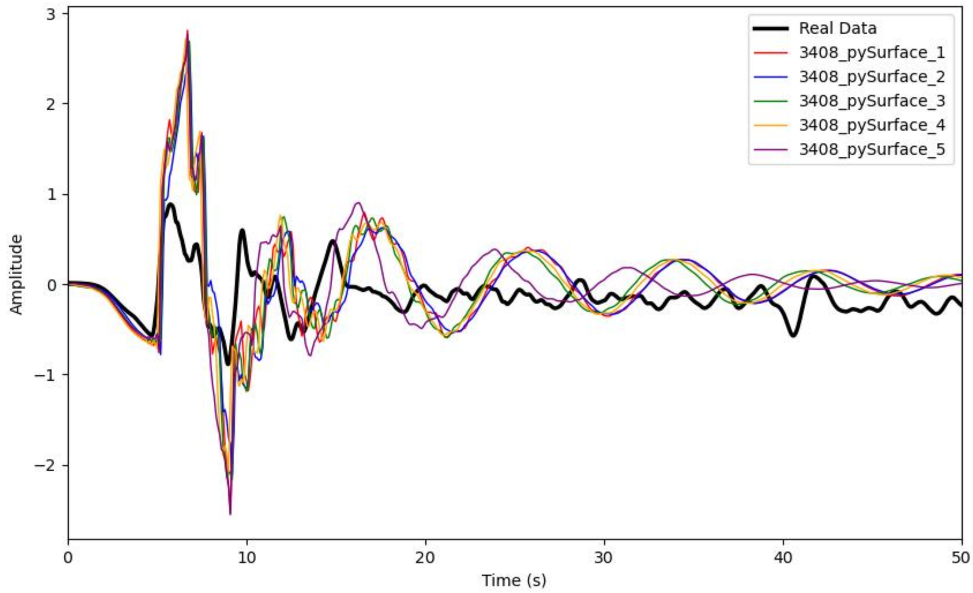

Figure 4.56. Top 5 Accepted Velocity Models Synthetic Waveforms Generated at the Surface vs Real Tangential Displacement Data for Station 3408

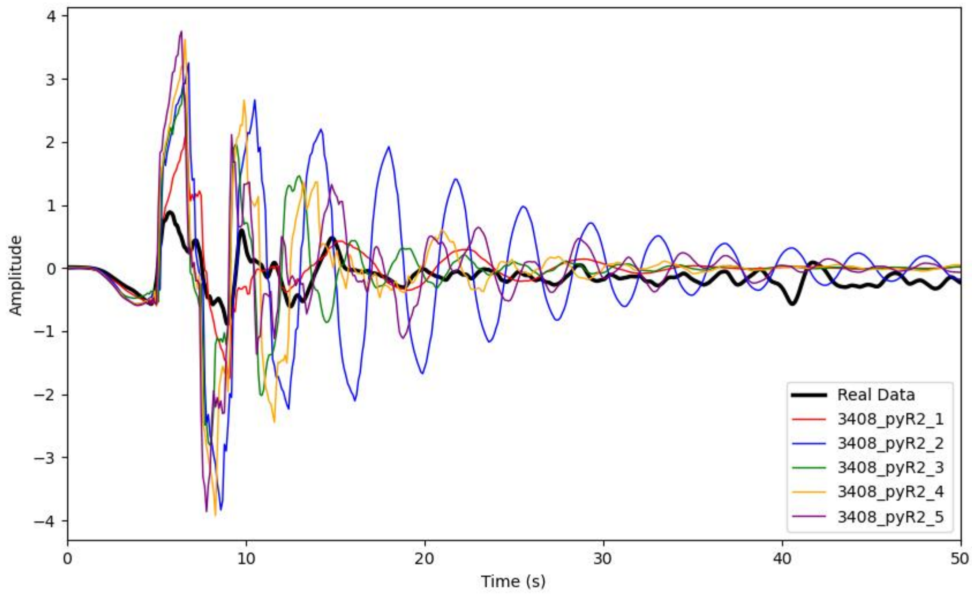

Figure 4.57. Top 5 Accepted Velocity Models Synthetic Waveforms Generated at the Depth of -2km vs Real Tangential Displacement Data for Station 3408

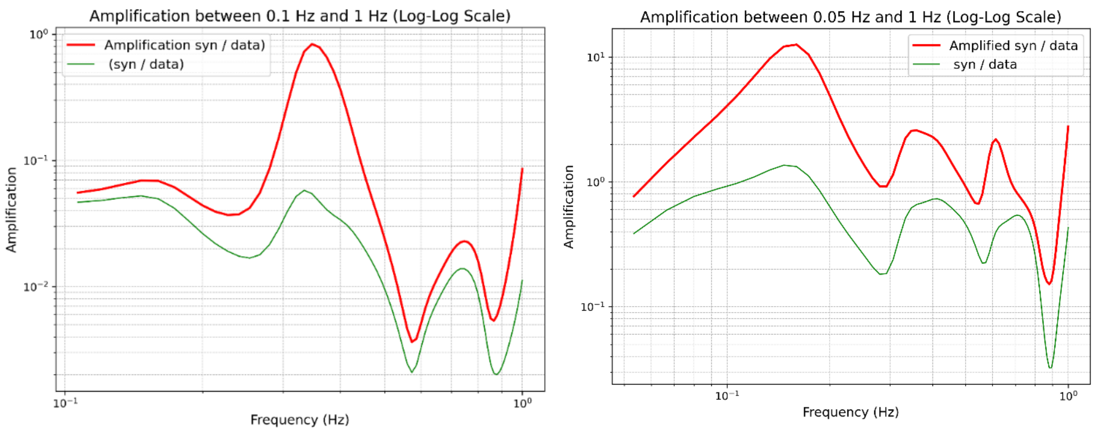

Figure 4.58. Amplification Range at the Frequency Domain for station 3408

4.3.4. Result of Station 3417

In the case, station 3417, the first layer's thickness was chosen in between 400 meters and 600 meters with Vs values from 600 m/s to 1000 m/s, while the second layer thickness was chosen in between 800 meters and 1500 meters with Vs ranging from 800 m/s to 2000 m/s. The damping factor has been considered within the range 1-3 for the first layer and between 1 and 3 for the second layer. These values have been selected for this area in view of their relatively soft sediments, the range of Vs values was derived based on reports from AFAD stations. Figure 4.59 shows the calculation of the amplification factor with Input from Synthetic Waveforms Generated at the Surface, where the synthetic seismogram from the crustal model has been taken as an input. The acceleration time history given in top panel: input in red, output in blue. From this output waveform, one can see that it has larger amplitudes w.r.t the input and such an effect may be attributed to the crust structure. The bottom-left panel shows the frequency-dependent amplification factor and reveals strong amplification at the lower frequencies below 1 Hz, with resonance peaks extending well into higher frequencies. The middle panel displays the phase shift that decreases progressively with increasing frequency and evidences wave propagation as dispersive in this crustal model. The bottom-right panel: Fourier amplitude spectra of input and output signals. A blue output spectrum shows higher amplitudes for the same frequencies compared to the input-red-skewed above in the time domain. From these results, it is evident that the crustal velocity model promotes frequency-dependent amplification of waves and mainly those with a long period. The peaks of resonance observed show consistency with the site response characteristics of the crustal structure.

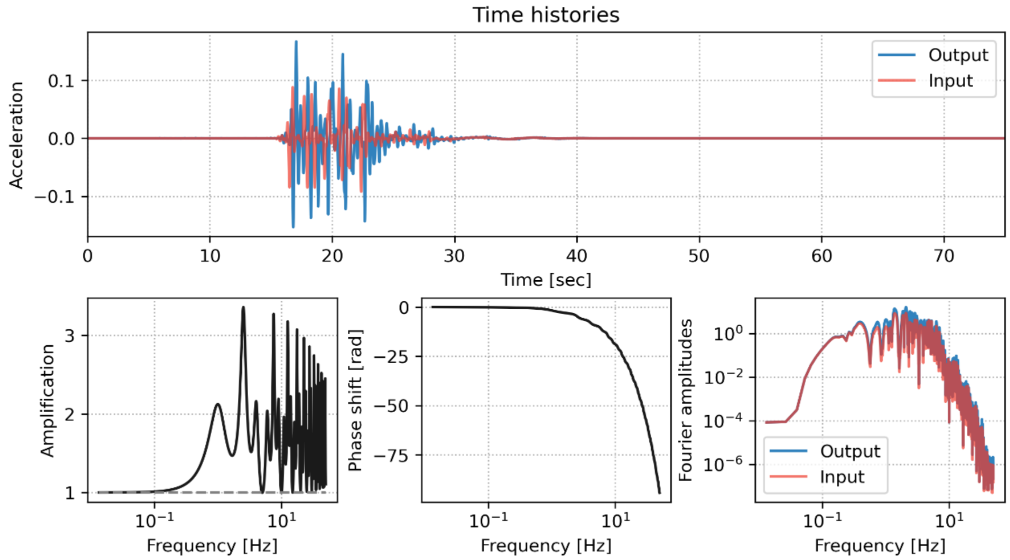

Figure 4.59. Amplification Factor and Fourier Amplitude Comparison of Station 3417 with Input from Synthetic Waveforms Generated at the Surface

Figure 4.60 shows the calculation of an amplification ratio by using a synthetic seismogram along with crustal velocity model. Time history of acceleration is shown in top panel. Input motion is given in red whereas output motion is shown in blue color. One can easily see that amplitude of output has been increased (amplification effect, in particular during the peak shaking). The lower left panel shows the frequency-dependent amplification factor, which has several important peaks at low frequencies due to resonant effects from subsurface layering. The central panel plots the phase shift between input and output signals, representing the wave propagation modification induced by the crustal model. The lower right panel shows the Fourier amplitude spectra of input and output motions. This therefore means that at the frequency bands, most especially within the low-mid frequency range, an easily noticed effect of amplification is viewed. This analysis justifies the inference that seismic wave propagation depends on a crustal model in such a way that amplitude and phases change. Since this indicates the presence of amplification peaks associated with ground motion, there should be something related to specific frequency site effects in resonance or due to wave trapping.

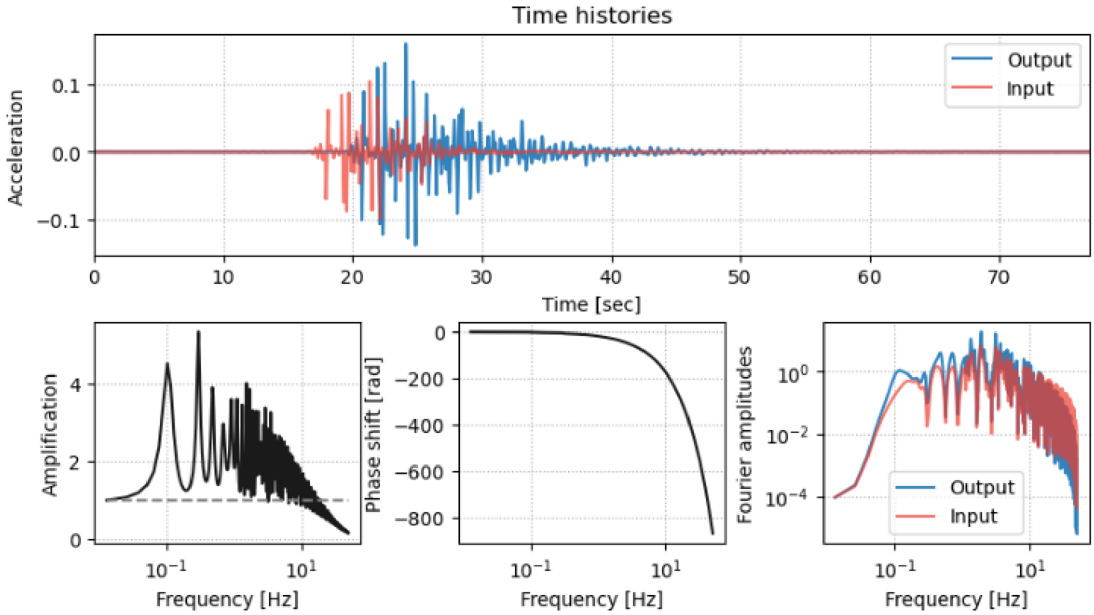

Figure 4.60. Amplification Factor and Fourier Amplitude Comparison of Station 3417 with Input from Synthetic Waveforms Generated at the Depth of 2 km

Figure 4.61 and Figure 4.62 illustrate the depth and Vs velocity of the five generated velocity models at levels of the surface and -2 km, respectively. Similarly, Figure 4.63 and Figure 4.64 present the comparison between the synthetic waveforms generated using these velocity models and the real data, in the same order. Figure 4.65 shows amplification range at the frequency domain, the amplified synthetic data over real data and the synthetic data which was generated with crustal structure model over real data, with Input from Synthetic Waveforms Generated at the Surface (left) and at the bottom -2 km (right) correspondingly.

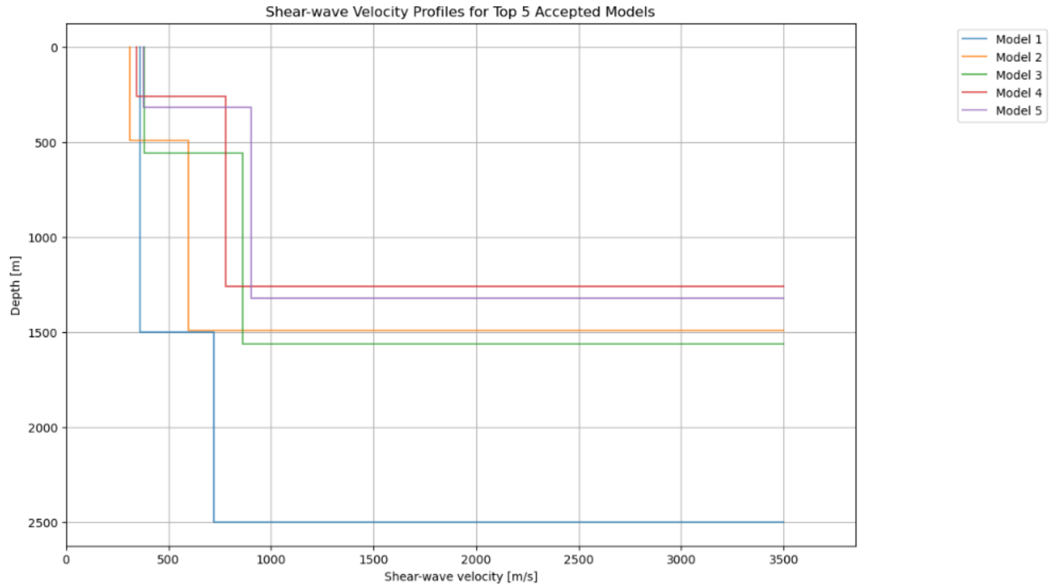

Figure 4.61. Top 5 Accepted Model for Station 3417 with Input from Synthetic Waveforms Generated at the Surface

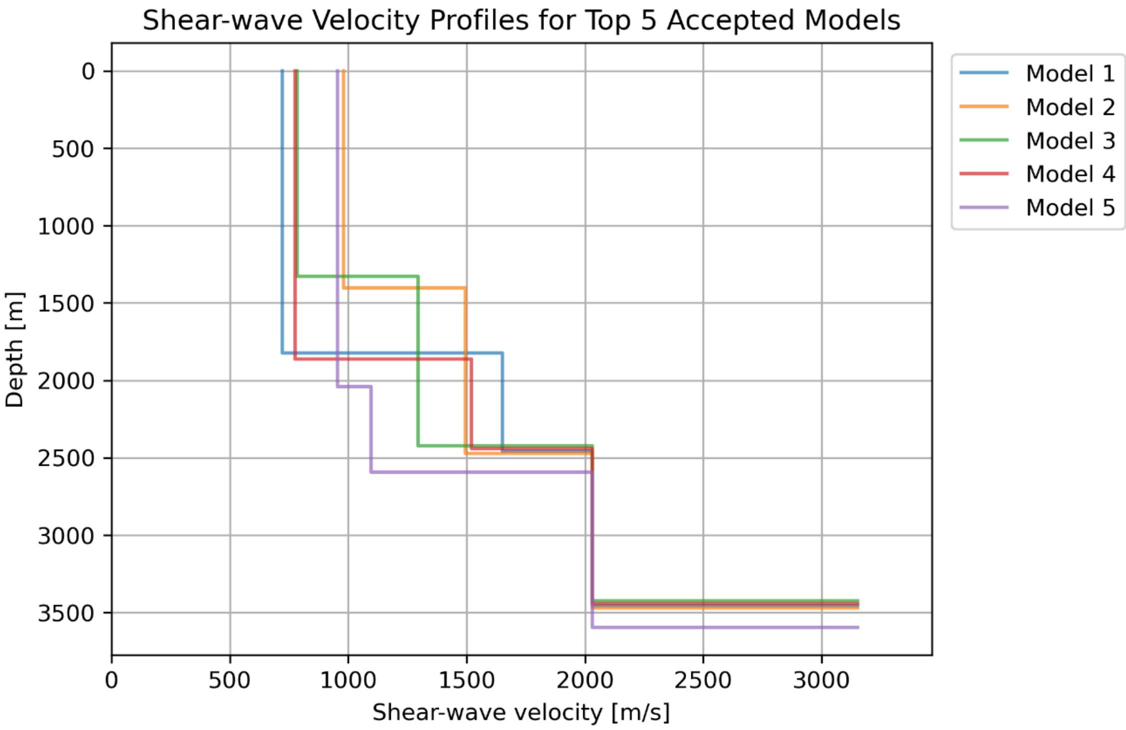

Figure 4.62. Top 5 Accepted Model for Station 3417 with Input from Synthetic Waveforms Generated at the Depth of 2 km

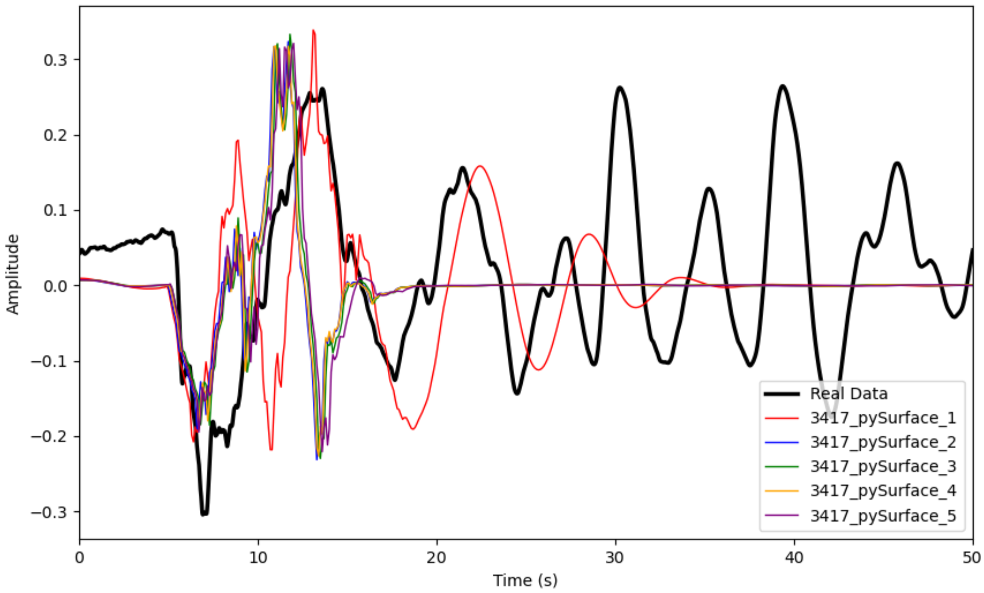

Figure 4.63. Top 5 Accepted Velocity Models Synthetic Waveforms Generated at the Surface vs Real Tangential Displacement Data for Station 3417

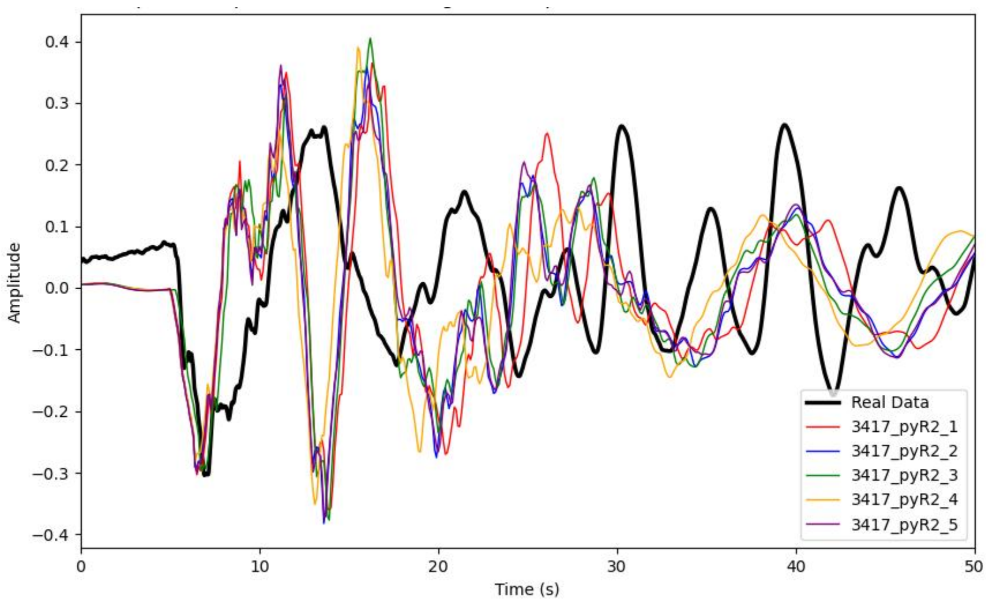

Figure 4.64. Top 5 Accepted Velocity Models Synthetic Waveforms Generated at the Depth of -2km vs Real Tangential Displacement Data for Station 3417

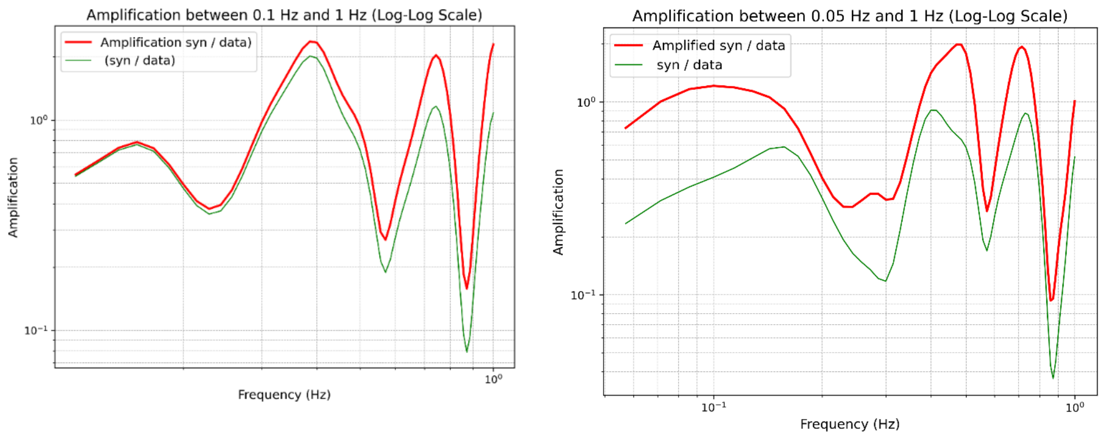

Figure 4.65. Amplification Range at the Frequency Domain for station 3417

4.4. Site Amplification Optimization and Site Specific Shallow Model Optimization for Station 3412

Station 3412 is particularly problematic to analyze because, for a wide range of velocity models tested, it is not possible to obtain an appropriate fit or amplification according to the expectations. This might depend on the site location or possible technical problems concerning the seismometer itself. Moreover, possible geological conditions of the site have to be taken into consideration in order to interpret the observed discrepancy. Since no specific range of velocity, thickness, and damping parameters yielded satisfactory results for station 3412, the parameter ranges were set to their maximum possible extent. Consequently, a total of 50,000 models were run to explore a broader solution space. Therefore, for station 3412, only the comparison between the synthetic waveforms generated from the top five models and the real data will be presented.

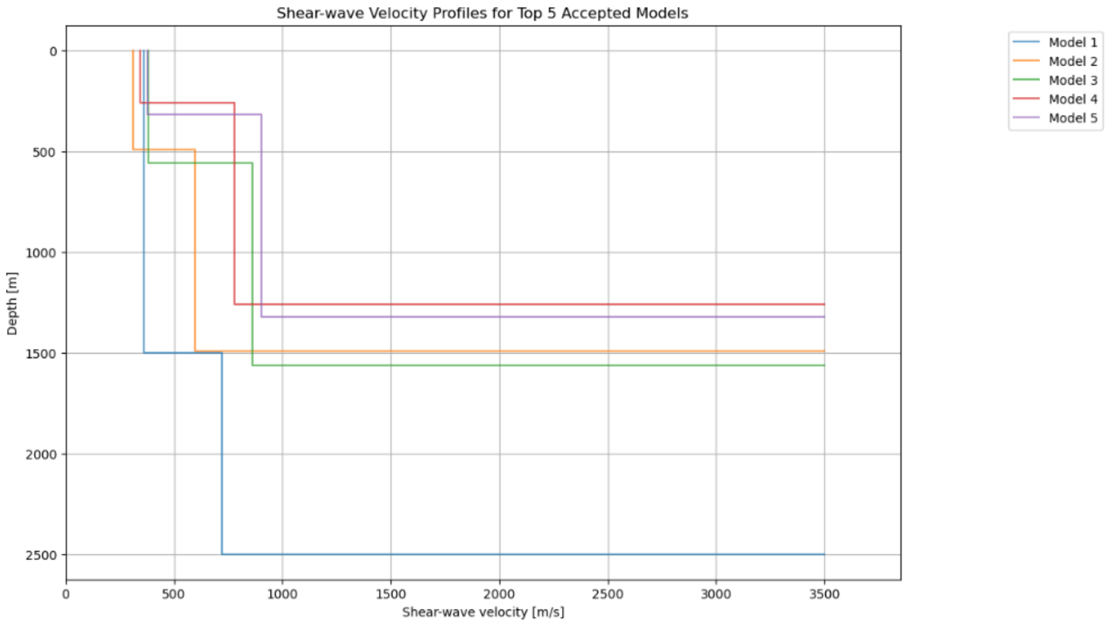

Figure 4.66. Top 5 Accepted Velocity Models with Input from Synthetic Waveforms Generated at the Surface for Station 3412

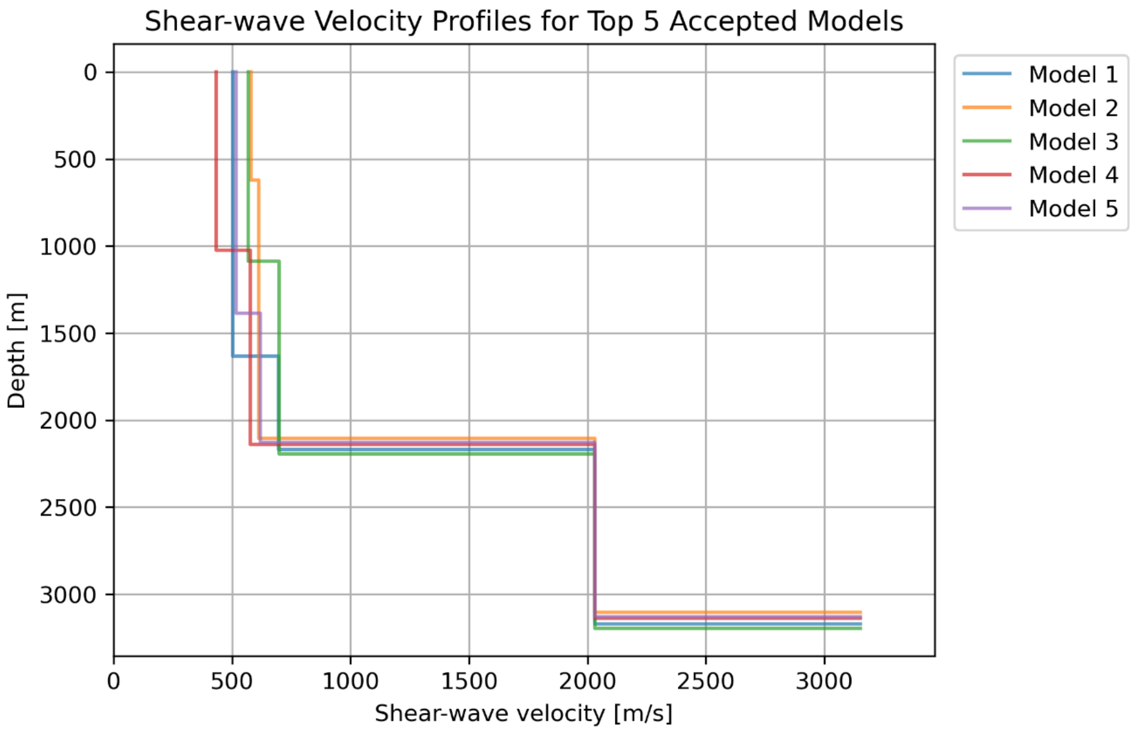

Figure 4.67. Top 5 Accepted Velocity Models with Input from Synthetic Waveforms Generated at the Depth of 2km for Station 3412

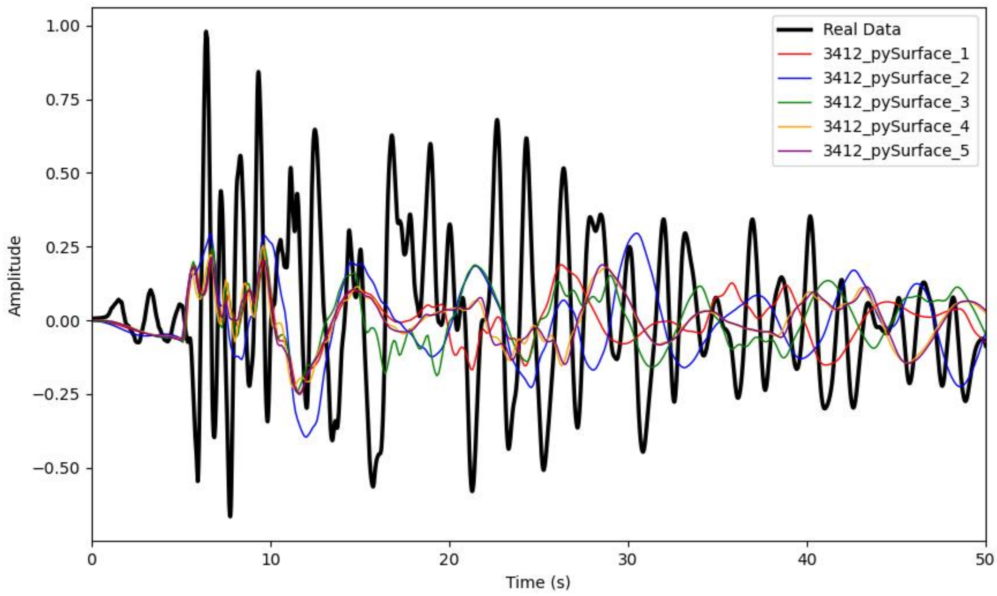

Figure 4.68. Top 5 Accepted Velocity Models Synthetic Waveforms Generated at the Surface vs Real Tangential Displacement Data for Station 3412

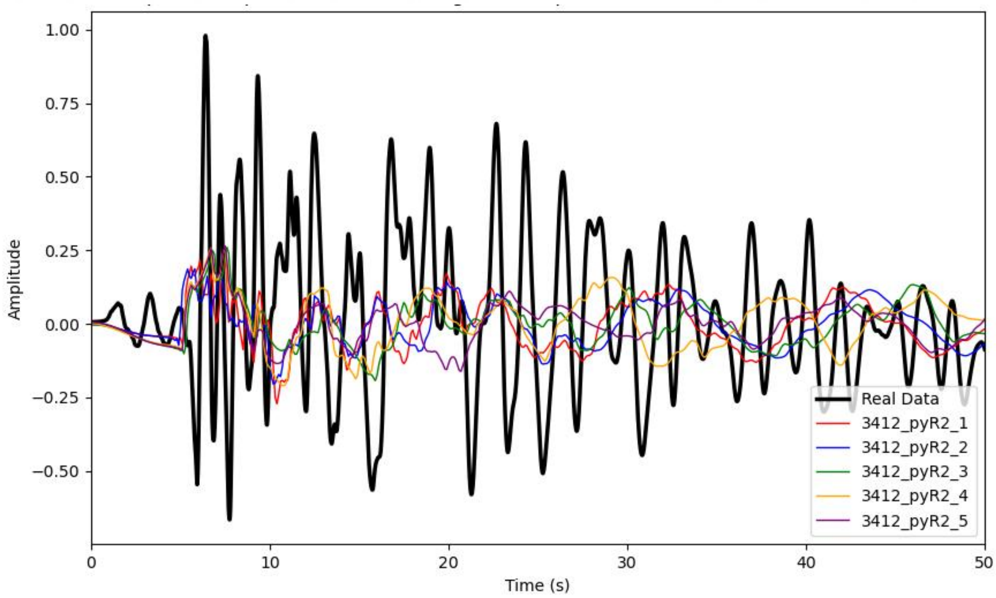

Figure 4.69. Top 5 Accepted Velocity Models Synthetic Waveforms Generated at the Depth of – 2km vs Real Tangential Displacement Data for Station 3412

Table 4.2 presents the comparison of the results of this study with the results of AFAD's station reports.

Table 4.1. Comparison of Study Result and AFAD Values

Station Code	Vs Values (m/s) from Study Results Layer 1	Vs Values (m/s) from Study Results Layer 2	Vs Values (m/s) AFAD Layer 1	Vs Values (m/s) AFAD Layer 2	Amplification Factor from Study Results	Amplification Factor from AFAD
3407	248	254	596	2000	10	No Info
3411	87	294	323	523	15	1.5
3413	420	789	452	772	9	1.61
3416	188	220	420	849	15	0.9

5. DISCUSSION

With over 17 million inhabitants, Istanbul is one of the most populous megacities in the world and lies very close to the North Anatolian Fault Zone-a highly active transform fault that has produced many large-magnitude earthquakes throughout history. Seismic hazard assessments indicate that there is a high probability of a significant earthquake affecting the region in the near future. Given the nature of Istanbul with highly dense urban settings, including critical infrastructure, high-rise buildings, and buildings of historical importance, understanding seismic wave propagation and site amplification effects is highly essential for earthquake resilience. Especially, long-period seismic waves dominate in the frequency range of 0.1-1.0 Hz, posing a serious threat to flexible structures such as large-span bridges and high-rise buildings, due to the resonance characteristic that could enhance seismic shaking. Therefore, proper modeling of site response and amplification through various geological conditions in the city is an important issue for seismic hazard mitigation.

During the 2019 Mw5.7 Silivri earthquakes, significant amplification and longer duration was observed in recorded waveforms on several AFAD strong-motion stations. This study presents a comparison of synthetic and recorded seismograms during the 2019 Mw5.7 Silivri earthquake generated using two different velocity models: a crustal model that was previously used for the 2019 Silivri sequence (Karabulut et al., 2020) and a second model where near-surface station specific layers were added to the crustal model based on

AFAD station reports to evaluate site amplification and subsurface velocity structures. The aim is to determine which of the two velocity models reproduces the seismic waveforms that were observed and also examines how different subsurface structures influence the propagation of long-period seismic waves. In order to achieve this, velocity models at the surface level and at a depth of -2 km depth were applied. It considers the contribution of deep velocity discontinuities to surface wave amplification and analyzes the influence on overall seismic response through a dual-layer approach.

Near-surface velocity values, provided by AFAD, were first added as supplementary layers into the crustal model in order to take care of the local geological variations.

The results show significant amplification for stations lying over soft sediments, especially stations 3412, 3411, 3407, 3413, and 3416. Amplification factors are remarkably higher within the frequency range from 0.1 to 0.5 Hz, which corresponds to the dominant frequencies of long-period seismic waves. This range is especially pertinent to seismic response for high-rise buildings and other flexible structures, as the long-period ground motions can resonate with the natural frequencies of such systems, thereby strongly amplifying shaking. Amplification at these stations indicates that buildings and infrastructure in these areas may be especially vulnerable to long-duration ground motion during large earthquakes.

We also conclude that for the stations where the ground motion is significantly amplified, the AFAD-based model is not capable of capturing the real characteristics of ground motion, which means the reported velocity values are not representative of site complexities.

On the other hand, the crustal model fits better with the observed data at hard rock stations but largely underestimates the amplification effects at soft sediment sites. Adding the station specific shallow layers from AFAD station reports does not yield any improvement. For the stations that are significantly amplified with respect to the estimates from the crustal model, in the frequency bands we are interested AFAD velocity models and amplification factor reports significantly underestimate the amplification observed in these station.

The large depth discrepancies in the amount of amplification indicates that local site conditions are likely to be the main source of the observed amplification. Therefore, we then proceed and optimize the shallow layers by adding site-specific two-layer models using vertical transfer functions to explain amplified and/or long duration data. As an input model we try a synthetic waveform at 2 km depth and also surface.

Stations on the soft sediments, such as 3411, 3416, and 3413, provided a best fit when input for site amplification is used as a synthetic waveforms generated at a depth of 2 km, and the rest is assumed to be 2 sedimentary layers complemented by the top layer of the crustal structure. These satisfactory fits in frequency domain also fits the amplification in the time domain. These results suggest that the amplification observed is due to site effects but is coming from the much deeper sedimentary layers which amplifies the waves at the longer period. We conclude that the stations that significantly amplify the ground motion can be modeled by site specific soft sediment models that are overlaying the crustal model at a depth. By contrast, station 3407 has a better fit when input for site amplification is used as a synthetic waveform generated at the surface indicating that the station is overlain by a shallower soft layer and the near-surface properties are dominant in the response at this station.

In hard rock stations, 3405, 3406, and 3408 have better fits when synthetic seismograms are calculated using the crustal velocity model on the surface, which was expected since the amplitude of the direct phase is well predicted by the initial crustal model. Nevertheless, station 3417 provided a better fit for the input synthetic model calculated at a depth of 2 km, proving that subsurface heterogeneities or deeper velocity structures have an influence on wave propagation at the site.

While the amplitudes on the hard rock sites are well predicted by the initial crustal model, the duration of these records is still quite long in comparison to the source duration (~4 seconds) and reverberations continues much longer than the predicted (e.g. Figure 4.63, 4.64). The problem with adding soft layers to these hard rock stations is that while adding soft layers yield spectral fits, the amplitude of the initial SH pulse is significantly overestimated when soft layers are added. This implies that some of the reverberations are not generated below the site but rather are path effects. One possibility is that since the earthquake occurs in the central basin where the sediment depth is about 6 km, the phases generated at the source region also contribute to the long period reverberations. In addition, when the waves generated hit the shelf of the Marmara coast, that could also affect the observed waveforms. It should also be noted that more than one earthquake and also earthquakes coming from different azimuths should be studies to improve the estimated velocity models.

This study assumes that the main effects come from local site conditions; path effects-such as the wave propagation through different crustal structures-may vary. The variations observed here between synthetic and empirical estimates could arise due to source variability or in path effects since those were not considered here. Such models have further refinements involving the analysis of earthquakes coming from other azimuths to fix these anomalies if they persist at more source locations and azimuths. A full 3D model and a 3D eave propagation model is necessary to calculate the details.

Especially, the strong reverberation effects present at station 3412, which shows long oscillations even in acceleration data, and such an anomaly could be related to very thick unconsolidated sediments or to some technical problems at the station. Contrary to other available stations, the waveform characteristics of 3412 seem quite different from those expected because of a high resonant condition of the site or due to some inconsistencies of the adopted velocity model.

Further comparison between the AFAD-based and crustal models reveals large discrepancies in near-surface velocity values. The optimized velocity models, derived from the best-fitting synthetic seismograms, are considerably different from the velocity structures reported by AFAD. This suggests that the currently available velocity models of AFAD need further refinement, particularly for soft sedimentary sites where local geological heterogeneities strongly affect ground motion. Thus, a detailed velocity model would highly be derived, considering that the seismic hazard studies are in need of a realistic model of the velocity distribution. High-resolution geotechnical and geophysical data should be considered in the derivation.

Insufficient capability of crustal model to provide site amplification effects at soft sediment sites calls for refined local velocity models. Although the crustal model represents a reasonable approximation for hard rock stations, it systematically underestimates the level of amplification of sites overlying unconsolidated sediments. This reality underlines the importance of the local velocity model that would take into account the detailed subsurface geophysical properties. Finally, some discrepancies between observed and synthetic waveforms are possibly due to the adopted damping factors that ranged between 0.1 and 0.5 in this study. Another decisive factor in amplification is the thickness of the surface layer, which further complicates the modeling of site response in Istanbul.

The location at a depth of -2 km was important to understand how deep velocity discontinuities may affect seismic wave amplification. These results imply important roles of deep-seated velocity contrasts in resonance effects at soft sediment sites, necessitating depth-dependent velocity models in site response studies. Findings are in good agreement with previously reported enhancement of long-period seismic waves resulting from deep basin resonance, thereby further justifying the inclusion of deep geological structure in seismic hazard assessment.

In general, this study underlines the critical role that site effects play in the propagation of seismic waves in Istanbul. The findings confirm that long-period seismic waves are a major factor in seismic hazard assessments for the region, particularly in areas underlain by soft sediments where amplification is most pronounced in the 0.1–0.5 Hz range. These effects, therefore, cannot be captured by a standard velocity model, and call for the need to develop superior site-specific velocity models incorporating high-resolution subsurface data. Due to the high susceptibility of Istanbul to large-magnitude earthquakes, as well as widespread soft sedimentary basins, further studies regarding long-period wave effects and local site conditions become necessary. Continued research into site response characteristics, as well as further developments in velocity modeling techniques, will be integral to earthquake resilience and seismic hazard mitigation.

6. CONCLUSION

In this study we explored the ground motions generated at the AFAD strong-motion sites in Istanbul. We show that while direct SH wave displacements can be well estimated by a crustal model significant amplification and longer durations in soft-rock sites cannot be explained by neither the crustal model, nor by adding shallow layers from AFAD station reports. We therefore attempt to obtain the shallow velocity structure beneath these stations by calculating the synthetic waveforms at depth and then convolving with the transfer function of the shallow layers. We successfully obtained the shallow layer on sites that are significantly amplified on the European side of the city. The estimated thickness in these sites varies between several hundred meters to almost a km. While the amplification in most sites can be explained, it is more challenging to model the stations where there is not significant amplification but still the reverberations continue for significantly longer. We infer that more complex 3D models are necessary to explain this behavior. Furthermore earthquakes from different azimuths are necessary to further improve the reliability of the obtained velocity models.

APPENDIX A: DISTRUBUTION ERRORS FOR STATION 3411 WITH INPUT FROM SYNTHETIC WAVEFORMS GENERATED AT THE SURFACE

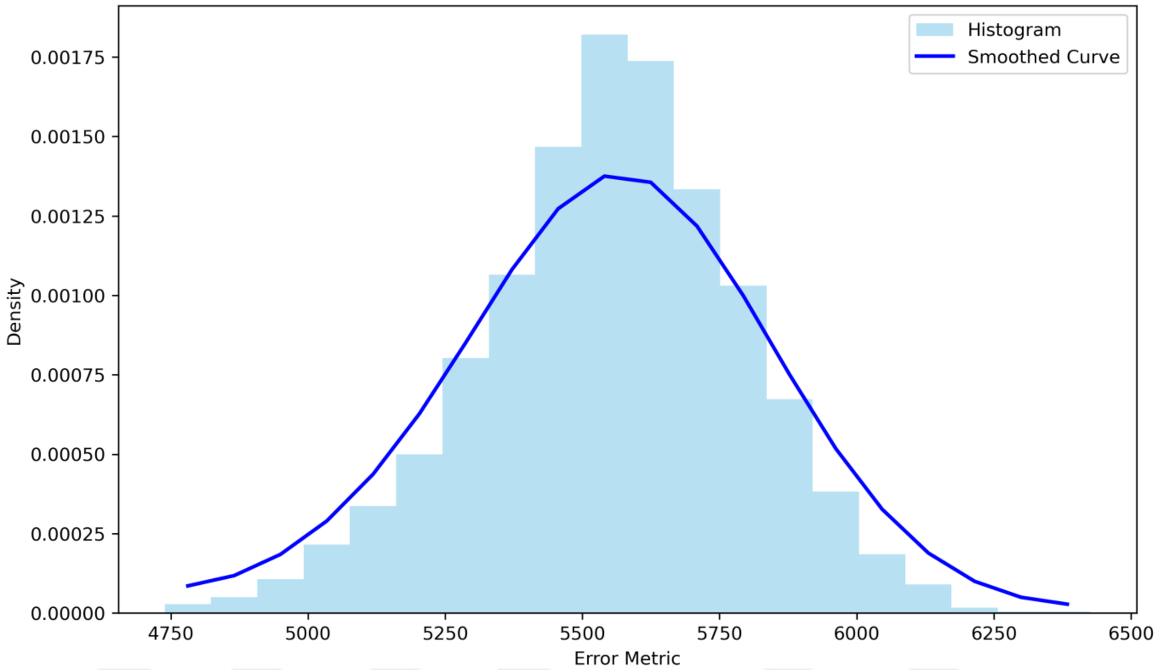

Figure A1. Distribution of Error Metrics for 5000 Two-Layer Models at Station 3411 Using Input from Synthetic Waveforms Generated at the Surface.

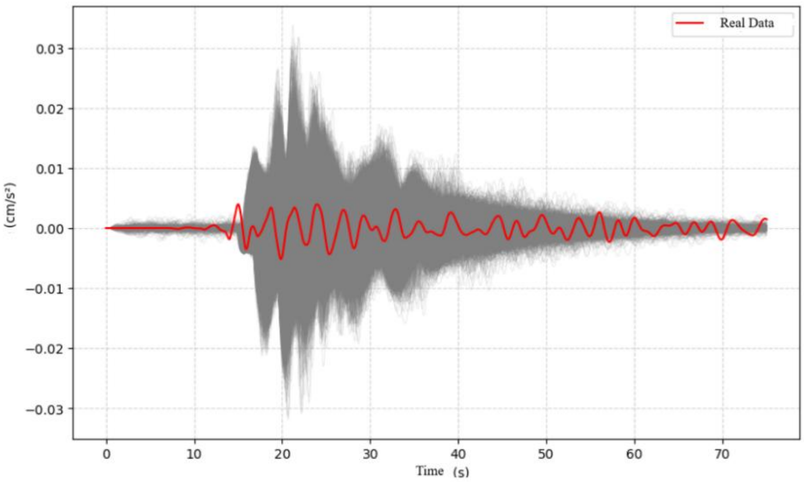

Figure A2. 5000 Synthetic vs Real Data Comparison for Station 3411

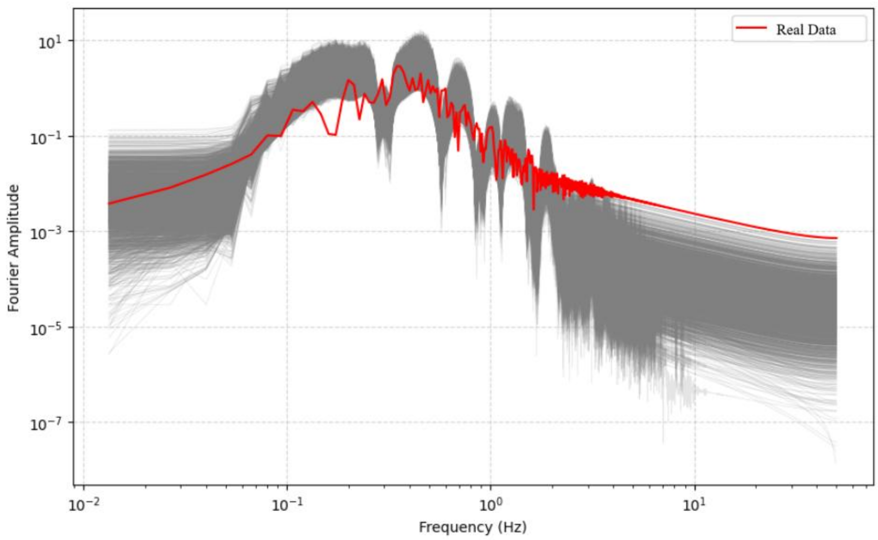

Figure A3. 5000 Model vs Real Data Comparison Spectral Domain for Station 3411

REFERENCES

Atakan, K., Ojeda, A., Meghraoui, M., Barka, A. A., Erdik, M., & Bodare, A. (2002). Seismic hazard in Istanbul following the 17 August 1999 Izmit and 12 November 1999 Duzce earthquakes. Bulletin of the Seismological Society of America, 92(1), 466-482.

Bard, P. Y. (1999). Microtremor measurements: a tool for site effect estimation. The effects of surface geology on seismic motion, 3, 1251-1279.

Bard, P.Y., Duval, A.M., Lebrun, B., Lachet, C., Riepl, J. and Hatzfeld, D., 1997, Reliability of the H/V technique for site effects measurements: An experimental assessment, Proc. of 8th Int. Conf. Soil Dyn. Earth. Eng., Istanbul, Turkey.

Bielak, J., Graves, R. W., Olsen, K. B., Taborda, R., Ramírez-Guzmán, L., Day, S. M., ... & Juve, G. (2010). The ShakeOut earthquake scenario: Verification of three simulation sets. Geophysical Journal International, 180(1), 375-404.

Birgören, G., Sekiguchi, H., & Irikura, K. (2004). Rupture model of the 1999 Düzce, Turkey, earthquake deduced from high and low frequency strong motion data. Geophysical Research Letters, 31(5).

Boore, D. M. (2003). Simulation of ground motion using the stochastic method. Pure and applied geophysics, 160, 635-676.

Boore, D. M. (2004). Estimating Vs (30) (or NEHRP site classes) from shallow velocity models (depths< 30 m). Bulletin of the seismological society of America, 94(2), 591-597.

Borcherdt, R. D. (1970). Effects of local geology on ground motion near San Francisco Bay. Bulletin of the Seismological Society of America, 60(1), 29-61.

Bouchon, M. (1982). The complete synthesis of seismic crustal phases at regional distances. Journal of Geophysical Research: Solid Earth, 87(B3), 1735-1741.

Day, S. M., Graves, R., Bielak, J., Dreger, D., Larsen, S., Olsen, K. B., ... & Ramirez-Guzman, L. (2008). Model for basin effects on long-period response spectra in southern California. Earthquake Spectra, 24(1), 257-277.

Erdik, M., Fahjan, Y., Ozel, O., Alcik, H., Mert, A., & Gul, M. (2003). Istanbul earthquake rapid response and the early warning system. Bulletin of earthquake engineering, 1, 157-163.

Erdik, M., Demircioglu, M., Sesetyan, K., Durukal, E., & Siyahi, B. (2004). Earthquake hazard in Marmara region, Turkey. Soil Dynamics and Earthquake Engineering, 24(8), 605-631.

Ergin, M., Özalaybey, S., Aktar, M., & Yalcin, M. N. (2004). Site amplification at Avcılar, Istanbul. Tectonophysics, 391(1-4), 335-346.

Graves, R. W., Aagaard, B. T., & Hudnut, K. W. (2011). The ShakeOut earthquake source and ground motion simulations. Earthquake Spectra, 27(2), 273-291.

Hoşgören, M. Y., 1995, İzmit Körfezi Havzasının Jeomorfolojisi, (ed. E. Meriç, İzmit Körfezi Kuvaterner İstifi içinde) pp.343-348, Kocaeli.

İstanbul Kent Jeolojisi Raporu, 2011, İstanbul Büyükşehir Belediyesi Deprem ve Zemin İnceleme Şube Müdürlüğü

Irikura, K. (1986, December). Prediction of strong acceleration motion using empirical Green's function. In Proc. 7th Japan Earthq. Eng. Symp (Vol. 151, pp. 151-156).

Joyner, W. B., & Chen, A. T. (1975). Calculation of nonlinear ground response in earthquakes. Bulletin of the Seismological Society of America, 65(5), 1315-1336.

Joyner, W. B., & Boore, D. M. (1981). Peak horizontal acceleration and velocity from strong-motion records including records from the 1979 Imperial Valley, California, earthquake. Bulletin of the seismological Society of America, 71(6), 2011-2038.

Kanamori, H. (1994). Mechanics of earthquakes. Annual Review Of Earth And Planetary Sciences, Volume 22, pp. 207-237., 22, 207-237.

Karabulut, H., Güvercin, S. E., Eskiköy, F., Konca, A. Ö., & Ergintav, S. (2021). The moderate size 2019 September M w 5.8 Silivri earthquake unveils the complexity of the Main Marmara Fault shear zone. Geophysical Journal International, 224(1), 377-388.

Ketin, İ., 1973, Umumi Jeoloji (General Geology), Published by İTÜ, 4th Ed.

Kitsunezaki C, Goto N, Kobayashi Y, Ikawa T, Horike M, Saito T, Kurota T, Yamane K, Okozumi K (1990) Estimation of P- and S-wave velocities in deep soil deposits for evaluating ground vibrations in earthquake. J JSNDS 9: 1–17

Komatitsch, D., & Tromp, J. (1999). Introduction to the spectral element method for three-dimensional seismic wave propagation. Geophysical journal international, 139(3), 806-822.

Okay, A. I. (1986). High-pressure/low-temperature metamorphic rocks of Turkey. Geological Society of America Memoirs, 164, 333-347.

Özel, N. M., Sasatani, T., & Özel, O. (2004). Strong ground motion during the largest aftershock (Mw= 5.8) of the 1999 Izmit earthquake, Turkey. Tectonophysics, 391(1-4), 347-355.

Özgül, N., 2012, "Stratigraphy and some structural features of the İstanbul Palaeozoic", Turkish J. Earth Sciences, vol. 21, pp. 817-866.

Parolai, S., Bormann, P., & Milkereit, C. (2002). New relationships between Vs, thickness of sediments, and resonance frequency Generated by the H/V ratio of seismic noise for the Cologne area (Germany). Bulletin of the seismological society of America, 92(6), 2521-2527.

Picozzi, M., Strollo, A., Parolai, S., Durukal, E., Özel, O., Karabulut, S., ..& Erdik, M. (2009). Site characterization by seismic noise in Istanbul, Turkey. Soil Dynamics and Earthquake Engineering, 29(3), 469-482.

Picozzi, M., Parolai, S., Bindi, D., & Strollo, A. (2009). Characterization of shallow geology by high-frequency seismic noise tomography. Geophysical Journal International, 176(1), 164-174.

Pulido, N., Ojeda, A., Atakan, K., & Kubo, T. (2004). Strong ground motion estimation in the Sea of Marmara region (Turkey) based on a scenario earthquake. Tectonophysics, 391(1-4), 357-374.

Satoh, T., Kawase, H., & Matsushima, S. I. (2001). Estimation of S-wave velocity structures in and around the Sendai basin, Japan, using array records of microtremors. Bulletin of the seismological society of America, 91(2), 206-218.

Semblat, J. F., Kham, M., Parara, E., Bard, P. Y., Pitilakis, K., Makra, K., & Raptakis, D. (2005). Seismic wave amplification: Basin geometry vs soil layering. Soil dynamics and earthquake engineering, 25(7-10), 529-538.

Singh, S. K., Mena, E., & Castro, R. (1988). Some aspects of source characteristics of the 19 September 1985 Michoacan earthquake and ground motion amplification in and near Mexico City from strong motion data. Bulletin of the Seismological society of America, 78(2), 451-477.

Sørensen, M. B., Oprsal, I., Bonnefoy-Claudet, S., Atakan, K., Mai, P. M., Pulido, N., & Yalciner, C. (2006). Local site effects in Ataköy, Istanbul, Turkey, due to a future large earthquake in the Marmara Sea. Geophysical Journal International, 167(3), 1413-1424.

Soysal H., S. Sipahioglu, D. Kolcak and Y. Altinok, 1981, Turkiye ve Cevresinin Tarihsel deprem Katalogu, TUBITAK, Proje no. TBAG 341, Istanbul, pp. 86.

Şengör, A.M.C. and Y. Yılmaz, 1981, "Tethyan evolution of Turkey: a plate tectonic approach", Tectonophysics, Vol. 75, pp. 181-241.

Tan, O., Karagöz, Ö., Ergintav, S., & Duran, K. (2023). The neglected Istanbul earthquakes in the North Anatolian Shear Zone: tectonic implications and broad-band ground motion simulations for a future moderate event. Geophysical Journal International, 233(1), 700-723.

Zhu, C., Pilz, M., & Cotton, F. (2020). Evaluation of a novel application of earthquake HVSR in site-specific amplification estimation. Soil Dynamics and Earthquake Engineering, 139, 106301.

Zhu, L., & Rivera, L. A. (2002). A note on the dynamic and static displacements from a point source in multilayered media. Geophysical Journal International, 148(3), 619-627.